INVESTIGATION ON THE LIQUEFACTION POTENTIAL OF SAND-GRANULATED RUBBER MIXTURE THAT USED AROUND THE BURIED PIPES: NUMERICAL MODELING AND DEVELOPING

A Thesis Submitted to
the Graduate School of
İzmir Institute of Technology
In Partial Fulfillment of the Requirements for the Degree of

MASTER OF SCIENCE

in Civil Engineering

by
Hadi VALIZADEH

November 2021
İZMİR

ACKNOWLEDGEMENTS

I offer my gratitude to the closest people to me for their help and support; I would not have reached this level of knowledge without their support.

First of all, I would like to express my gratitude to Prof. Dr. Nurhan ECEMIŞ, my Supportive supervisor, for her patience, constant guidance, and encouragement during the progress of this research.

I would like to thank all my family, especially my dear wife TORKAN, for her endless patience and encouragement in all stages of our life together.

Finally, I would express my respect to my friends who helped me during the completion of this study. Thank you all.

ABSTRACT

INVESTIGATION ON THE LIQUEFACTION POTENTIAL OF SAND-GRANULATED RUBBER MIXTURE THAT USED AROUND THE BURIED PIPES: NUMERICAL MODELING AND DEVELOPING

Recently, the sand-granulated rubber mixture has been reported as a new soil improvement method that can be applied as a liquefaction mitigation filling material around the buried pipes. This study performed numerical modeling of liquefaction potential of tire-derived granulated rubber–sand mixture used around the buried pipes by the FLAC 2D software. The effects of pipe size, burial depth, and shaking intensity on the pipe uplift and the liquefaction potential of the sand-tire derived granulated rubber mixture placed around the buried pipes were investigated using the finite difference method. Furthermore, UBCSAND advanced soil constitutive model was used for liquefaction analysis.

First, the result of 1-g shaking table tests was utilized for the verification of the numerical analysis. Comparing the numerical results and the experimental measurements showed that the numerical simulation using the UBCSAND constitutive model could accurately estimate the liquefaction-induced uplift of the buried pipes as well as the related failure. Then, a parametric study was conducted to investigate the effects of the pipe diameter, pipe depth, and the maximum acceleration on pipe uplift and liquefaction potential when the sand-granulated rubber mixture was placed as the filling material. Eventually, an analytical formula was proposed to estimate the liquefaction-induced uplift of buried pipes, and the soil failure mode was categorized according to the pipe's burial depth.

Keywords: Dynamic numerical modeling, Buried pipes, Granulated rubber, Liquefaction potential, Finite Difference Method (FDM), UBCSAND constitutive model, Liquefaction induced uplift.

ÖZET

GÖMÜLÜ BORULAR ETRAFINA YERLEŞTİRİLEN KUM-LASTİK KIRPINTI KARIŞIMLARINDA BORU HAREKETİNİN İNCELENMESİ: NÜMERİK MODELLEME VE GELİŞTİRME

Son zamanlarda, gömülü boruların çevresinde sıvılaşmayı azaltan dolgu malzemesi olarak uygulanabilen yeni bir zemin iyileştirme yöntemi olarak kum-granüle kauçuk karışımı rapor edilmiştir. Bu çalışma, gömülü boruların çevresinde kullanılan lastikten türetilen granüle kauçuk-kum karışımının sıvılaşma potansiyelinin FLAC 2D yazılımı ile sayısal modellemesini gerçekleştirdi.

Boru ebadı, gömme derinliği ve sarsıntı yoğunluğunun borunun yükselmesi üzerindeki etkileri ve gömülü boruların etrafına yerleştirilen kum-lastik türevi granüle kauçuk karışımının sıvılaşma potansiyeli sonlu farklar yöntemi kullanılarak araştırıldı. Ayrıca, sıvılaşma analizi için UBCSAND gelişmiş zemin kurucu modeli kullanılmıştır.

İlk olarak, sayısal analizin doğrulanması için 1-g sarsma tablası testlerinin sonucu kullanılmıştır. Sayısal sonuçların ve deneysel ölçümlerin karşılaştırılması, UBCSAND kurucu modelini kullanan sayısal simülasyonun, gömülü boruların sıvılaşma kaynaklı yükselmeyi ve ilgili arızayı doğru bir şekilde tahmin edebileceğini gösterdi. Daha sonra, dolgu malzemesi olarak kum-granüle kauçuk karışımı yerleştirildiğinde boru çapı, boru derinliği ve maksimum ivmenin boru kaldırma ve sıvılaşma potansiyeli üzerindeki etkilerini araştırmak için parametrik bir çalışma yapılmıştır. Sonunda, gömülü boruların sıvılaşma kaynaklı yükselmeyi tahmin etmek için analitik bir formül önerildi ve zemin kırılma modu, borunun gömme derinliğine göre kategorize edildi.

Anahtar Kelimeler: Dinamik sayısal modelleme, Gömülü borular, Granül kauçuk, Sıvılaşma potansiyeli, Sonlu Farklar Yöntemi (FDM), UBCSAND kurucu modeli, Sıvılaşma kaynaklı yükselme.

TABLE OF CONTENTS

LIST OF FIGURES

Figure **Page**

Figure **Page**

Figure **Page**

Figure **Page**

LIST OF TABLES

Table **Page**

LIST OF ABBREVIATIONS

ASTM	American Society for Testing and Materials
Dr	Relative Density
EPWP	Excess Pore Water Pressure
FDA	Finite Difference Analysis
FLS	Flow Liquefaction Surface
GR	Granulated Rubber
SGR	Sand-Granulated Rubber
STCh	Sand-Tire Chips
TDA	Tire-Derived Aggregate
PSR	Principal Stress Rotation
USCS	Unified Soil Classification System
DST	Direct Sheat

در این خاک، در این خاک، در این مزرعه پاک

بجز عشق، بجر مهر، دگر تخم نکاریم

" رومی "

In this earth, In this earth, In this pure farm

We do not plant any seeds except love and kindness

“Rumi”

CHAPTER 1

INTRODUCTION

1.1. Foreword

There are various lifelines in urban and non-urban areas severely affected by fearsome earthquakes. Gas and oil transmission lines, water distributions and sewage networks, transportation tunnels, and railroads are examples of the lifelines; their failure can aggravate the earthquake damages. For instance, along with the economic loss and environmental pollution, the damage in the oil transmission pipelines can cause a horrible fire. The historical study of damages caused by destructive earthquakes worldwide revealed that the lifelines failure contribution was very significant. For example, in 1989 Loma Prieta earthquake in America over 90 percent, in 1994 Northridge earthquake over 80 percent, in 1995 Cube earthquake in Japan over 75 percent, and in 1999 Izmit earthquake over 85 percent of failures were direct and indirect related to lifelines failures (Rubeiz, 2009). Sand liquefaction is the most critical event which damages the lifelines.

Granular soils, like saturated sands, are highly susceptible to liquefaction. During intense loading, these kinds of soils may liquefy in undrained conditions due to Excess Pore Water Pressure (EPWP) generation. Liquefaction of sands and silty sands generates forces that affect the buried structures as pipes. Surveying on the most past earthquakes shows that buried pipes failure in liquefiable sand is highly intense.

1.2. History of Pipeline Vulnerabilities in Past Earthquakes

This section summarized some important earthquakes that have damaged the pipelines and caused economic and social losses.

1.2.1. 1906 San Francisco Earthquake

On April 18, 1906, the San Francisco earthquake with an 8.3 M_w happened. In this earthquake, about 300 main water sources and 23000 water supply sub-sources were destroyed. Due to the lack of the proper water supply system, the fire continued for three days, and over 80 percent of damages were because of fire, whereas only 20 percent of failures were caused by seismic loading (Rubeiz, 2009).

1.2.2. 1989 Loma Prieta Earthquake

On October 17, 1989, at 5.04 o'clock P.M., a 6.9 M_w earthquake happened in San Francisco and surrounding areas. The epicenter was reported at 37.04 degrees north latitude and 121.88 degrees west longitude near the summit of Loma Prieta in the Santa Cruise mountains. In this earthquake, the main harm happened in the liquefiable area like the San Francisco seaport. Old low-pressure steel pipes of the gas distribution system were severely damaged. In San Francisco, Oakland, Berkley, and Santa Cruise, near 600 water pipe failures happened (O'Rourke, 1996).

1.2.3. 1993 Kushiro-Oki Earthquake

On January 15, 1999, an earthquake with 7.8 M_w occurred at Kushiro-Oki city in the north of Japan. This earthquake caused significant damages to sewage networks, gas transportation lines, roads, and ports. So many old sewage pipes in and out of the city were out of service. In the city, 7744 m and out of the city 10838 m of pipes were severely damaged. Based on the geological reports, most of the damages occurred in the liquefiable soil areas. The three types of failures as bending failure, failure in connections, and uplift, were observed in buried pipelines. Also, 20 manholes were raised from the ground with a maximum amount of 1.3 m (Yasuda et al. 1994; Yasuda and Kiku, 2006) (Figure 1.1).

Figure 1.1. Uplift of manhole after the 1993 Kushiro-oki earthquake in Kushiro Town (Source: Yasuda and Kiku, 2006)

1.2.4. 1994 Northridge Earthquake

This 6.7 M_w earthquake on January 17, 1994, happened. In addition to severe damages to lifelines, the earthquake also caused severe damages to residential and commercial buildings. The earthquake damages are estimated at around $20 billion. The earthquake damaged the Northridge water pipeline to California and caused 1500 water transmission lines failure in San Francisco. It also caused 1700 water leaks in pipelines and 1400 fractures in the San Francisco valley gas, water, and fuel pipelines. Many failures occurred in specific areas with high liquefaction potential. Outside these areas, the fracture distribution pattern showed the vulnerability of old pipes made by brittle materials due to the ground deformation. On Balboa Boulevard, a 22-inch pipe was broken due to the tension and pressure forces. In some water and gas pipes, fracture at the connections was observed. In this earthquake, the gas pipes were damaged, including 35 failures in old pipelines, 123 steel pipelines, and 117 other pipes. The 394 leakage cases were also observed after the earthquake due to erosion (Rubeiz, 2009).

1.2.5. 2004 Niigata-ken Chuetsu Earthquake

On October 23, 2004, a 6.6 M_w earthquake happened at Niigata-ken, killing 48 and injuring 4160 people. In this earthquake, major damages were caused to the sewage networks. Furthermore, more than 1450 undergrounds structures, sewage facilities, including manholes, were destroyed. The manhole's uplift from the street and city passages was measured up to 1.5 m. In addition to sewage system failure, this phenomenon led to urban traffic blockage, which prevented emergency vehicles movement and increased human losses (Tobita et al., 2009).

Figure 1.2. Uplifted manhole after the 2004 Niigata-ken Chuetsu, Japan, Earthquake (Source: Tobita et al., 2009)

1.2.6. 2011 Tohoku-Japan Earthquake

This earthquake happened on March 11, 2011, in Japan. In Urayasu city, many underground structures were damaged because of their floatation due to the liquefaction phenomenon. Most of the manholes uplifted near 0.6 m, which fractured the transportation as well as water and sewage network (Chian and Tokimatsu, 2012).

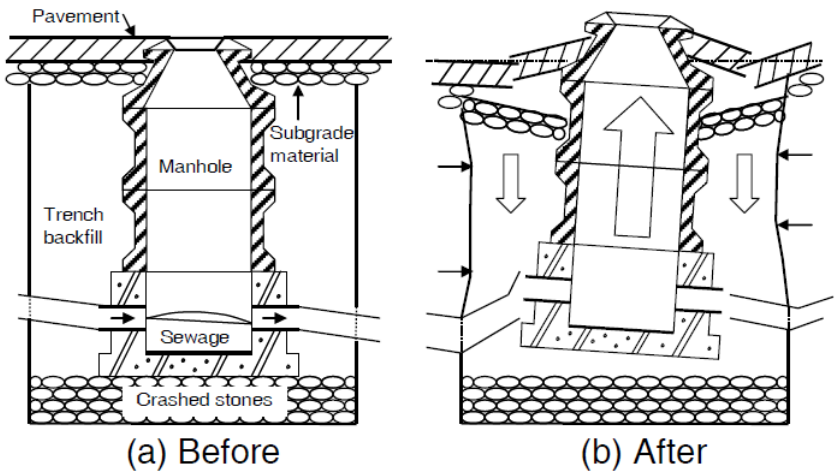

Figure 1.3. Schematic illustration of the damage pattern of a manhole; (a) before and (b) after an earthquake (Source: Tobita et al., 2009)

Figure 1.4 Right: Uplift of a manhole at Shiraishi, Left: Uplift of a manhole at Iwakiri (Source: Yamaguchi et al., 2012)

The mentioned items were clear examples of pipeline fractures in the recent earthquake, which many researchers aimed to identify the pipes failure cases. It should be noted that underground tunnels operated similarly to large diameter pipes and were not safe from such damage.

1.3. The Phenomenon of Liquefaction

During the last six decades after the 1964 Niigata and Alaska earthquakes, many investigations have been done on the liquefaction event and its related damages. This

section has a basic concepts review related to liquefaction to find every aspect of this phenomenon.

The study of the liquefaction phenomenon dated back to 1920 but is still one of the selected discussion topics in geotechnical engineering. Castro and Paulo, 1977, mentioned that Hazen, in 1920, was the first one who used the liquefy word for the Calaveras dam failure (Bhattacharya et al., 2003). Ishihara, named this event to Terzaghi and Peck in 1948 (Ishihara, 1993). Also, Kramer introduced Mogami and Kubo as the liquefaction inventor in his seismic geotechnical book (Kramer, 1996). Das, 1983, mentioned Casagrande as the first one who studied the liquefaction in sands in 1936.

1.3.1. Liquefaction Mechanism

When the loose granular soil is saturated, the EPWP increases due to the loading in undrained conditions. As a result, the effective stresses are reduced, based on the effective stress relation:

$$\sigma' = \sigma - u \tag{1.1}$$

In which σ', σ and u are effective stress, total stress, and the Pore Water Pressure (PWP), respectively. If u equals to σ, therefore $\sigma' = 0$. In this case, sand regarding Mohr-Coulomb fracture in 1-2 relation has no shear strength and acts like a thick fluid.

$$\tau = \sigma \tan \varphi + c \tag{1.2}$$

Where c is cohesion, τ is shear strength, φ is internal friction angle, and σ is vertical stress.

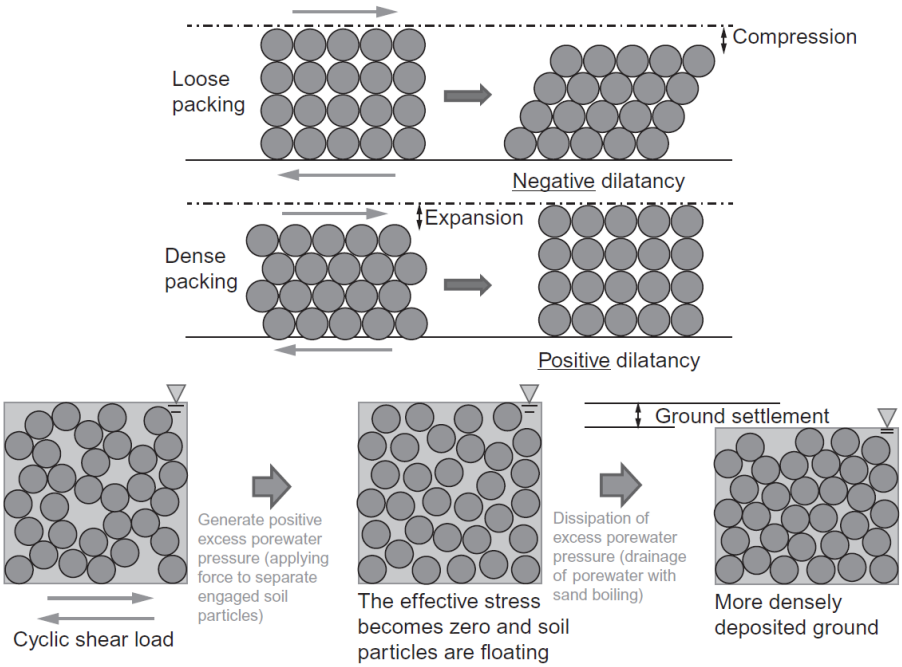

Figure 1.5. Mechanism of liquefaction

(Source: Butterworth-Heinemann, 2018)

In sandy soils, particles are stable till the earthquake effective forces change the soil particles' stresses. This case in Fig.1-5a is schematically simulated with circular spheres. When the soil deforms due to shear stresses caused by earthquake vibrations, the connectivity between particles disappears, as shown in Fig 1-5b. As a result, the forces which transformed to EPWP by particles connectivity causes soil liquefaction. In this case, the particles connectivity are disappeared, and the shear strength of the soil gets near to zero, and soil behaves similar to a fluid whose specific gravity is equal to saturated soil. After liquefaction, the soil particles connectivity is reestablished with the water outflows as shown in Fig.1-5c, the shear strength reaches the soil mass. The volume reduction in the soil is equal to PWP that comes out of the soil. This behavior in real soil consisting of various particles is very complicated (Butterworth-Heinemann, 2018).

1.3.2. Phenomena Related to Liquefaction

The liquefaction phenomenon can be divided into two main parts: Flow liquefaction and Cyclic mobility; both are very important and should be studied in the

liquefaction damages. Flow liquefaction is less common than cyclic mobility, but the Flow damages are severe. In return, Cyclic liquefaction happens in massive areas of soil, and its destructive effects can be classified from low to severe damage (Kramer, 1996).

1.3.2.1. Flow Liquefaction

Flow liquefaction has essential effects among all the liquefaction phenomenon. Flow liquefaction occurs when the shear stress required for the static balance of soil mass is larger than the residual shear stress of liquefied soil. In Flow liquefaction, large deformations occur in the soil due to the static shear stresses, and dynamic stress only creates internal instability. The sudden expansion and large distance that liquefied materials often move characterize flow failures (Kramer, 1996). Figure 1.6 shows the susceptible zone to flow liquefaction. The occurrence of flow liquefaction will occur if the initial condition falls within the shaded zone and an undrained disturbance change the effective stress path to the Flow Liquefaction Surface (FLS). (Kramer, 1996).

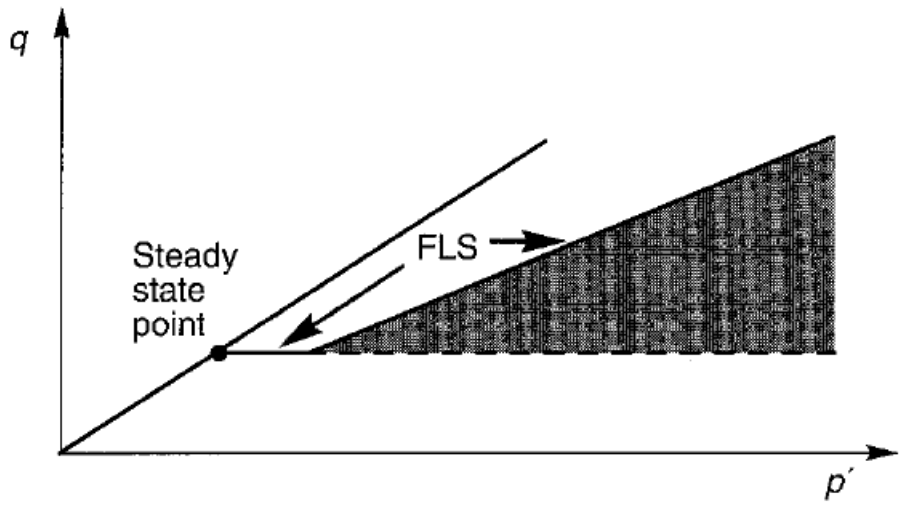

Figure 1.6. Flow liquefaction susceptible zone

(Source: Kramer, 1996)

1.3.2.2. Cyclic Mobility

Cyclic mobility is another phenomenon that can cause massive and unexpected deformations during an earthquake. Cyclic mobility happens when the static shear stress is less than the shear stress of liquefied soil. Deformations caused by cyclic mobility failure during an earthquake are increasingly widespread. Unlike Flow liquefaction, the deformations created by Cyclic mobility are due to both cyclic and static stresses. These deformations which are known as lateral spreading, could happen on a slope or even on flat ground near the water, which is the specific mode of Cyclic mobility called level ground liquefaction. Since there are no static horizontal shear stresses that cause lateral deformations, Cyclic liquefaction could create massive displacements known as the ground oscillation during the earthquake, but the lateral and permanent displacements are small. Ground liquefaction failures occur due to the upward water flow when seismically induced EPWP dissipate. Some of the level ground liquefaction failures are high vertical settlement, floating low lands, sand boiling. Figure 1.7 indicates the cyclic mobility susceptible zone. It is possible to have cyclic mobility if the initial circumstances plot inside the shaded zone (Kramer, 1996).

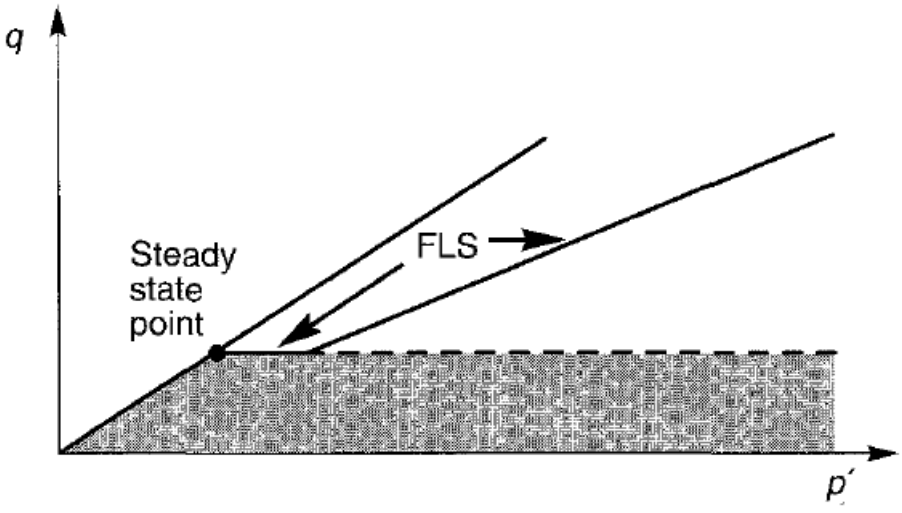

Figure 1.7. the cyclic mobility susceptible zone

(Source: Kramer, 1996)

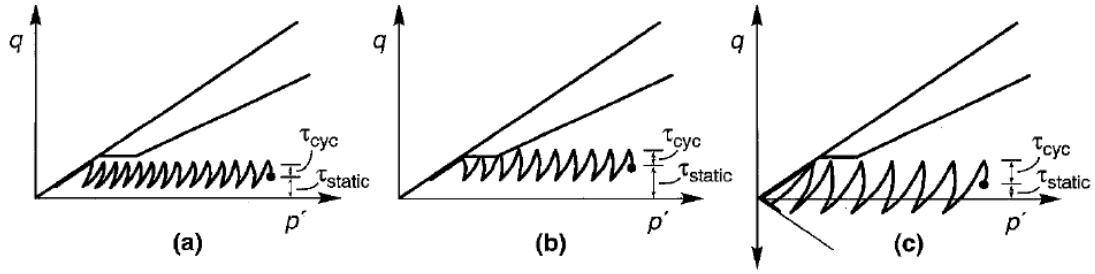

Figure 1.8. Three cases of cyclic mobility: a) without stress reversal and steady-state strength exceedance; b) without stress reversal with immediate periods of steady-state strength exceedance; c) with stress reversal without exceedance of steady-state strength (Source: Kramer, 1996)

1.3.2.3. Susceptible Soils to Liquefaction

All types of soils are not liquefiable. Therefore, the considered first step is to evaluate the liquefaction potential. Many factors are effective in the occurrence of the liquefaction phenomenon. Kramer provides the following criteria for evaluating liquefaction potential (Kramer, 1996).

1.3.2.4. Historical Criteria

Youd, 1984 after examining the soil of liquefied areas, concluded that liquefaction often occurs again in liquefied areas that the soil and conditions have changed. Investigations also showed that liquefaction occurred in specific areas of the earthquake epicenter (Kramer, 1996).

1.3.2.5. Geological Factors

Geological environments such as depositional environments, hydrological conditions, and soil strata age all affect soil liquefaction. Geological phenomena that cause soil uniform aggregation create loose soil mass and increases liquefaction

potentiality. Therefore, the older geological soil strata age decreases the liquefaction (Kramer, 1996).

1.3.2.6. Soil Texture and Structure

In the past, it seemed that liquefaction occurred only in sand. Later it was observed that the non-plastic silts and cohesionless coarse-grained soils are also highly susceptible to liquefaction. Moreover, liquefaction has been observed in gravels in undrained conditions. Laboratory and field observations show that liquefaction often occurs in grained soils. However, the well-grained soils are less liquefiable than the others because of the holes filled by finner particles. Therefore, the soil compression tendency is reduced, and less EPWP is generated. The particles shape is also effective in liquefaction. The soil with round-shaped particles experiences more compression than the soil with angular-shaped particles so, more EPWP is generated, and liquefaction possibility is increased (Kramer, 1996).

1.3.2.7. Soil Initial Conditions

The EPWP generation is highly affected by initial soil density and stresses. Hence, liquefaction is highly related to the soil's initial conditions.

1.4. Loads on Buried Pipes

Buried pipes during their services may be affected by various loadings depending on the piping and geographical location. Some of these loads, such as embankment or seismic loads, generally enter through all the pipelines, and some others, like point loading or ground sliding, may be occasional. There are some possible loadings in pipelines that can be summarized as follows:

- Embankment loads
- Traffic loads
- Overloads
- Hydrostatic pressure inside the pipe
- The weight of the pipe and fluid inside it

- The loads caused by temperature changes
- The loads caused by changes in soil volume around the pipe due to temperature changes
- The loads caused by seismic vibrations
- The loads caused by indirect effects of earthquake as, liquefaction, sliding, soil drifting, uplift and fault.

Besides, it is possible that pipelines are damaged by chemical erosion due to the soil conditions and pipe contents (Alliance, 2001).

1.5. Soil Liquefaction Induced Buried Pipes Uplift

The flotation of buried pipes in saturated sediments after intense earthquakes was a relatively new phenomenon for scientists to examine in the last decade. Sands as granular materials are susceptible to compaction during an earthquake. In saturated deposits, the presence of pore water prevents volume decrease. Inadequate drainage as a result of poor permeability and brief loading duration results in a practically undrained state. This undrained state, along with a propensity to diminish the volume of soil skeleton, contributes to the accumulation of PWP.

As a result, the effective stress of these cohesionless soils decreases, as does their shear resistance. By continuing to generate EPWP, the effective stress progressively decreases that might result in liquefaction. The flotation of the pipeline is achieved through EPWP beneath it and soil shear resistance reduction above it (Figure 1.6).

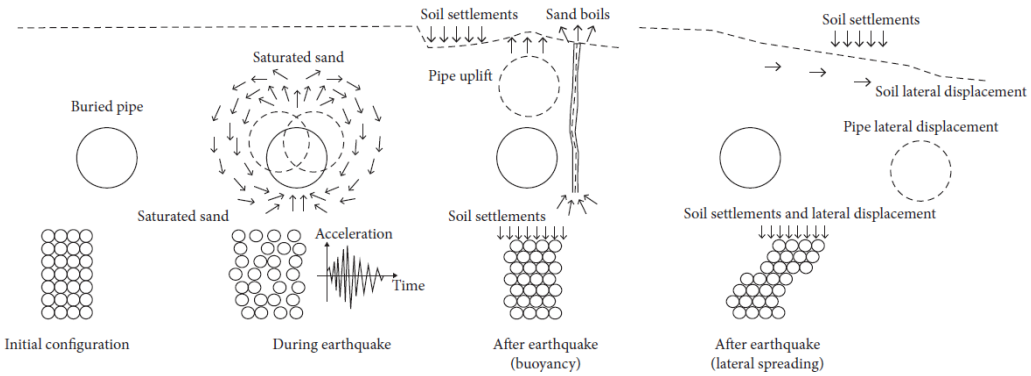

Figure 1.9. Simplified scheme of liquefaction-induced effects on buried pipelines (Source: Castiglia et al., 2019)

1.5.1. Remediation Methods

previous studies focused on protecting buried structures from damage due to soil liquefaction. Numerous alternative techniques of liquefaction remediation are discussed in general. However, some of these techniques are specialized in the protection of subterranean structures. The main concept behind these techniques is to decrease the liquefaction ratio (i.e., the ratio of the excess pore water pressure and the effective vertical stress, $r_u = \frac{\Delta u}{\sigma'}$).

In other words, these methods work on:

- Decrease the generated EPWP under the structure by soil densification or solidification.
- Keep the groundwater away from the underground structures by lowering the water table or dissipating the EPWP by surrounding drainage gravel.
- Increase the effective vertical stress under the structures by increasing its unit weight or its buried depth.
- Damping the earthquake shear loading by installing surround structural members (e.g., sheet piles, geosynthetic or overweight).

1.5.2. Sand-Granulated Rubber Mixture

The size of the shredded rubber tire has a major effect on the performance of the soil/sand-rubber combination. According to ASTM D6270-08 and ASTM D5681-18, waste tire rubbers can be classified as granulated rubber, powdered rubber, coarse shreds, tire chips, and tire-derived aggregate. Additionally, Table 1.1 summarizes the nomination and sizes of leftover tire rubber.

Numerous researches have demonstrated that a mixture of sand and tire (in chips, crumb, or shred form) is a potential new approach for geotechnical engineering ground improvement. Studies on this composite material started in the 1990s. Then, the emphasis on research and application increasingly switched to the civil engineering industry. Granulated rubber (GR) is an elastic substance that absorbs less energy during the compression process. Sand-granulated rubber (SGR) mixes have a lower relative density and, as a result, are less interlocking than pure sand when compacted with the same force. This approach was recently developed as a liquefaction prevention strategy by researchers. Granulated rubber has been demonstrated to inhibit the generation of EPWP when subjected to seismic shaking. No doubt mixing GR to the sandy soil has the capability to reinforce the soil conditions, but the detailed application to practice has not been well guaranteed. Numerous numerical and laboratory studies performed on this topic indicate the importance of correct knowledge of this phenomenon (Ecemis et al., 2021).

Table 1.1. Waste tire rubber is classified according to its size (Source: Liu et al., 2020).

ASTM D6270-08 [18]		
Designation	Shape	Size
Granulated rubber	Non-spherical	<0.425–12 mm
Ground rubber	Non-spherical	<0.425–12 mm
Powdered rubber	Non-spherical	<0.425 mm
Rough shreds	–	>500 × 50 × 50 mm, but <762 × 50 × 100 mm
Tire chips	Basic geometrical shape	12–50 mm
Tire-derived aggregate	Basic geometrical shape	12–305 mm
Tire shreds	Basic geometrical shape	50–305 mm
Whole tire	–	Unprocessed

1.6. The Purpose of This Study

In this thesis, finite difference models of buried pipes in Sand-Granulated Rubber (SGR) mixture were performed by adopting the constitutive soil model UBCSAND Version 904aR (Beaty and Byrne, 2011) to the commercially available computer code FLAC2D version 7.0 (Itasca, 2011). First, we presented a precise explanation of the accepted numerical model for buried pipes concerning the model verification against previously performed 1-g shaking table results (Ecemis et al., 2021). After verifying the numerical modeling and calibration of the constitutive model for infill material, a series of parametric simulations were prepared to investigate the model's geometric parameters such as burial depth, pipe diameter, and maximum input excitation amplitude (a_{max}) on liquefaction-induced pipe uplift. The buried pipe's failure mode was investigated according to its burial depth ratio and divided into shallow and deep failure mechanisms. Finally, using the parametric simulation results, an analytical formula was proposed to estimate the maximum pipe uplift in the SGR mixture with a granulated rubber size of 2.5-5 mm and a ratio of 30%.

1.7. Thesis Organization

Based on the objectives and scope of the research, this study consists of five chapters:

Chapter 1 provides a brief introduction to buried lifelines and their damages in past earthquakes, liquefaction mechanism, the scope, and the purpose of the present thesis.

Chapter 2 provides a comprehensive literature review of the seismic behavior of buried pipes. In this chapter, previous experimental and numerical studies related to the liquefaction-induced uplift of underground structures and buried pipes, using granulated rubber as reinforcement material and theoretical formulation to estimate the buried pipes' uplift, have been discussed.

Chapter 3 describes the assumptions and principles of numerical modeling. Brief explanations about the FLAC2D and its applied basis are provided. Soil constitutive models for static and dynamic analyses are introduced, and the superiority of the

UBCSAND advanced model is expressed. Finally, numerical modeling is verified using the 1-g shaking table result to calibrate the UBCSAND constitutive model.

In **Chapter 4**, a parametric study was conducted to investigate the impact of pipes geometric parameters such as the pipe diameter, the pipe buried depth, and also the amplitude of the maximum input acceleration on pipe uplift and liquefaction potential when the Sand-Granulated Rubber (SGR) mixture was placed as a filling material. In the following, an analytical formula is proposed to estimate the liquefaction-induced uplift of buried pipes. Finally, the soil failure mode is categorized according to the pipe's burial depth.

In **Chapter 5**, the main conclusions and suggestions for future studies are presented.

CHAPTER 2

LITERATURE REVIEW

2.1. Introduction

Numerous earthquakes, including the Niigata earthquake of 1964, the Alaskan earthquake of 1964, the Loma Prieta earthquake of 1989, and the Hyogoken-Nambu earthquake of 1995, have demonstrated the detrimental effects of soil liquefaction on buried pipelines (Giridharan et al., 2020). Furthermore, Observations of liquefaction-induced uplift of subterranean structures such as pipelines and manholes have been made during the Great East Japan earthquake. (Tokimatsu et al., 2011). Numerous studies, both experimental and Numerical, have been conducted to explain the seismic behavior of buried buildings and pipes in liquefiable soil, as well as the numerous characteristics that affect pipeline uplift (e.g., Ling et al., 2003; Byrne et al., 2004; Liu and Song, 2006; Chou et al., 2011; Saeedzadeh and Hataf, 2011; Chian and Tokimatsu, 2012; Huang et al. 2014; Zhai et al., 2014; Chian et al. 2014; Zhou et al., 2015; Sharafi and Parsafar, 2016; Hu et al., 2018; Castiglia et al., 2019; Mahmoud et al., 2020; Chen et al., 2020; Castiglia et al., 2020; Ecemis et al., 2021). In this chapter, investigation and obtained outcomes about the uplift behavior of pipelines buried into the liquefiable soil have been discussed.

2.2. Literature Review

2.2.1. Shaking Table Test

Castiglia et al., (2019) performed shaking table tests to study the effectiveness of gravel bags to increase the stability of pipelines subjected to uplift in liquefiable soils. Moreover, Castiglia et al., (2020) used geogrid sheets as a remedy for the liquefaction-induced uplift of buried pipelines.

Four 1-g shaking table experiments were conducted to determine the efficiency of innovative remedial techniques for increasing the stability of onshore pipelines subjected to uplift in liquefiable soils during seismic excitation (Castiglia et al., 2019). Test T1_1

was the reference test to quantify the pipe's uplift amount, and T1_2 was considered to be a repeatability check of the T1_1 result. T1_3 and T1_4 were conducted by adding a gravel bag on the top and bottom of the pipe as a mitigation measure. The purpose of this study was to determine how the subterranean structure will behave under cyclic loads in the event of liquefaction. As a mitigation method, a gravel bag was put above and below the pipe (Figure 2.1).

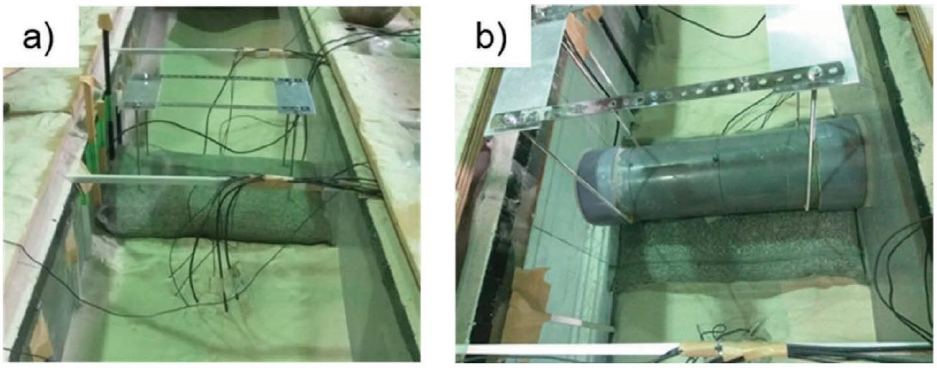

Figure 2.1. Gravel bag details. a) above and b) below the pipe
(Source: Castiglia et al., 2019)

A camera was mounted in front of the transparent wall of the soil box, which was attached to the moving base, and images were collected during shaking. Figure 2.2 compares the original and deformed shapes of T1_1 and T1_2 samples.

In samples including a remedial treatment, soil deformation surrounding the pipe is minimal, and the pipe's uplift is nearly nonexistent. Figure 2.3 illustrates the cumulative vertical displacements of the pipe caused by the shaking stages and dissipation phases. Liquefaction begins at 0.2 g, but considerable uplift occurs at 0.3 g, when the liquefaction impacts more layers of the soil deposit.

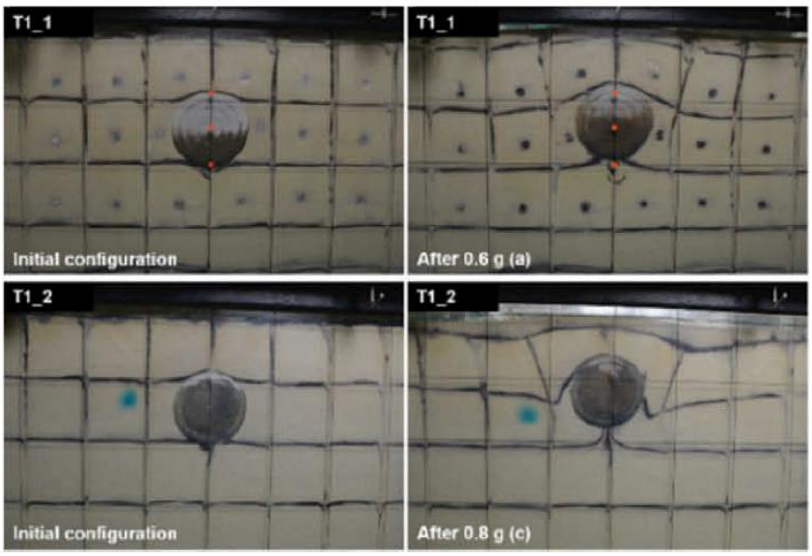

Figure 2.2. Comparison between initial and deformed configuration

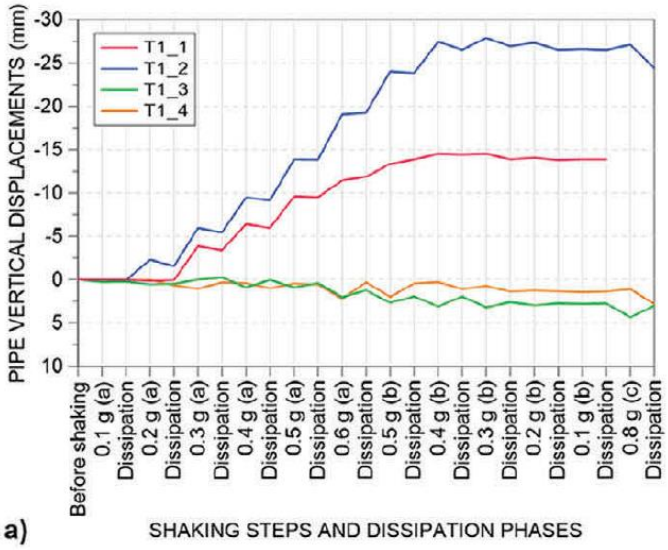

Figure 2.3. Cumulative uplift of pipe

The effectiveness of these novel approaches is proved by comparing the performance of remedied samples to those of pipes without remediation. Both recommended systems produce acceptable outcomes. Due to the presence of greater deformations, increased excess pore water pressures, the necessity of connecting the pipe to the gravel, and the depth of excavation, the arrangement with the gravel above the pipe was determined to be the most effective remedial method in this specific study.

2.2.2. Centrifuge Test

Huang et al. 2014, investigated the uplift mechanism of buried pipes by considering the seismic loading-induced EPWP generation in sands. They conducted two series of 30g centrifuge tests (Figure 2.4); each consisted of two buried aluminum pipes with a unit density of 27 g/cm^3 simultaneously. The first pipe with the free-ends was installed to get the pipes uplift amount, and the second one was fixed by rods to measure the uplift force accurately. In the first sample, pipes were placed in 20 mm depth (equal 0.5D), and in the second sample, in 80 mm depth (equal 2D) (Figure 2.5). The Fujian standard sand with 60 percent relative density (Dr=60%) was used in this investigation. Also, three types of loading, including El-Centro wave, Taft, and Zhejiang seism wave, were considered to study seismic loading intensity accurately. This probe was divided into two parts: the study of free pipe liquefaction-induced uplift behavior and propose an equation to predict the buried pipe uplift (Huang et al., 2014).

Figure 2.4. Centrifuge setup
(Source: Huang et al., 2014).

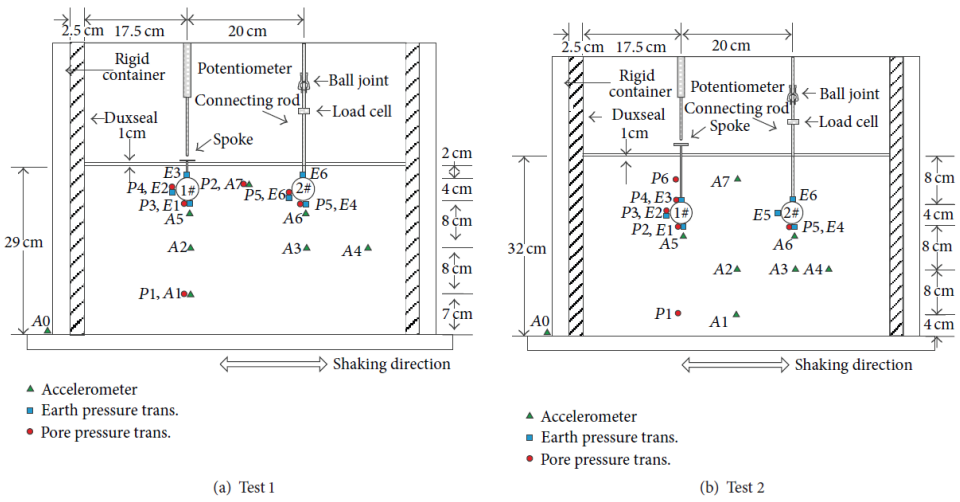

Figure 2.5. The layout of pipes and instruments in the experimental study (Source: Huang et al., 2014).

According to the outcomes, with the seismic loading initiation, the EPWP was generated, and the EPWP started to dissipation by excitation ending (Figure 2.6). It should be noted that the soil full liquefaction occurrence ($r_u=\frac{\Delta u}{\sigma'}=1.0$) was not necessary for the buried pipe uplift initiation. As in some seismic loading where the loading intensity was not enough to occur full liquefaction, the buried pipe uplift phenomenon was observed, indicating that uplift also occurs in incomplete soil liquefaction (Figure 2.6).

According to Figure (2.7), It was observed that by increasing the seismic loading intensity, the amount of EPWP generation increased, and the dissipation velocity of EPWP was reduced after excitation. In some cases, it was perceived that the EPWP generation has continued even after the loading stopped. Although some researchers believed that the buried pipe uplift initiation was related to seismic loading intensity, and the EPWP generation has a negligible effect on this initiation, Huang, by examining the results of centrifuge tests with different loading patterns, found that the buried pipe uplift initiation in liquefied soil is not related to seismic loading. In other words, input excitation causes the EPWP generation, and by obtaining the sufficient liquefaction ratio ($r_u=\frac{\Delta u}{\sigma'}$) uplift phenomenon starts (Huang et al., 2014).

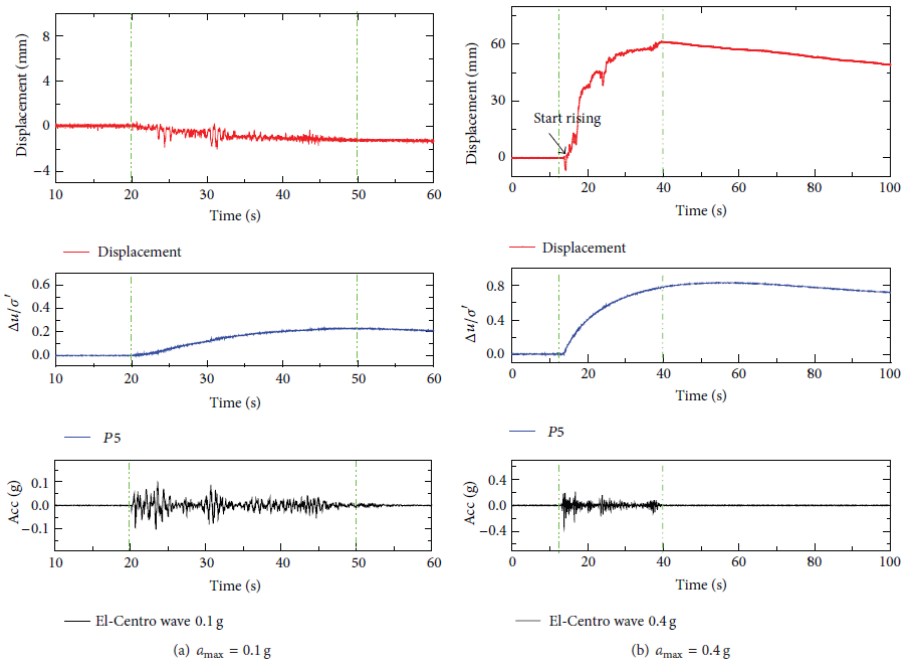

Figure 2.6. Uplift of pipe in test 2 under El-Centro wave

(Source: Huang et al., 2014).

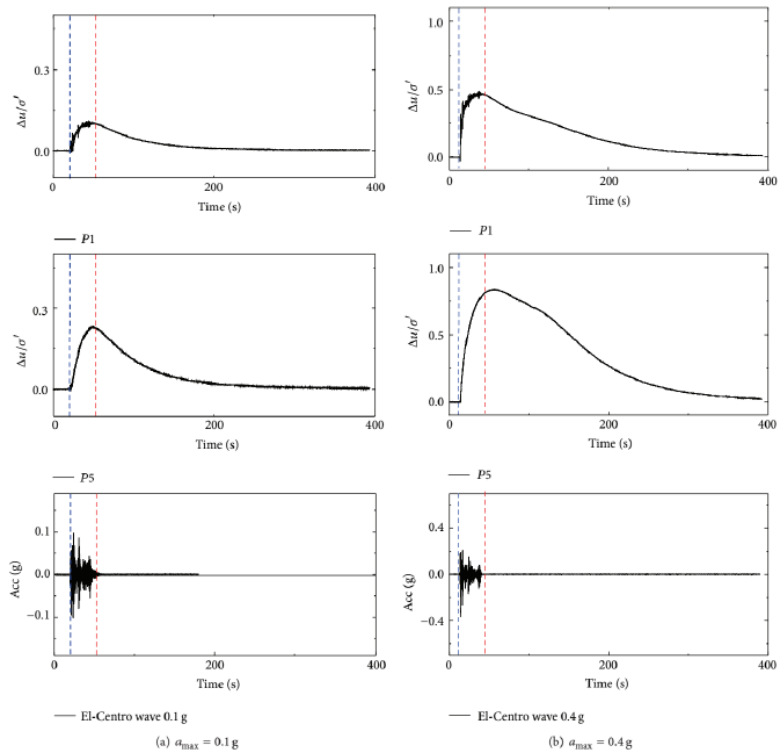

Figure 2.7. Liquefaction Ratio ($r_u=\frac{\Delta u}{\sigma'}$) in test 2 under El-Centro wave

(Source: Huang et al., 2014).

2.2.3. Numerical Modeling

Saeedzadeh and Hataf, 2011 investigated the pipe geometric variables and soil geotechnical properties on the buried pipe uplift behavior in the sand alluvium during the earthquake. The PLAXIS2D finite element software was used for this purpose (Figure 2.8). In this study, the used soil model was the Hardening Soil (HS) model, which is based on plasticity theory. This model considers soil dilation and yield cap, making this model superior to the older Duncan and Chang's hyperbolic model (Duncan and Chang, 1970). The saturated Nevada sand with relative densities (D_r) of 40, 50, 60, 70 percent was used to study the buried pipe uplift behavior. Moreover, buried pipes with 1, 2, 3 m diameters in the depth of 0.5, 1, 1.5 m were modeled based on Figure 2-5 (Saeedzadeh and Hataf, 2011).

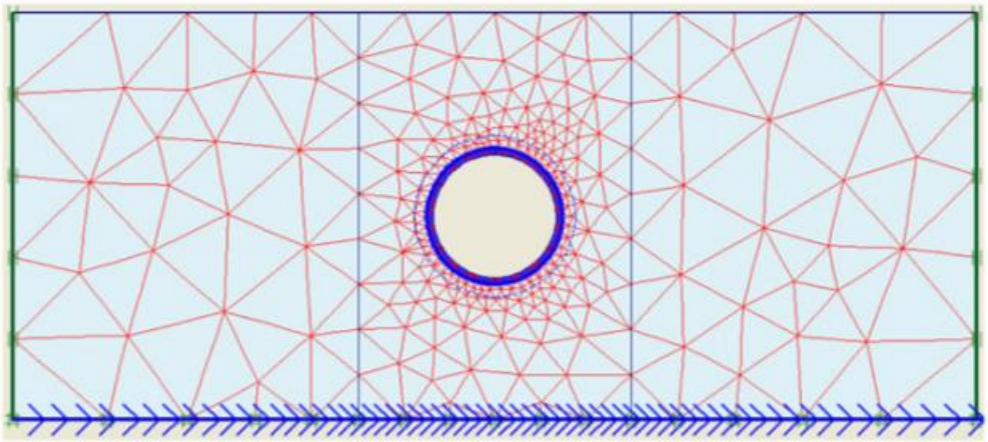

Figure 2.8. Finite element mesh in PLAXIS2D software
(Source: Saeedzadeh and Hataf, 2011)

They concluded that by examining buried pipes in diameters of 1, 2, and 3 m, buried in Nevada sand of 40% density ratio by fixing the burial depth at 3 m, under a sinusoidal excitation with an amplitude of 0.6g and frequency of 3 Hz for 10 s, by increasing the pipe diameter, the uplift of pipe (normalized by pipe diameter) increases. In contrast, the rate of this increase decreases, as shown in Figure 2.9 (Saeedzadeh and Hataf, 2011).

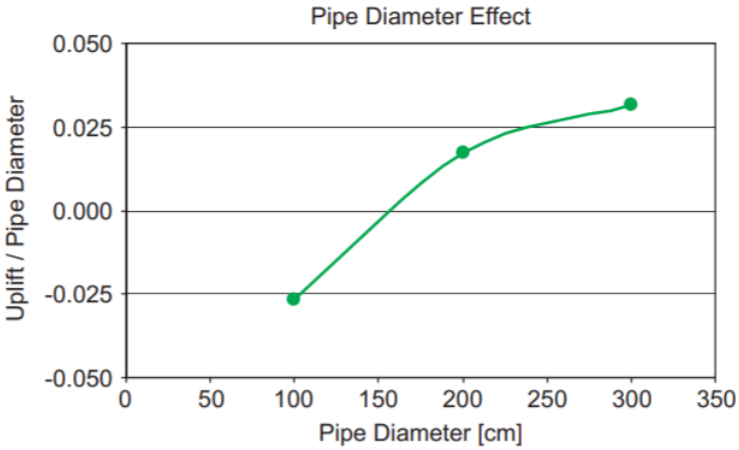

Figure 2.9. Pipe diameter effect on uplift

(Source: Saeedzadeh and Hataf, 2011)

By investigating the buried pipe behavior with a diameter of D=3 m in the three different depths 1.5, 3, 4.5 m (i.e., D/2, D, and 3D/2, respectively) under the Tabas earthquake record, They concluded that as burial depth and the overburden pressure increase, the pipe uplift diminishes. Moreover, this reduction rate decreases after the burial depth equal to D (pipe diameter), as seen in Figure 2.10 (Saeedzadeh and Hataf, 2011).

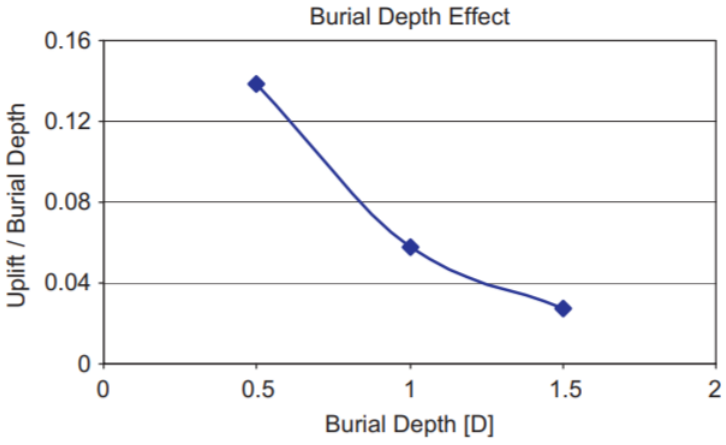

Figure 2.10. Burial depth effect on uplift

(Source: Saeedzadeh and Hataf, 2011)

Chian and Tokimatsu, 2012 studied the manholes' and buried pipes' uplift behavior in liquefiable soil by FLAC (Fast Lagrangian Analysis of Continua) software. In this study, in order to predict the sand liquefaction accurately, Wang's nonlinear bounding surface plasticity constitutive model was used, which is the proper model for the dilation and contraction behavior of sand. Regarding the soil layers diversity, a sample sand alluvium and a buried pipe with a diameter of 1 m at 4 m depth were used in the numerical analysis, Figure 2.11. Numerical modeling was simulated under plane strain conditions. Regarding Chian's previous studies, the buried structures uplift started by the EPWP generation, which was compatible with the numerical modeling results. EPWP generation, along with the production of surplus force under the buried structure, decreased the above soil shear strength and caused the uplift initiation. Also, by studying the obtained numerical results of FLAC, it was observed that by the end of the seismic loading, even the EPWP was not dissipated entirely, the buried structure uplift stopped, that was against the structure buoyancy in the viscous liquid, that the uplifting process had to continue even after the dynamic loading ended, Figure 2.12 (Chian and Tokimatsu, 2012).

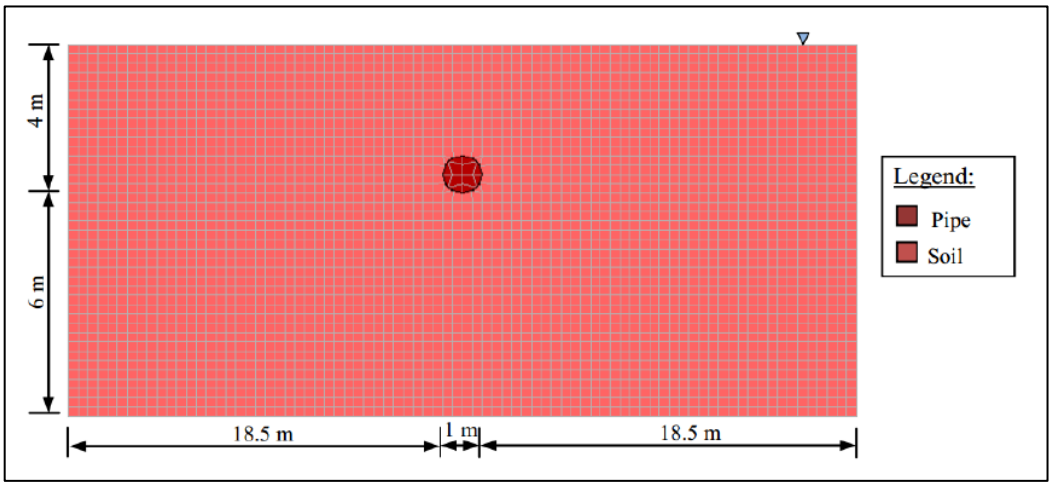

Figure 2.11. Model layout with buried pipe
(Source: Chian and K. Tokimatsu)

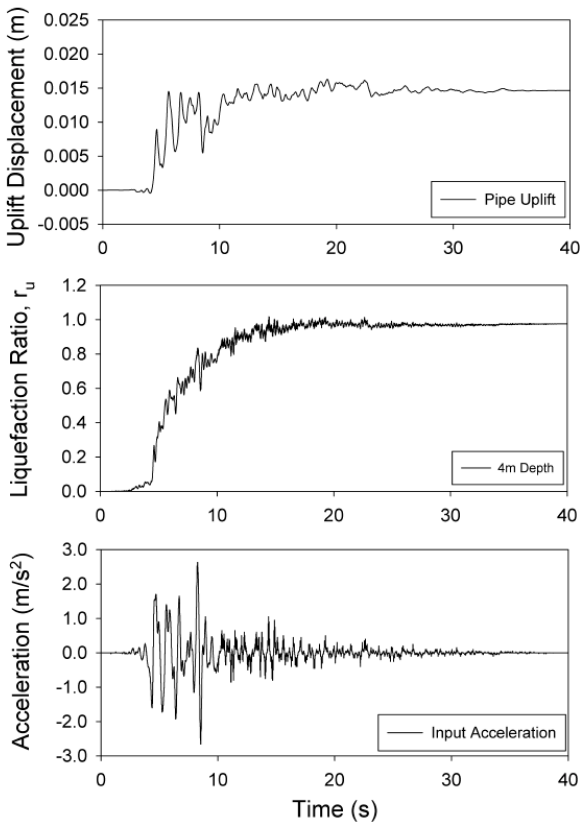

Figure 2.12. Uplift displacement of pipe and liquefaction ratio (r_u) at 4m depth (Source: Chian and K. Tokimatsu)

Chian et al. 2014, using the centrifuge tests and numerical modeling, aimed to find the explanation for the mechanism of the behavior of the pipelines buried in liquefied soils layer. In the experimental study, the centrifuge with a gravity of 66.7g used to 75 mm pipe in the model be like the 5 m pipe in reality (Figure 2.13). The used sand in tests was the Huston sand with Dr=45%. The Wang constitutive model and FLAC2D software were used in numerical analyses (Figure 2.14). The Wang model is nonlinear and based on the plasticity bounding surface of the sand and has established sand's contracting and dilating behavior under cyclic loading (Chian et al., 2014).

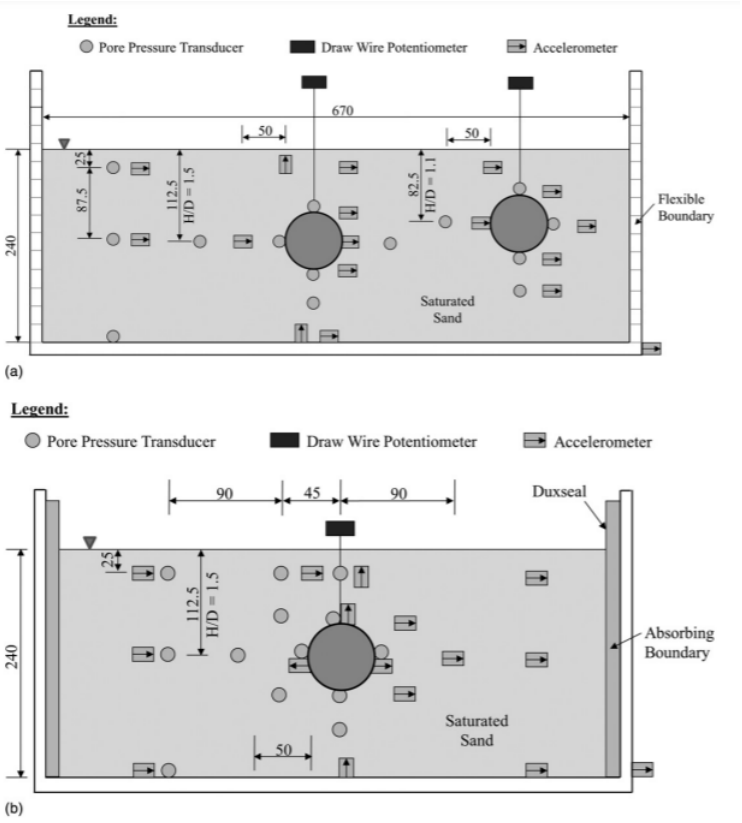

Figure 2.13. Pipe and instrument layouts in centrifuge tests

(Source: Chian et al., 2014)

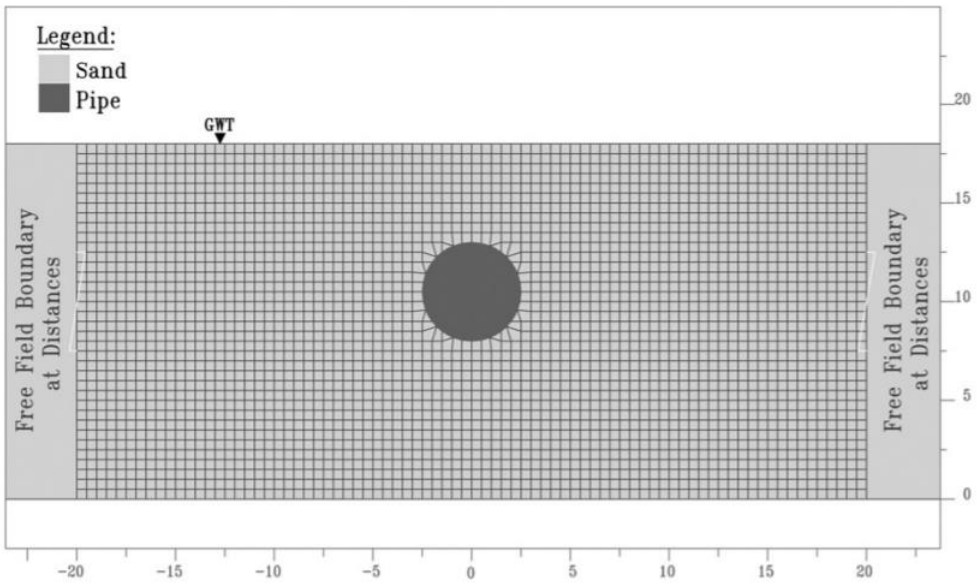

Figure 2.14. Numerical modeling of buried pipe (dimensions in meters)

(Source: Chian et al., 2014)

By comparing experimental outputs with numerical simulation results, Chian concluded that by the EPWP generation initiation in soil mass because of dynamic loading, the shear strength of soil particles decreased and caused the uplift of buried structures and its buoyancy in the soil mass. Also, this study revealed that EPWP is one of the effective variables in soil liquefaction and buried structure buoyancy. Based on the obtained results, they believed that the increasing process of pipe uplift was stopped by ending the seismic loading. However, by doing some experimental studies, Huang observed that the increasing process of the pipe uplift might continue even after the earthquake stops (Huang et al., 2014). He found that the EPWP increasing process was related to the seismic waves return from the model boundaries and the inability of these boundaries to absorb the seismic waves. At the end of the study, Chian, using the obtained numerical and laboratory results, investigated the effect of the great earthquake in Japan, 2011 in Urayasu city on buried structures. The soil of the area consisted of highly liquefiable soil (site I) and non-liquefiable soil (site II) (Chian et al., 2014).

By comparing the liquefiable and non-liquefiable zone results, Chian concluded that the generated EPWP causes floating and uplifting of buried structures. In the liquefiable zone, earthquake initiation often caused a heighten in the liquefaction process, but in the non-liquefiable zone, this increase was not observed in EPWP (Figure 2.15). Also, considering the greater number of buried structures failures in the liquefied area than in the non-liquefied area, it concluded that earthquake waves were not the main cause of underground structures failure. Liquefaction, a phenomenon caused by earthquake waves, was the main cause of damage to buried structures (Chian et al., 2014).

2.2.4. Soil-Granulated Rubber Mixture as a Remedial Material

Scrap tires in various forms such as complete tires, shredded tires, chips, ground tires, or powder tire shapes have been used in a variety of geotechnical applications throughout the last three decades. One of the primary advantages of shredded tires is their economic effectiveness and environmental friendliness. While discarded tires improve the behavior of sand, they can be converted to shredded material for use in a variety of industrial applications.

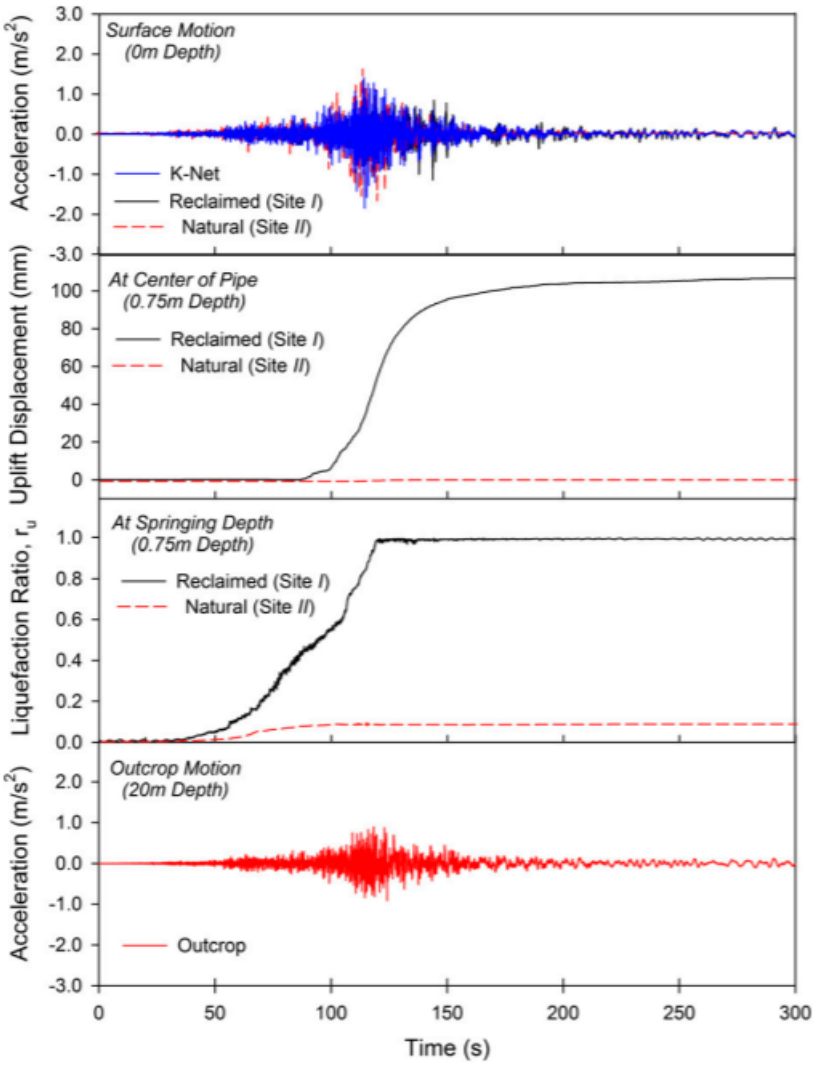

Figure 2.15. Pipe uplift, liquefaction ratio, and input acceleration time histories (Source: Chian et al., 2014)

Recently, researchers demonstrated that the SGR mixture is a novel strategy for preventing liquefaction and lowering EPWP generation during seismic shaking. (e.g., Uchimura et al., 2007; Yoshida et al. 2008; Neaz Sheikh et al., 2012; Kaneko et al., 2013; Bahadori and Manafi 2015; Jamshidi Chenari et al., 2017; Noorzad and Raveshi, 2017; Saberian et al., 2020; Ecemis et al., 2021).

Rubber has a great degree of flexibility, tensile strength, durability, and a low specific weight, making it ideal for geotechnical tasks (Liu et al., 2020). Numerous researches have established the benefits of tire recycling in geotechnical engineering appliances by identifying a feasible method of recycling waste tires, such as subgrade

backfilling, landfilling, and retaining walls (e.g., Uygunoglu and Topçu, 2009; Tafreshi et al., 2012; Neaz Sheikh et al., 2012; Su et al., 2015; Liu et al., 2018; Morales et al., 2018).

Yoshida et al., (2008), using 1-g shaking table, studied the use of permeable recycled materials to improve soil properties in reducing liquefaction, which caused manhole buoyancy during the Niigata earthquake. The recycled materials that used in this investigation were granular rubber extracted from wasted tires and grains obtained from wasted reinforced concrete. The material was placed inside the bag and located around the manholes, as shown in Figure 2.16 (Yoshida et al., 2008).

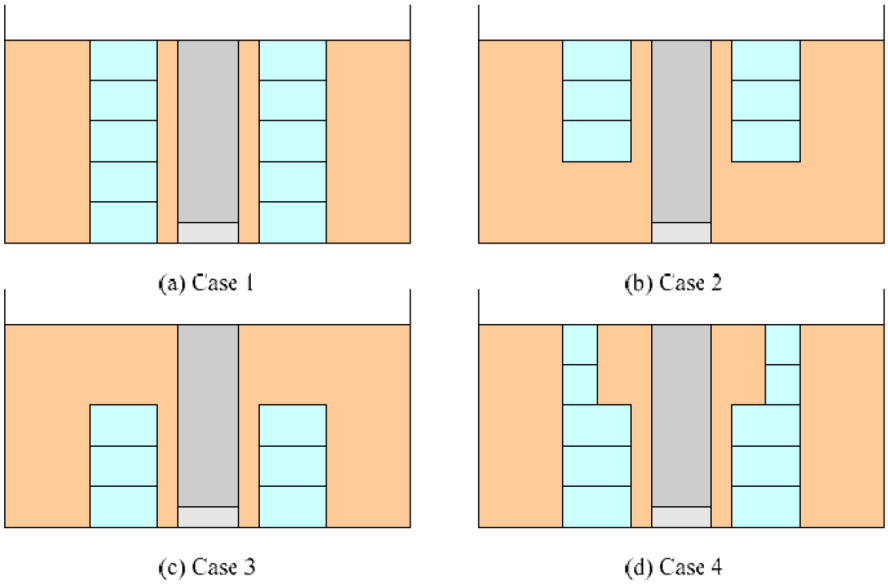

Figure 2.16. Manhole and Recycled material bags layout
(Source: Yoshida et al. 2008)

The granulated rubber size was between 10 to 16 mm, and the size of the crushed concrete was considered about 2.5 to 5 mm. The used sand was the loose liquefiable Silica sand No.7 with D_r=35 %. These tests were conducted in four models, as shown in Figure 2-13. The sample results can be seen in Figure 2.17.

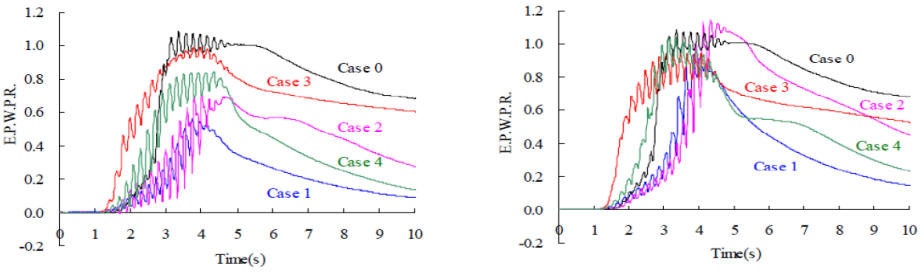

(a) Tire chips [P1] (b) Recycled gravels [P3]

Figure 2.17. Excess pore water pressure amount for cases
(Source: Yoshida et al. 2008)

As seen in Figure 2.14, the reduction of EPWP increased in case 1, and by using the granular rubber, this reduction intensified. This was because of the full coverage around the manhole, which was armed with bags (case 1). The recycled materials packed in bags had high permeability and could dissipate EPWP during liquefaction. Soil reinforced with crumb rubber showed better performance than with granular materials. Therefore crumb rubber can be used as drainage materials instead of granular materials. By placing the granular materials in the bag inside the liquefiable soil, the soil was protected due to its permeability. Moreover, the manholes' buoyancy was controlled. Crumbed rubber kept high permeability even with increasing earthquake time because of the very low gravity and high elasticity.

Bahadori and Manafi, (2015) carried out a series of 1-*g* shaking table model tests at different percentages of sand–tire chips mixtures. They utilized Firoozkuh no. 161 sand in the tests, and the wet tamping sample preparation method was adopted. Figure 2.15 illustrates a shaking table device and its instrumentation. A rigid box with an inner dimension of 200 × 50 × 70 cm was used. Furthermore, a rigid plastic plate was fixed and sealed at the center of the box to separate clean sand and Sand-Tire Chips (STCh) mixture parts (Figure 2.18). Therefore, two tests might be evaluated concurrently using the same input acceleration. (Figure 2.18).

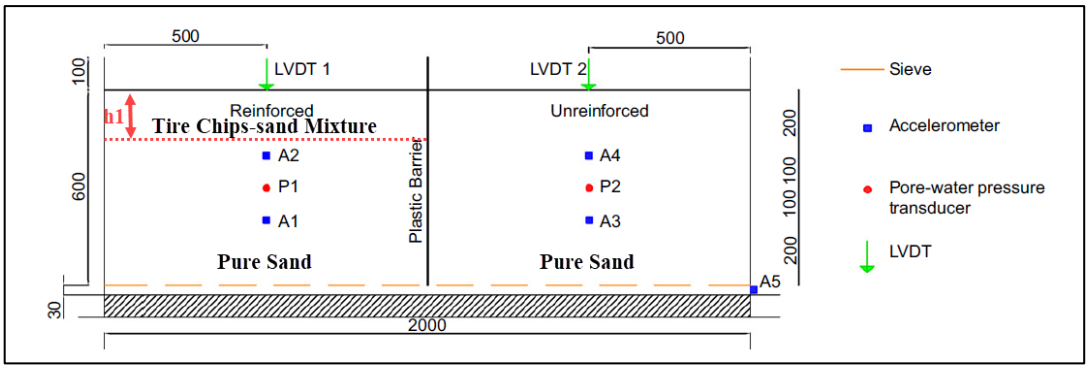

Figure 2.18. Model and instrumentation

As mentioned, tire chip was used as a soil reinforcement material. Tire chips (TChs) were made from waste tires that had been broken to pieces and sieved by an industrial tire-shredder system. As is typical of rubber, the tire chips particle has a negligible water absorption capacity. Additional tire chip properties are specified in ASTM D6270-98 (ASTM, 1998). Base vibration with uniform amplitude and a frequency of around 2 Hz was manually applied to the models.

Table 2.1. Tests properties

	Test a	Test b	Test c	Test d
Reinforced depth, *h*: mm	600	600	600	600
Tyre chips content ratio, *P*	10	20	30	40

Figure 2.19 shows the EPWP ratio ($r_u=\frac{\Delta u}{\sigma'}$) time history of two reinforced and unreinforced parts. It can be observed that the increase in tire chips ratio decreases the maximum EPWP ratio considerably. Also, the STCh mixture causes the time retardation of the EPWP to reach a peak value.

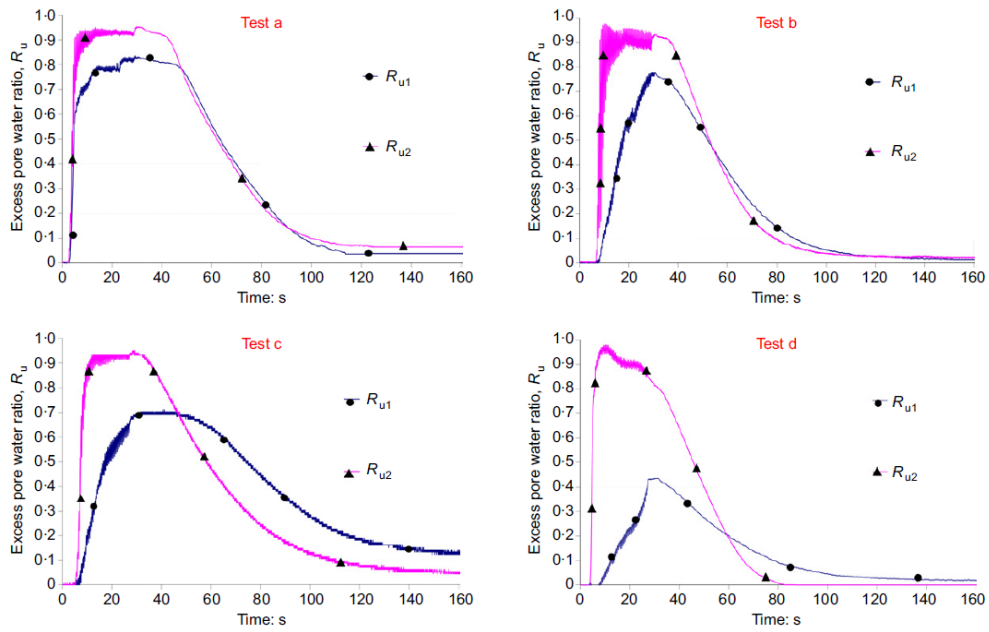

Figure 2.19. Time histories of EPWP ratio ($r_u=\frac{\Delta u}{\sigma'}$)

The results showed that using TCh basically reduces PWP generation due to liquefaction. Also, the mean damping ratio is increased with increasing TCh content in the STCh mixture. Generally, reinforcing soil with TCh is found to decrease the deformations caused by liquefaction considerably. Also, the reinforcing depth has a considerable effect on the liquefaction mitigation outcomes.

Noorzad and Raveshi, (2017) conducted triaxial compression tests on sand–tire crumb mixtures with varying percentages of tire crumbs (0, 5, 10, 20, and 30%). The sand–tire combination was predicted to have a D_r of approximately 70%. This study examined the effects of tire size, tire content (by weight), and confining pressure on the sand's behavior.

Uniform quartz sand was utilized, and to classify the test sand, ASTM D422 (2004a) particle size measurement was used; the grain size distribution of this sand is depicted in Figure 2.20. The uniformity coefficient (Cc) was determined to be 1.03 and the curvature coefficient (Cu) to be 1.8. According to the unified soil classification system (USCS), the sand might be categorized as SP. The sand's maximum and minimum unit weights were 17.3 and 14.7 kN/m^3, respectively.

The Tire-Derived Aggregate (TDA) employed in this investigation was a manufactured material created by shredding discarded tires with specialized equipment.

Two distinct sets of TDA (T1 and T2) were used (Figure 2.21). T1 and T2 samples were classed as granulate rubber (GR) and powder rubber (PR), ٥n accordance with CEN Workshop Agreement (CWA) 14243-2002 (2002). The specific gravity of the tire crumbles utilized in this experiment was 1.12.

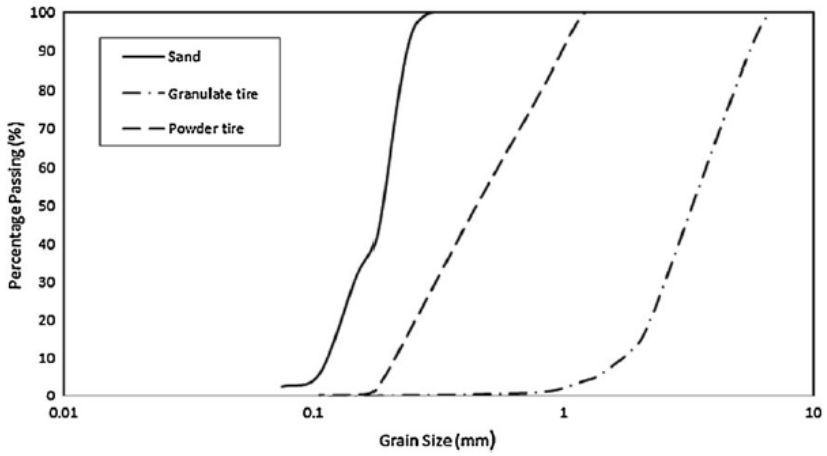

Figure 2.20. Distributions of grain size in pure sand, granulate, and powder tire (Source: Noorzad and Raveshi, 2017)

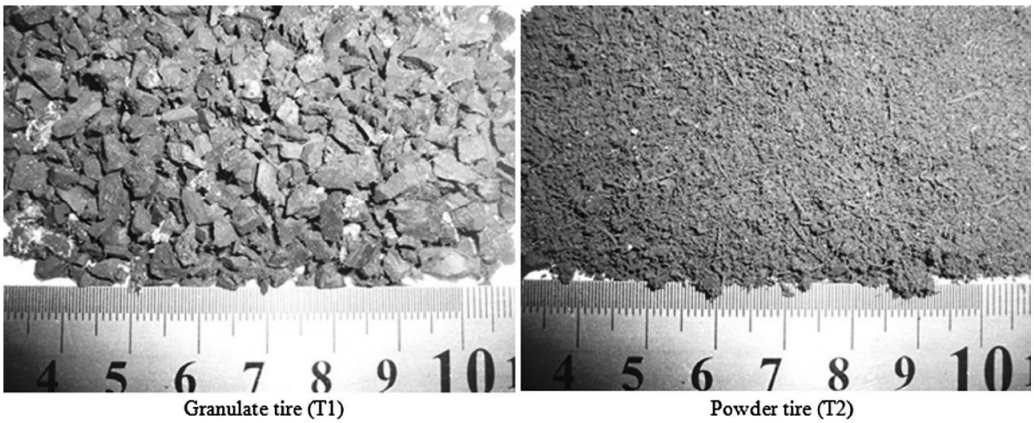

Figure 2.21. Images of tire crumbs T1 and T2 (Source: Noorzad and Raveshi, 2017)

The samples were compacted in five layers and were subjected to testing at 50, 100, and 200 kPa cell pressure. For all tests, the sample was loaded at a 0.30 percent per minute strain rate. The tests were carried out until the load peaks or until the 15% strain is reached.

Figure 2.22 illustrates typical failures of unreinforced and reinforced sand samples. As demonstrated in this photo, unreinforced samples fail along a shear plane at an angle of $(45 + {}^{\varphi}/_{2})$, whereas reinforced samples bulge. Additionally, the bugling of samples rose as the tire's content increased. The sand–tire composite material is a cohesive substance. As a result, its composition bulges under failure conditions.

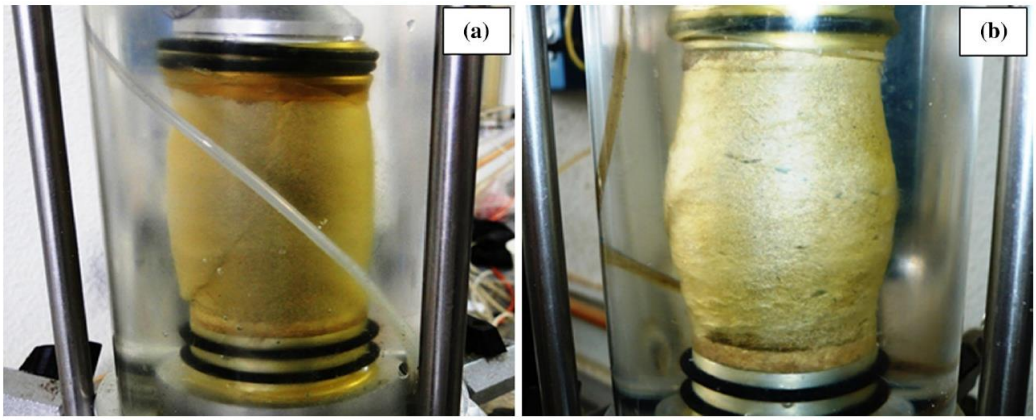

Figure 2.22. Samples failure state a) unreinforced sand, b) reinforced sand
(Source: Noorzad and Raveshi, 2017)

Unlike some previous studies, the mixture's shear strength was decreased with the increment of granulated rubber ratio. The friction coefficient between tire crumbs and sand has an effect on the decrement in the peak strength of sand–tire mixes. The peak strength of sand–tire combination is likewise decreased by lowering this parameter.

In compared to samples reinforced with powder tire (T2), those reinforced with granulate tire (T1) exhibited a higher peak strength, a lower axial strain at failure, and a better reduction in post-peak strength loss. The addition of tire crumbs decreased the reinforced sand dilatancy. The ratio of tire crumb size to mean sand diameter was also significant in this regard. The amount of tire crumbs in the combinations had a significant effect on the rigidity of reinforced sand. The rigidity diminishes proportionately to the

percentage of tire crumbs added. Raise the proportion of tire crumbs in the sand–tire mixtures to decrease the internal friction angle and increase the cohesion, respectively.

Ecemis et al., (2021) investigated a series of shake table tests to quantify the scrap tire granule's seismic behavior and mitigation aspect mixed with sand during liquefaction. Dynamic experiments on a completely saturated Sand-Granulated Rubber (SGR) mixture with small diameter buried pipelines are conducted under 1-g conditions. The experiments investigate three distinct granulated rubber dimensions of 2.5-5, 5-10, and 10-15 mm, as well as granulated rubber ratios of 10, 20, and 30%.

The fine silica sand mixed with scrap Granulated Rubber (GR) was used as a backfill material around the pipe. The particle size distribution curves of clean sand, different sized GR, and Sand-Granulated Rubber (SGR) mixtures are shown in Figure 2.20. The soil was defined as poorly graded sand (SP), according to the Unified Soil Classification System (USCS).

According to ASTM D6270-08 (2012), the scrap rubbers employed in this study comprises of the granulated rubber size (non-spherical and range in size from 0.425 to 12 mm according to Table 1.1). The physical parameters of the SGR mixes utilized in the studies are listed in Table 2.2.

A 65 cm height fully saturated silica sand layer was placed into the laminar box by the hydraulic filling method, which simulates the process of alluvial deposition of soils in rivers/lakes that of hydraulic fills. To densify the soil, the laminar box was shaken for several minutes at various accelerations. Then, a loose sand or SGR layer was obtained inside the laminar box. The dense sand layer corresponds to the original, non-liquefiable ground. Above the dense sand layer, the first 10 cm of SGR mixture was formed at a prescribed ratio by volume. The average saturated density of the mixture throughout the depth is shown in Table 2.2. A model of buried pipe was placed in this situation. The box was then filled to a depth of 65cm with an SGR mixture. After establishing the dry combination, water was carefully added to obtain a fully saturated sample.

In Tests 1–3, only the free ends of the pipe were inserted inside the loose, clean sand to determine the effect of acceleration level on buried pipes. The plan and side views of the free ends pipe design and instrument layout are shown in Figure 2.24. No pipe was placed in Test 4. In Tests 5–13, both fixed and free ends pipes were immersed in the SGR mixture at the same acceleration level to determine the influence of a soft backfill material on buried pipe reaction during and after liquefaction.

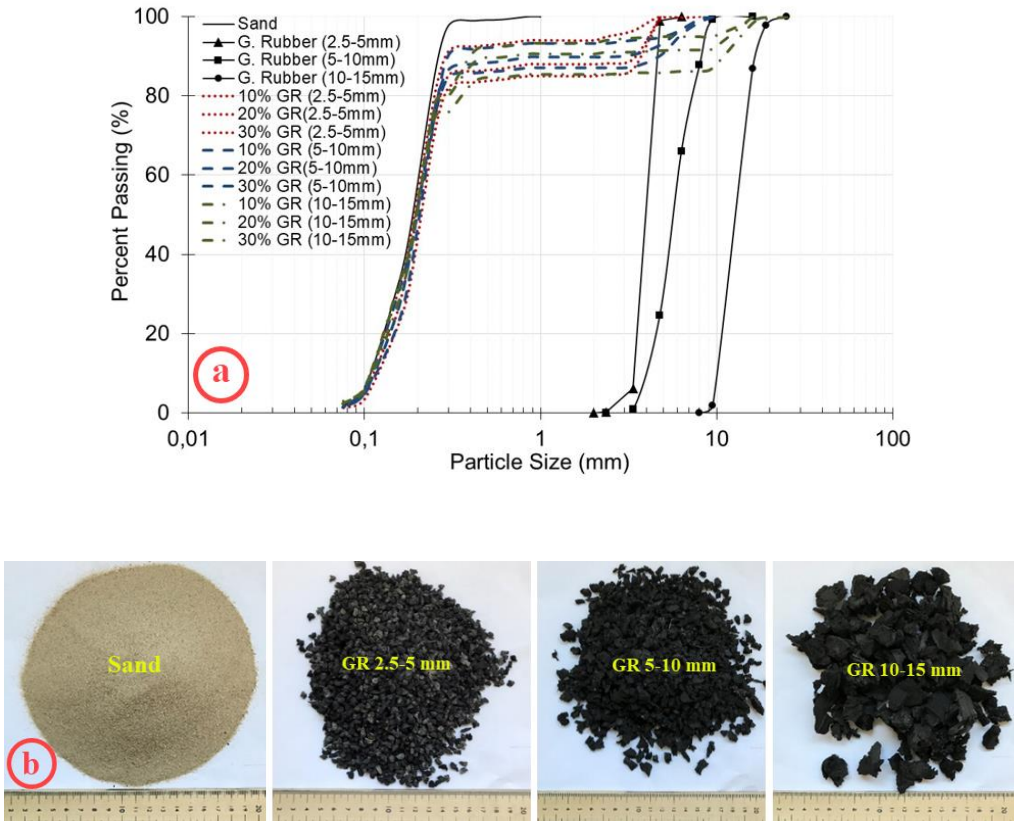

Figure 2.23. (a) Particle size distribution of the sand, GR, and SGR mixtures used in the tests, and (b) A sample of silica sand and GR (2.5-5 mm, 5-10 mm, 10-15 mm) utilized in the studies to surround the pipes.
(Source: Ecemis et al., 2021)

Table 2.2. Physical properties of SGR mixtures
(Source: Ecemis et al., 2021)

Test No.	GR ratio (by volume)	GR ratio (by weight)	GR dimension	D_{10}	D_{50}	C_u	C_c	Sat. density	D_r *	Pipe
-	(%)	(%)	(mm)	(mm)	(mm)	-	-	(kN/m^3)	(%)	-
T1	0	0	-	0.12	0.19	1.71	0.91	20.90	33	Free pipe
T2	0	0	-	0.12	0.19	1.71	0.91	20.50	49	
T3	0	0	-	0.12	0.19	1.71	0.91	20.90	24	

(Cont. on next page)

Table 2.3. (cont.)

T4	0	0	-	0.12	0.19	1.71	0.91	20.90	37	No pipe
T5	10	6.76	2.5-5	0.11	0.2	2.0	1.31	19.27	26	Fixed /free pipes
T6	20	10.12	2.5-5	0.11	0.2	2.0	1.34	19.16	35	
T7	30	14.35	2.5-5	0.12	0.2	1.91	1.28	18.65	39	
T8	10	4.74	5-10	0.12	0.2	1.83	1.23	20.08	29	
T9	20	9.08	5-10	0.11	0.2	2.10	1.18	19.47	42	
T10	30	13.46	5-10	0.11	0.2	1.91	1.11	18.55	28	
T11	10	6.43	10-15	0.11	0.2	1.91	1.28	20.08	10	
T12	20	11.95	10-15	0.11	0.2	2.0	1.31	19.37	41	
T13	30	13.77	10-15	0.11	0.2	2.0	1.02	17.94	20	

GR: Granulated Rubber, GRr: Granulated Rubber Ratio, GRd: Granulated Rubber Dimension, ρ_s: particle density, Gs: specific gravity, D_r= Average initial relative density for the loose layer (*CPT Results), D_{50} =mean grain size of the particle, C_u=coefficient of uniformity and C_u=coefficient of curvature.

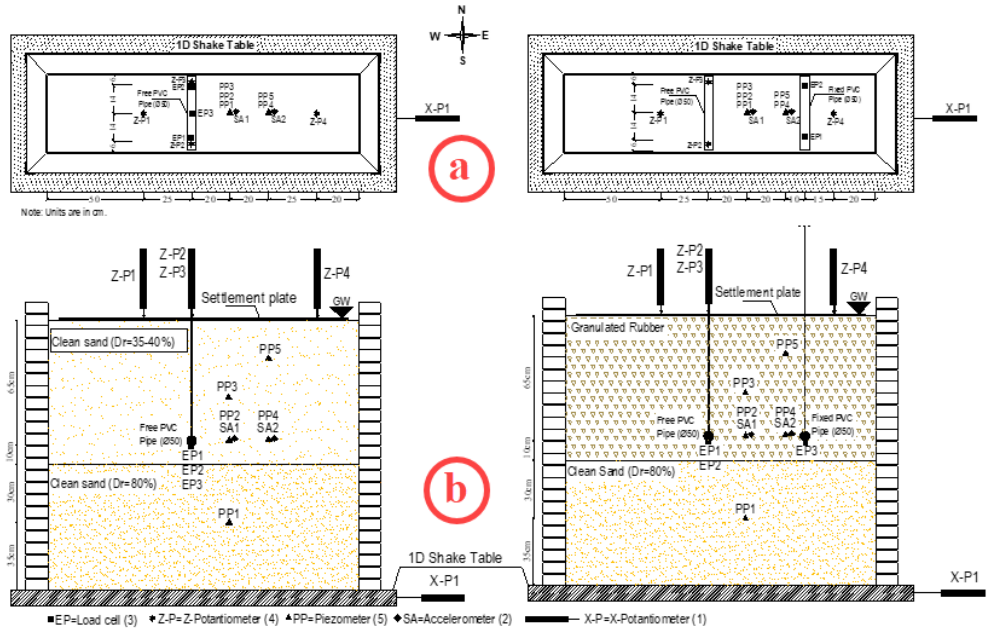

Figure 2.24. (a) plan view of setup (b) Configuration of model pipes and schematic illustration of the instrumentation (Source: Ecemis et al., 2021)

The effect of maximum acceleration on clean sand backfills and pipe response was examined by comparing the results of tests 1, 2, and 3. These tests applied three different maximum horizontal accelerations, a_{max} (0.2g, 0.35g, and 0.46g) with 2 Hz frequency. The applied accelerations were sinusoidal, unidirectional, with a constant frequency (Figure 2.25). The base shaking levels utilized in this study are given in Table 2.3, along with their equivalent maximum acceleration values $(a_{max})_{eq}$, as recommended by Seed and Idriss (1971).

Table 2.4. Summary of shaking table

Test #	Frequency (Hz)	Input max. Disp. (mm)	a_{max} (g)	$(a_{max})_{eq}$ (g)	Duration (sec)
T1	2	12.45	0.2	0.30	20
T2	2	22.54	0.35	0.54	20
T3	2	26.89	0.46	0.71	20
T4-13	2	22.54	0.35	0.54	20

Note: a_{max}= maximum acceleration

The change in EPWP ratio at 0.65 m and 0.4 m depth during the shaking Tests 1, 2, and 3 are given in Figure 2.26. The EPWP ratio is defined as $r_u=\Delta u/\sigma_{vo}'$ where Δu is the EPWP and σ_{vo}' is the initial effective vertical stress. Δu results with oscillation were observed for Test 3.

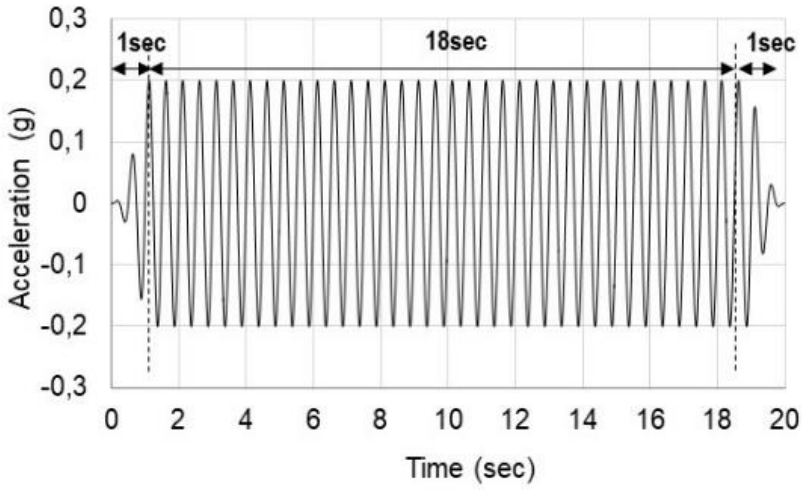

Figure 2.25. base excitation (a_{max}=0.2g)

(Source: Ecemis et al., 2021)

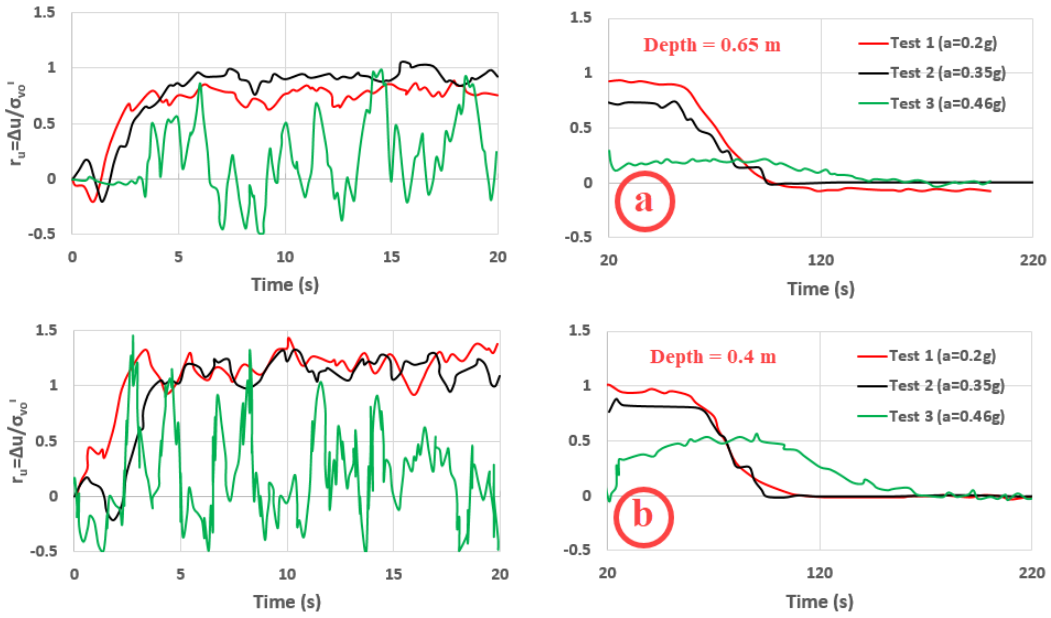

Figure 2.26. The Δu ratio of tests for a_{max} 0.2g (T1), 0.35g (T2), and 0.46g (T3) at depths (a) 0.65 m, (b) 0.4 m (Source: Ecemis et al., 2021)

Figure 2.28 shows the response of $r_u=\Delta u/\sigma_{vo}'$ in the clean sand deposit when there is no pipe (T4) and pipe buried inside the soil (T2). The ratio of r_u at 0.4 m and 0.65 m depths in the soil deposit with and without the pipe was near to unity, implying the occurrence of complete liquefaction. With the presence of a pipe in the earth, the generation and dissipation of pore pressure changed.

The generation of $r_u=\Delta u/\sigma_{vo}'$ at the pipe level (0.65 m depth) obtained from different ratios and sizes of the SGR mixture is shown in Figure 2.29a.

It can be seen that in the sample with clean sand, the r_u rises up to 1.0 at around 7.5 sec. Eventually, it approaches a more or less constant value. For other tests consisting of different amounts and sizes of GR in the sand, the Δu responded differently. The Δu in the sand-only backfill increased, showing liquefaction immediately with shaking initiation, while in the mixture, backfill increased gradually to a much lower extent. In the case of each GR dimension and ratio, no liquefaction occurred according to average r_u values. The result shows that the SGR mixture mitigated the liquefaction at the pipe level. The earth pressure increments (ΔP) at the bottom of the free pipe, during the shaking, are shown in Figure 2.29b. The results showed that the pressure increment was less than 10 kPa during shaking.

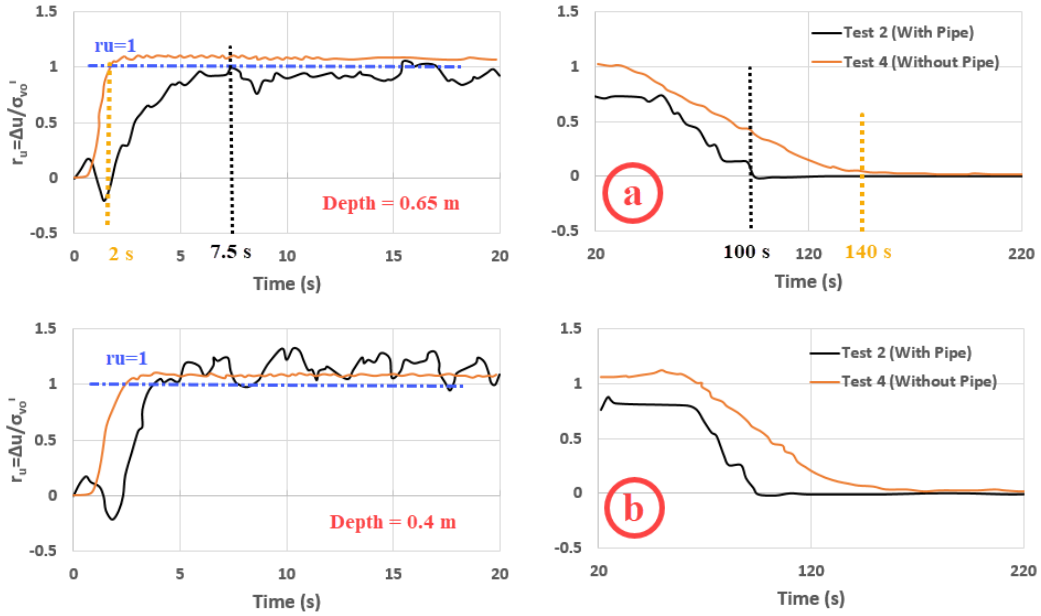

Figure 2.27. The r_u of sand deposit with no-pipe (T4) and pipe (T2) buried (a) 0.65 m (b) 0.4 m (Source: Ecemis et al., 2021)

The load transducers were measuring the total stress, which implied that the lateral earth pressure acting at the pipe increased following liquefaction. These findings show that the pressure increments are not only related to the Δu but also the settlement of the mixture and movement of the pipe.

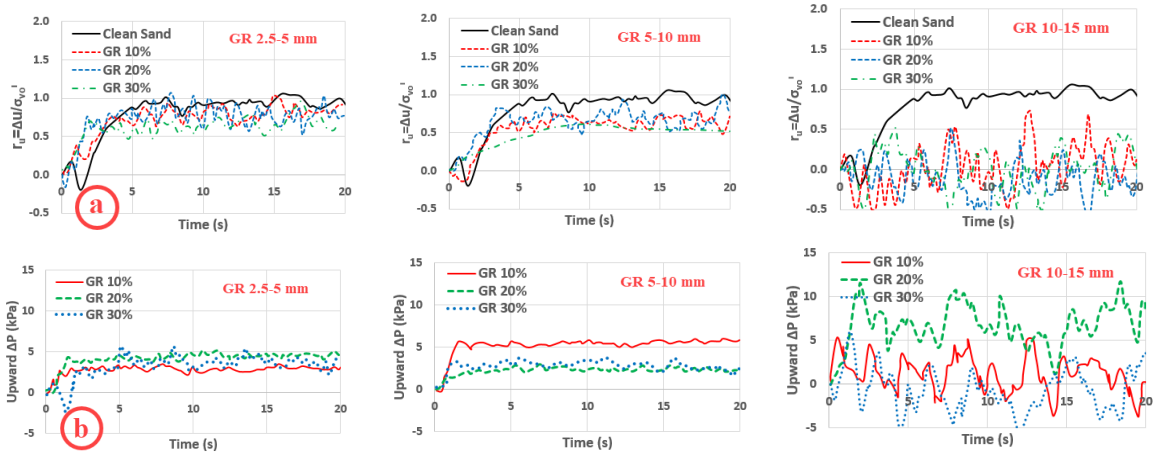

Figure 2.28. Time histories of (a) excess pore-water pressure ratio at the side of the pipe, (b) load increment at the bottom of the free pipe (Source: Ecemis et al., 2021)

The movement of the buried pipes and the SGR mixture settlement obtained from different GR dimensions and ratios are shown in Figure 2.30.

The pipe in the mixture backfills showed settlement and reasonable uplift during the shaking. Therefore, these cases were presented in three stages, and the illustration of these cases was given in Figure 2.31. In each test, the recorded settlement at the pipes was between 0 to 10 mm up to 3 sec shaking. Meanwhile, the maximum recorded settlement of the mixture surface was about 35 mm. This was represented as stage I. During stage I, the change in Δu was not big enough to uplift the pipe. (Stage I, 0-3 sec)

When the Δu reached a threshold value, pipe displacement changed, and uplift was seen for about 17 sec shaking (from 3 sec to 20 sec). This was represented as stage II (stage II, 3-20 sec). In each shaking test, the recorded uplift of the pipe was between 14 to 70 mm (Figure 2.30). At the same time, the reasonable settlement was recorded on the soil surface around 0 to 29 mm. At the end of the shaking, the pipe uplifting caused PWP dissipation, and the pipe settled for about 1 to 11 mm. At the same time, the maximum recorded settlement of the mixture was 10 mm. This was represented as stage III (stage III, 20-300 sec). The pipe settlement at stages I and III was due to the soil settlement. As shown in Figure 2.31, at stages I and III, the soil and pipe settled simultaneously. Although there was soil settlement in stage II, the pipe uplift was observed.

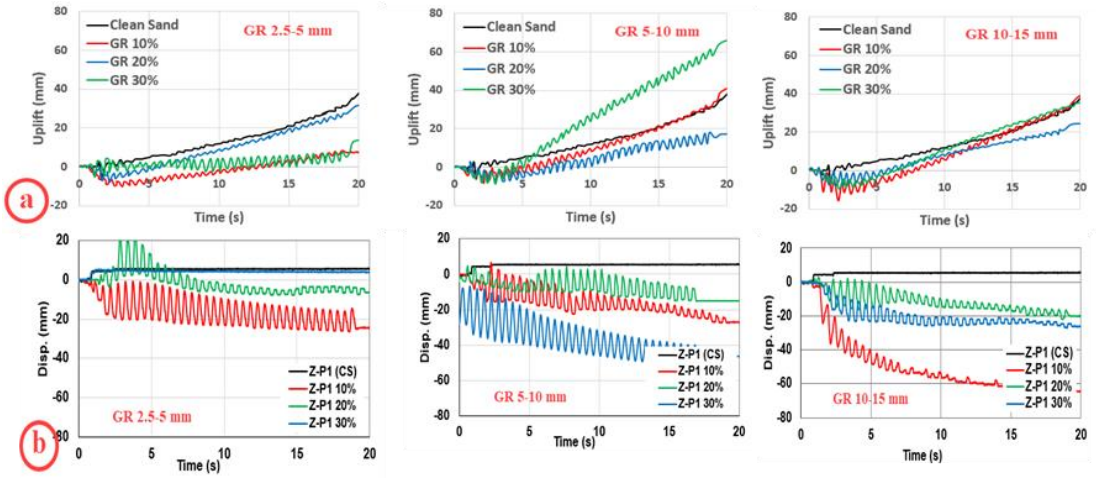

Figure 2.29. Time histories of; (a) pipe uplifting during the shaking, (b) the mixture settlement (Z-P1) (Source: Ecemis et al., 2021)

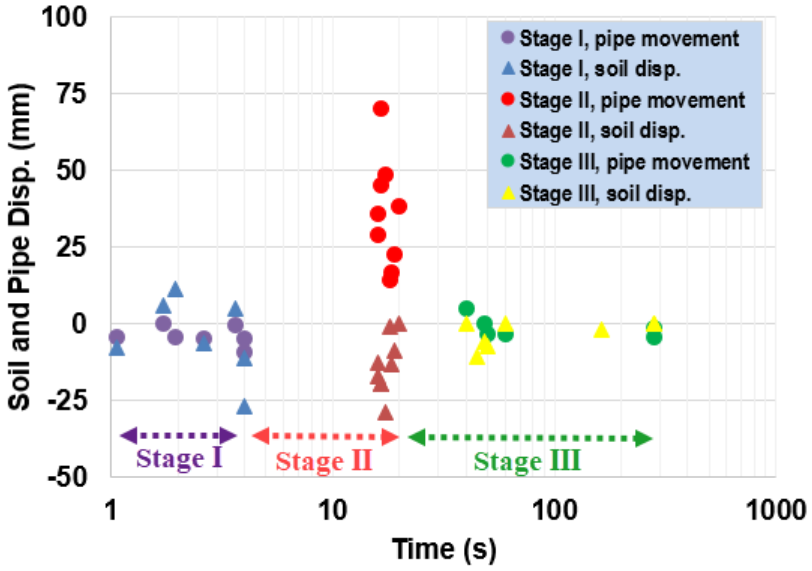

Figure 2.30. The pipe and soil movement at stages I, II, and III
(Source: Ecemis et al., 2021)

The results indicated that when the sand was shaken, the effective stress reduced as a result of the formation of considerable pore water pressure. However, the generation of Δu was decreased by increasing the volume of highly deformable GR in the clean sand. When the pipes were buried in the SGR mixture, the GR significantly reduced the amplitudes of the seismic waves, effectively isolating the pipe from the base seismic waves. Generally, the rise in the pore water pressure ratio reported in SGR mixtures is less than the increase recorded in clean sand. The results reveal that the pressure pressing on the pipes is directly related to the pore water pressure regardless of other variables. When the pipe was shaken in the ground with the SGR mixture used as backfill, the excess pore water pressure dissipated more quickly.

2.3. Theoretical Uplift Formulation

The uplift resistance in cohesionless soils is usually calculated using wedge uplift models where the resistance is divided into two contributions: the soil's weight above the pipe and the shear force acting on the slip surface along the soil wedge. The slip surface for the wedge assumed in the calculation model can either be vertical or inclined, as

shown in Figure 2.32. The inclined slip surface model has been experimentally shown to be closer to the real deformation mechanism by White et al. (2001). In this model, the inclination θ for the wedge is equal to the dilatancy angle (Eiksund 2014).

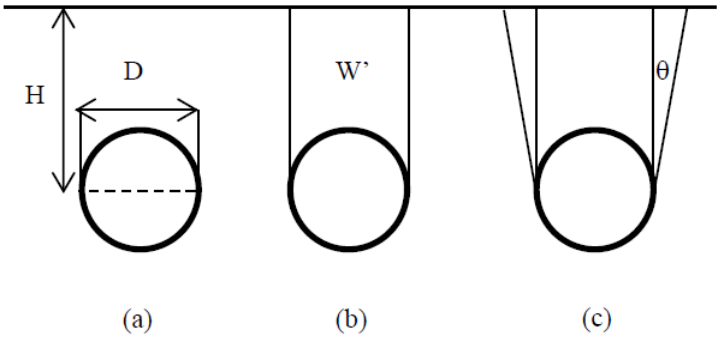

Figure 2.31. a) Embedment ratio definition H/D, b) Vertical wedge model, c) and inclined wedge model (Source: Eiksund 2014)

2.3.1. Load Mechanism of Buried Pipe in Static State

In a static state, a buoyant pipe is subjected to an uplift force due to the Archimedes Principle. The buoyant force can be estimated by subtracting the pipe weight (F_T) from the buoyancy force (F_B), as shown on the left-hand side of Equation 2.1. The overlying soil's weight (F_{WS}) and shear strength (F_{SP}) inhibit the floatation (Figure 2.33). This leads to the force equilibrium equation;

$$F_B - F_T \leq F_{WS} + F_{SP} \tag{2.1}$$

$$F_{resist} = F_{WS} + F_{SP} = \left[(\gamma'.D).\left(H - \frac{\pi.D}{8}\right)\right] + [f.(\gamma'.H^2)] \tag{2.2}$$

F_{ws}= overlying soil weight (Figure 2-30)

F_{SP}= soil's shear contribution

F_T= Structure weight

F_B= Buoyancy force

$\acute{\gamma}$= submerged unit weight of soil

D= Diameter of the structure

H= depth of the soil to the structure's axis

For loose sand, the code expresses the uplift resistance factor f as follows:

$$f = K_0 . \tan \varphi' = (1 - \sin \varphi') \tan \varphi' \quad (2.3)$$

Where K_0 is the coefficient of lateral earth pressure at rest, and φ' as the drained friction angle of the soil. For φ' = 25−40°, the range of f is less than 1.

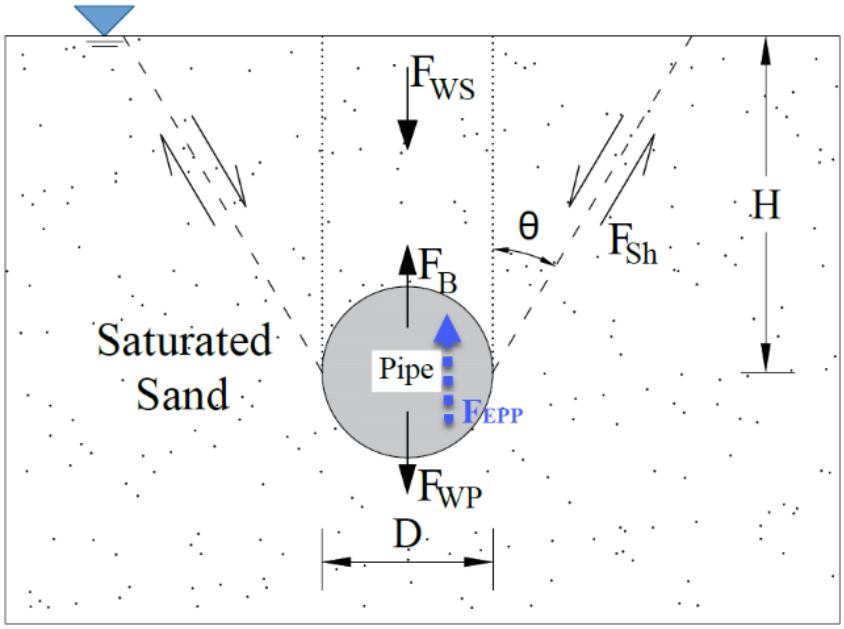

Figure 2.32. Force distribution acting on the pipe buried into saturated sand at vertical and inclined wedge model (Source: Chian and Madabhushi 2012)

2.3.2. Load Mechanism of Buoyant Buried Pipe in Liquefied Soil

In the event of soil liquefaction, the soil loses most of its shear strength, thereby reducing the contribution of the shear stresses along the two shear planes resisting the floatation.

$$F_B - F_T + F_{EPP} > F_{WS} + F_{Sh} \quad (2.4)$$

F_{EPP}= the force generated by the invert's increased pore pressure

2.3.3. Forces Influencing Floatation of Buried Pipe in Liquefied Soil

When liquefaction develops, the frictional contact between soil grains is lost, thereby reducing soil's shear strength.

$$F_{WS} = \left[\left(H.D - \frac{\pi.D^2}{8} + H^2.\tan\varphi'\right).\gamma'\right] \quad (2.5)$$

$$F_{SP} = (\tau_{ave}.2.L.\cos\varphi').(1 - r_u) \quad (2.6)$$

where *L* refers to the length of each shear plane (r_u=1 => F_{SP}=0).

$$F_{EPP} = F_{EPP\_Invert} = \int_{-D/2}^{D/2} P_{EPP\_Invert}\, dD \quad (2.7)$$

$$F_{EPP} = P_{EPP}.D \quad (2.8)$$

F_{EPP} is the uplift force at the bottom of the buried pipe caused by the EPWP; and $F_{EPP} = P_{EPP}.D$, in which P_{EPP} is the difference between the EPWPs at the bottom and the top of the pipe. Due to the simplicity of the equilibrium technique, it does not explicitly account for soil dilation reactions and seepage forces during and after soil liquefaction.

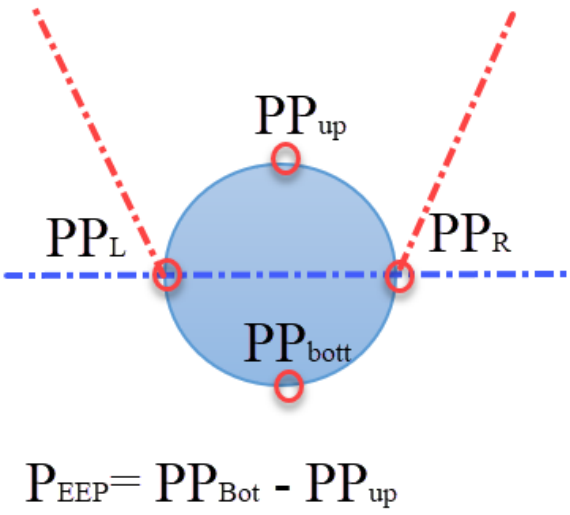

Figure 2.33. Force due to excess pore pressure generation
(Source: Ecemis et al., 2021)

2.3.4. Seepage Forces

Based on the soil deformation plots in Figure 2.35, it is evident that the soil deformation around the pipe formed wide circular loops on both sides, displacing from the crown to the invert of the structure. The overlying soil was pushed aside by the uplifting structure, whereas the region of the soil near the invert was drawn toward the expanding void beneath the structure. Given the lower excess pore water pressures at the invert of the structure compared with the far-field at the same depth, a hydraulic gradient exists, which induces movement of liquefied soil toward the invert of the structure because of a seepage force acting in the direction of the fluid flow. The values of F_{EPP} and F_{Seep} were evaluated by using the excess pore water pressure at the bottom of the structure and in the underlying soil layer. As a result, F_{Seep} value was usually zero or otherwise, less than 5% of F_{EPP} (Koseki et al. 1997).

$$F_{Seepage} \leq 5\% \, F_{EPP} \tag{2.9}$$

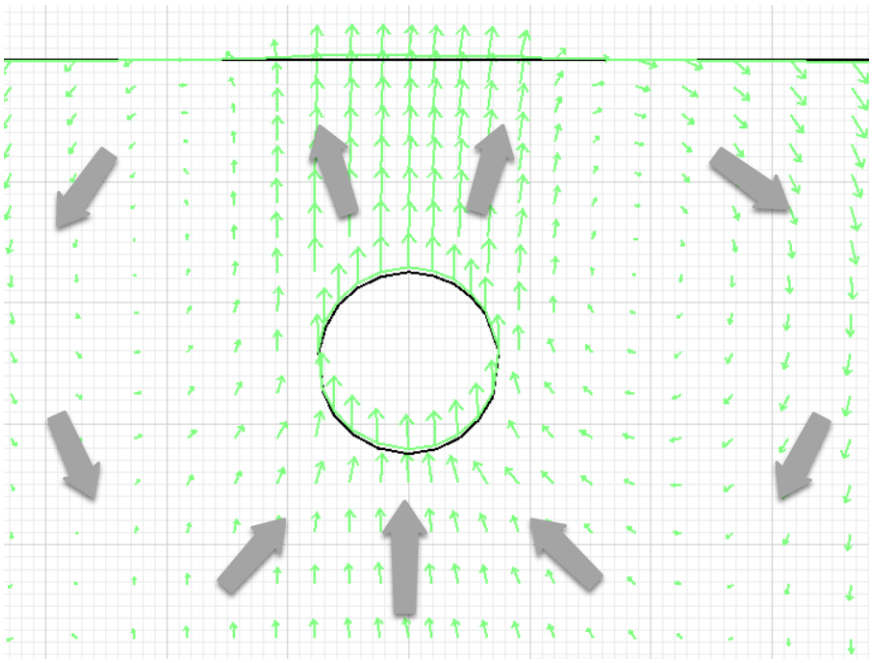

Figure 2.34. Final cumulative soil deformation and pipe displacement (Source: Ecemis et al., 2021)

where γ', D, H, and ϕ' are the submerged soil's unit weight, the diameter of the pipe, the pipe burial depth, and the drained friction angle, respectively. L refers to the length of each shear plane, and pore pressure ratio (r_u) equal to 1 results in F_{SP} to 0. The factor of safety (FoS) of the buried pipe base on inclined slip surface model can be found by the following equation:

$$FoS = \frac{F_{WS}+F_{Sh}}{F_B - F_{WP}+F_{EPP}} \tag{2.10}$$

2.4. Summary

Some laboratory and numerical studies about the buried pipe uplift in the liquefied soil were reviewed in the previous sections. The conducted studies in this area were mostly experimental. Numerical researches had a low portion in the conducted studies in this area. Also, to study the liquefaction phenomena, advanced constitutive models had to use so that the obtained results get close to the sand behavior in reality. Numerical

studies have been performed to investigate the diameter of the pipe and the buried depth effect by using old models. Most of these constitutive models cannot predict the dilation behavior and saturated sand contraction during an earthquake, which causes the EPWP generation correct simulation's inability. Therefore, this study uses sufficient software (FLAC) and advanced soil constitutive model (UBCSAND) to investigate the effect of EPWP generation, buried pipe diameter, and burial depth variables on the uplift behavior of buried pipes in liquefied soil.

CHAPTER 3

NUMERICAL STUDY

3.1. Introduction

One of the significant challenges of soil mechanics is developing a novel and advanced constitutive model to accurately model the soil's nonlinear behavior that is a time-dependent event. The soil has a multi-phase medium which fluid flow is a challenging issue. FLAC (Fast Lagrangian Analysis of Continua) is a finite difference (FD) software presented by Itasca consulting engineers (Itasca, 2011). The complex and challenging issues related to soil structures can be investigated using numerical studies in this software. It is an incredibly difficult process to simulate liquefaction numerically since it is a highly nonlinear problem with many variables (Topalidisz, 2018).

FLAC can simulate liquefaction by coupling the differential equations of the solid and fluid phases. FLAC can perform coupled effective stress models (Itasca, 2011). Explicit solution methods and finite different element formulation are two significant aspects of FLAC in comparison with other analysis methods. Recently, FLAC was used to observe the seismic behavior of buried structures in liquefiable and non-liquefiable soils. The UBCSAND advanced soil constitutive model has also been used to simulate the liquefaction phenomenon in this work. This model can be used to simulate changes in pore water pressure and soil stiffness as a result of monotonic and cyclic stress.

3.2. FLAC2D

FLAC software uses the Finite Difference Method (FDM) for engineering calculations. This program has been utilized to model the structural behavior of soil, rock, or other materials that may plasticize after yielding. It is basically designed for geotechnical and mining engineering. However, due to its wide range of capabilities, this program can solve complex mechanical problems in other engineering fields. The various constitutive models introduced in this program help engineers model and analyze different non-linear events.

FLAC is one of the products of Itasca Consulting Group, Inc. The company was founded in 1981 by the faculty members of the civil and mining engineering department at the Minnesota University established to provide soil and rock mechanical services, numerical modeling of geotechnical environments, and underground spaces. In 1986, the first version of FLAC2D software was introduced to the scientific community worldwide by Dr. Peter Cundall's support. During the development of the new and 3D versions of this software, other software, including PFC2D, PFC3D, 3DEC, for specific geotechnical modeling was revealed by Itasca.

Among the capabilities of FLAC, the following can be mentioned:

- The ability to model interface elements through slipped planes, faults, soil layers, and interactions was simulated.
- Analytical modes of plane strain, plane stress and axial symmetry.
- The ability to model groundwater flow and soil consolidation.
- The ability to model structural elements to simulate tunnels, nailing systems, rock bolts, piles, etc.
- The ability of geotechnical problems dynamic analyses to apply harmonic loads, earthquake loads, and explosion.
- Ability to model viscoelastic and viscoplastic (creep).
- Ability of thermal and heat changes modeling and mechanical stresses and pore water pressure (PWP).
- Ability to model two phase flow to simulate this flow in porous media.
- Ability to add models that are written by the C++ programming.

The FLAC has a powerful programing language called FISH (FLACish). Using this programing language, the user can model the desired functions in the software or introduce the advanced constitutive models to the environment. The FISH programming also allows the user to perform parametric and staged studies quickly. This programing will make FLAC more flexible to the user in unforeseen issues and parametric studies. For example, a new variable can be introduced, new nodes can be applied to the model (Itasca2011).

3.2.1. Explicit Dynamic Solution Scheme

FLAC is known as the Explicit Finite Difference Method (FDM) software, which acts based on the Lagrange analysis. The FDM is almost the oldest numerical analysis method that operates based on differential equations in which the initial and boundary conditions are introduced into the model. In the FDM, each derivative of equations is directly defined by an algebraic description in terms of model variables. These variables are not defined into the model elements. On the contrary, in the Finite Element Method (FEM), the main focus is on changing the values of the model quantities (such as stress and displacement) using functions in each of the elements defined based on the model parameters. The formulation is based on calculating the values related to the parameters to minimize the calculation or energy error. Both of these methods obtain a set of algebraic relations to solve the model. Although these equations are gained in different ways, the results obtained by the calculations of specific models will be similar to each other.

FLAC uses an explicit time-domain method to solve algebraic equations, while in Finite Element (FE) analyses, the implicit methods based on the matrix analysis are more common. Figure 3.1 shows the common computation cycle in FLAC software. In this method, the motion equations are initially used to extract new velocities and displacements due to the stresses and forces applications. Then the strain values are calculated from the velocity value and the new stress value obtained from the new strain.

Each of these computational cycles occurs in a time increment. In each operator shown in Figure 3.1, all variables related to the zones are updated than the previous step.

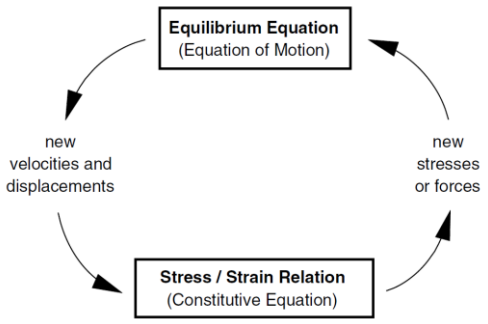

Figure 3.1. Explicit calculation cycle

(Source: Itasca 2011)

In the following, explicit and implicit methods are compared. As can be seen, the main disadvantage of the explicit FDM is little time increments. This will lead to a large number of computational steps in model analysis. The FDM is the best analysis method for complicated simulations such as nonlinear models, large strain, and physical instability (Itasca2011), Table 3.1.

Table 3.1. Comparison of explicit and implicit solution methods
(Source: Itasca, 2011)

Explicit	Implicit
Timestep must be smaller than a critical value for stability.	Timestep can be arbitrarily large, with unconditionally stable schemes.
Small amount of computational effort per timestep.	Large amount of computational effort per timestep.
No significant numerical damping introduced for dynamic solution.	Numerical damping dependent on timestep present with unconditionally stable schemes.
No iterations necessary to follow nonlinear constitutive law.	Iterative procedure necessary to follow nonlinear constitutive law.
Provided that the timestep criterion is always satisfied, nonlinear laws are always followed in a valid physical way.	Always necessary to demonstrate that the above-mentioned procedure is (a) stable, and (b) follows the physically correct path (for path-sensitive problems).
Matrices are never formed. Memory requirements are always at a minimum. No bandwidth limitations.	Stiffness matrices must be stored. Must find ways to overcome associated problems such as bandwidth. Memory requirements tend to be large.
Since matrices are never formed, large displacements and strains are accommodated without additional computing effort.	Additional computing effort needed to follow large displacements and strains.

3.2.2. Finite Difference Equations

The finite difference (FD) equations for a triangular sub-zone are obtained using Gaussian divergence theory in the form of Equation 3.1:

$$\int_s n_i f ds = \int_s \frac{\partial f}{\partial x_i} dA \tag{3.1}$$

Where;

$\int_s$ is the integral around the boundary of a closed surface;

n_i is the unit normal to the surface, s;

f is a scalar, vector or tensor;

xi are position vectors;

ds is an incremental arc length; and

$\int_A$ is the integral over the surface area, *A*.

Variation average values of f in A area is defined as:

$$< \frac{\partial f}{\partial x_i} >= \frac{1}{A} \int_A \frac{\partial f}{\partial x_i} dA \tag{3.2}$$

By using Equation 3.1, Equation 3.2 can be written as:

$$< \frac{\partial f}{\partial x_i} >= \frac{1}{A} \int_A n_i f ds \tag{3.3}$$

For a triangular sub-element, Equation 3.3 is defined as:

$$< \frac{\partial f}{\partial x_i} >= \frac{1}{A} \sum_s < f > n_i \Delta s \tag{3.4}$$

In which Δs is the one side length of triangular and the simulation is conducted on all three sides of the triangle. The <f> value is calculated regarding the longitudinal average of the element's three aspects. Strain rate $\dot{e}_{ij}$ by writing node velocity for a zone and replacing it with the average velocity vector in each side of the element for f variable based on Equation 3.4 is calculated as Equations 3.5 and 3.6.

$$\frac{\partial \dot{u}_i}{\partial x_j} = \frac{1}{2A} \sum_s (\dot{u}_i^{(a)} + \dot{u}_i^{(b)}) n_i \Delta s \tag{3.5}$$

$$\dot{e}_{ij} = \frac{1}{2} \left\{ \frac{\partial \dot{u}_i}{\partial x_j} + \frac{\partial \dot{u}_j}{\partial x_i} \right\} \tag{3.6}$$

In these Equations, (a), (b) are two consecutive nodes on a triangular boundary. It should be noted when the velocity between nodes changes linearly, by averaging Equation 3.5, the same results are obtained, like integrating.

By using Equations 3.5 and 3.6, all components of the strain tensor can be extracted. The maximum shear strain is the best variable to get the results output. This value means the second strain constant in the components on the x-y plane. This value can be extracted using the Mohr cycle of strain according to Figure 3.2.

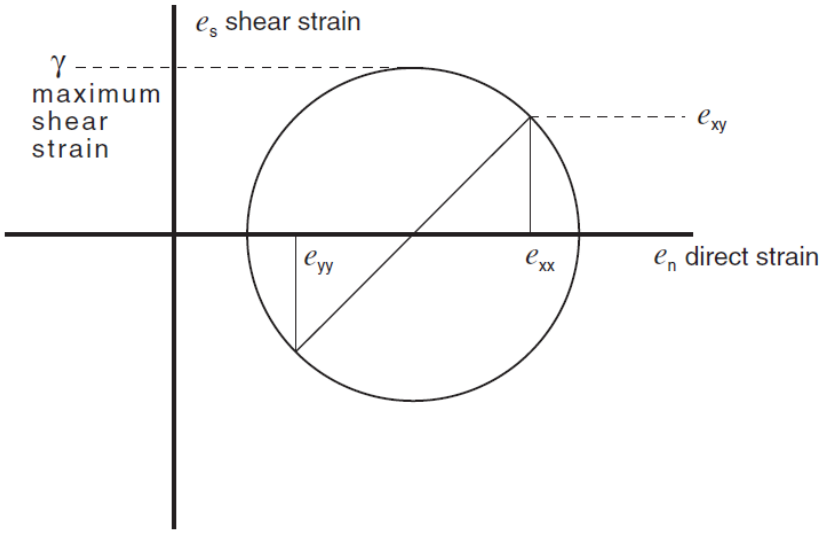

Figure 3.2. Mohr's circle of strain

(Source: Itasca 2011)

considering Figure 3.2, the maximum shear strain will be equal to:

$$\gamma = \frac{1}{2}\left(\left(e_{xx} - e_{yy}\right)^2 + 4e_{xx}^2\right)^{1/2} \tag{3.7}$$

3.3. Numerical Modeling

Numerical modeling is performed in two steps: static and dynamic.

3.3.1. Static Stage

- Create a finite-difference network.
- Applying the constitutive models and properties of materials.
- Boundary and initial conditions application.
- Establishing the initial equilibrium conditions in the model.
- Performing the program till the initial balance is reached.

By assigning a grid, the geometry of the model can be introduced to the software. The constitutive models and materials properties introduced to the model determine how the model performs under deformations. Finally, the initial and boundary conditions defined the simulated environment state. After applying these specifications, the model is analyzed to reach the initial equilibrium state.

3.3.1.1. Model Geometry and Zones

In the zoning process, the number of zones should be selected efficiently. Although the larger number and smaller zones in a model result in exact outcomes, the run time increases with a large number of the zones. Therefore, according to the model, the zone dimensions should be selected to achieve high accuracy and the proper run time.

In dynamic analysis, wave propagation in the soil media may generate numerical confusion because of modeling unwanted conditions. The frequency content of the input wave and the wave velocity affect the numerical accuracy of wave transmission. In order to wave transfer accuracy in a continuum soil medium, the recommended condition by (Kuhlemeyer and Lysmer, 1973) have to satisfy. These researchers suggested that the zone sizes in the continuum media should be smaller than the values of the following Equation:

$$\Delta l \leq \frac{\lambda}{10} \tag{3.8}$$

In this Equation, Δl is the size of the largest zone, and λ is wavelength in the highest frequency in the model. On the other hand, if the C is the velocity of P or S wave in the environment and T is the wave period, so λ equals to:

$$\lambda = CT \tag{3.9}$$

By the “grid” command, the total row numbers are specified in the zoning network. By the “Generate” command, the zoning network can be geometrically shaped. In this study, smaller zones around the buried pipe have been used to increase the accuracy and control the run time (Figure 3.3).

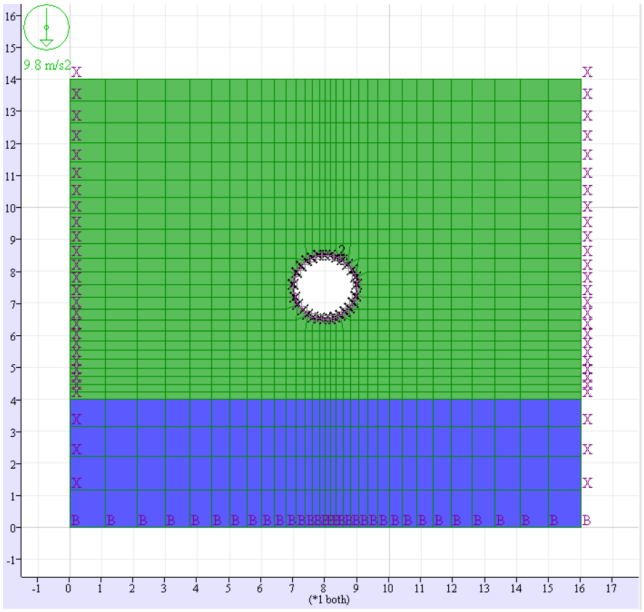

Figure 3.3. Model zoning pattern

3.3.1.2. Constitutive Models in FLAC

The types of elastic constitutive and some plastic constitutive models predefined in FLAC software are as follows:

- Elastic Isotropic Model
- Elastic Transversely model
- Mohr-Coulomb Model
- Drucker – Prager Model
- Strain – Hardening/Softening Model

- Modified Cam – Clay Model

In the static analysis stage, the Mohr-coulomb model has been used. This model is more suitable for modeling due to its elastoplastic behaviors.

3.3.1.3. Mohr-Coulomb Model

This model is the most common model for modeling soil-rock environment, which properly introduces the shear failure behavior in soil. In Figure 3.4, the general form of the Mohr-coulomb failure criterion is observed. As seen, the failure occurs in A to B path.

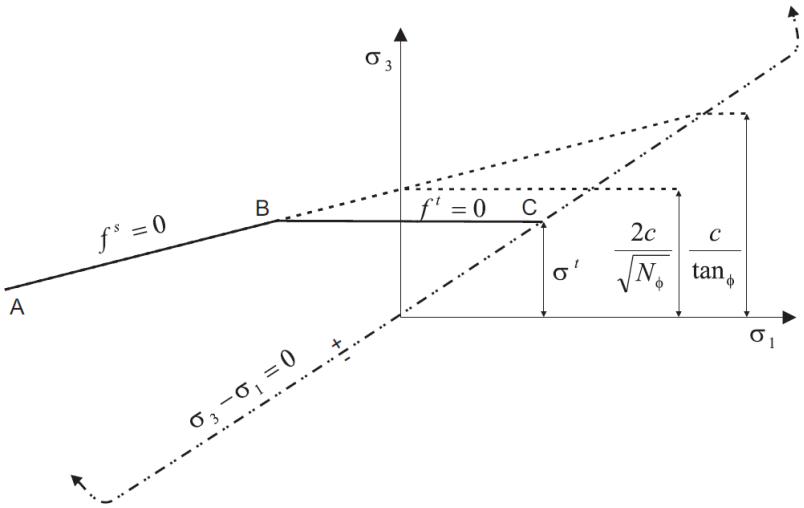

Figure 3.4. Mohr-Coulomb failure criterion in FLAC
(Source: Itasca 2011)

In Equation 3.10, the path is introduced using the flow function of Mohr-coulomb.

$$f^s = \sigma_1 - \sigma_3 N_\phi + 2c\sqrt{N_\phi} \tag{3.10}$$

Tensile flow also occurs in path B to C using the function 3.11.

$$f^s = \sigma^t - \sigma_3 \tag{3.11}$$

In these Equations, ϕ is internal friction angle, C is cohesion, σ_t tensile strength, and N_ϕ value is obtained by Equation 3.12.

$$N_\phi = \frac{1+\sin\phi}{1-\sin\phi} \tag{3.12}$$

In the shear flow formulation, only the minimum and maximum principal stresses are used, and the mean principal stress will have no effect on the formation. The shear potential function of materials is introduced in Equation 3.13.

$$g^s = \sigma_1 - \sigma_3 N_\psi \tag{3.13}$$

In this Equation N_ψ is introduced as Equation 3.14, which ψ is the dilation angle.

$$N_\psi = \frac{1+\sin\psi}{1-\sin\psi} \tag{3.14}$$

This model by using the “model Mohr-coul” Command or “m m” allocated to the selected zones.

3.3.1.4. Boundary Conditions and the Initial Equilibrium

Boundary conditions in numerical modeling include field variables such as stress and displacement. Boundary conditions are divided into two categories real and artificial. The real boundary exists practically like the edge of the shaking table. There is no artificial boundary in reality, but it is necessary to constrain the zones in infinite.

In static analysis, the model boundaries are fixed using the “Fix” command. In this way, the characteristic of the supports located at the boundaries of the real model is simulated acceptably. The model must reach initial equilibrium before applying dynamic loading. In complex modeling with various materials, the initial equilibrium in the model must be done to reach its stability.

There are two limit methods for the user to realize the balance of the model:

1. Study of the node force, which is called the maximum unbalanced force.
2. Study the maximum ratio between the unbalanced force and the average force applied in the node points is called the equilibrium ratio.

Theoretically, the model reaches equilibrium when in each node the resultant force reaches zero. As seen in Figure 3.5, on the horizontal axis that shows the analysis increments, the unbalanced force on the vertical axis reaches zero after some increments.

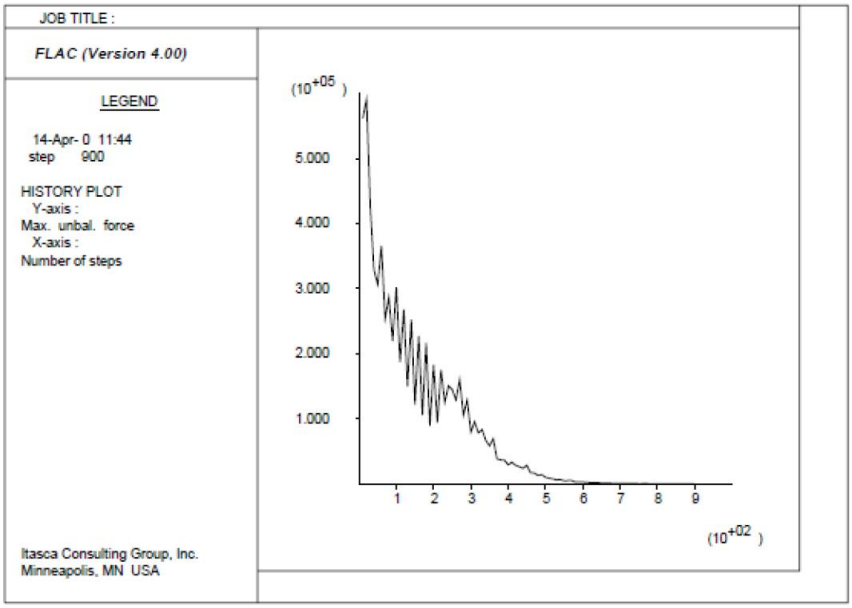

Figure 3.5. Maximum unbalanced force History
(Source: Itasca 2011)

3.3.2. Dynamic Analysis

FLAC software allows the user to perform dynamic analysis on the 2D plane strain and axisymmetric models. Dynamic analysis can also be performed on the models consisting of structured elements. Therefore, the user can investigate the soil-structure interaction in the models. Dynamic analysis can be used to model the earthquake occurrence, vibrating foundations, explosion, etc.

3.3.2.1. Dynamic Analysis Methods

The two common methods in the dynamic analysis are the Equivalent-Linear method and the Fully Non-Linear method.

The equivalent-linear method is suitable for studying earthquake excitation, wave propagation in soil strata, and soil-structure dynamic interaction. In this method introduced by Seed and Idriss 1969, linear analysis is performed by assigning initial values to the damping ratio and shear modulus in different areas of the model. The maximum cyclic shear strain is recorded for each element and used to determine new values for damping and modulus by reference to laboratory-derived curves that relate damping ratio and secant modulus to the amplitude of cycling shear strain. The new values of damping ratio and shear modulus are used in a new numerical analysis of the model. This process continues till the obtained values from numerical analysis and laboratory tests reach compatibility. In the fully nonlinear method, the modeling analysis process is performed in only one step in a way that proper nonlinear Equations are used. Each method has its strengths and weaknesses. The linear equivalent method is easier and uses the laboratory results directly. On the other hand, the nonlinear method has modeled the system's overall physics carefully. It is more complex than the linear equivalent method, and the user requires deep dynamic knowledge.

3.3.2.2. Characteristics of the Equivalent-Linear Method

- In this method, specific linear properties are considered for each element, which remains constant during vibration and is estimated by the mean dynamic motion. During the quiet periods, the elements' behavior is smooth and stays in an overdamped state, while during the intense vibrations, the elements' behave stiff and underdamped.
- In this method, interference and mixing phenomena that occur between components with different frequencies in nonlinear material are ignored.
- The information about irreversible displacements and changes cannot be extracted because only oscillatory vibrations are modeled in this method. However, permanent effects can also be modeled using empirical relationships.

- The elastic theory is used in the equivalent linear method, so the relation between strain and stress tensors is not based on the incremental relations of strain tensors in the plasticity theory.
- When compressive and shear waves flow in the model, the linear equivalent method independently considers these two types of waves. Consequently, the software does not calculate the interaction of these two waves.

3.3.2.3. Characteristics of the Fully Nonlinear Method

- Using the nonlinear method, interference and mixing of different frequency are simulated naturally in the model.
- Irreversible displacements and other permanent changes in the model are automatically applied.
- In this method, the increase of the plastic strain can be modeled regarding the plasticity theory in the program.
- The effect of other alternative models on the simulated model can be easily studied.
- Both shear and compressional waves are propagated together in a single simulation, and the material responds to the combined effect of both components. In intense vibrations, the shear and compressive waves coupling effect can be very important.

3.3.2.4. Dynamic Formulation

The finite-difference formulation in dynamic modeling in FLAC is the same as the classical finite difference formulations. The stiffness of the studied zones can be calculated according to Equation 3.15.

$$k_z = \left(K + \frac{4}{3}G\right)\frac{L_d^2}{A_z}T \tag{3.15}$$

where A_z is the area of the rectangular zone, K is the Bulk modulus, G is the shear modulus, and L_d is the length of its diagonal.

The model thickness for the plane strain condition is considered equal to 1.0. Equation 3.16 is also used to calculate the time increments of the solution.

$$\Delta t_{inc} = min\left\{\frac{A}{C_p \Delta x_{max}}\right\} \tag{3.16}$$

In this Equation, C_p is the compressive wave velocity, and A is the area of the triangle's subzone. Δx_{max} is the maximum length of the studied zone. When there is no damping, the safety factor of 0.5 is also used to estimate the critical time interval. Therefore, in this case, Equation 3.17 is proposed to calculate the time steps of the solution.

$$\Delta t_d = \frac{\Delta t_{inc}}{2} \tag{3.17}$$

If damping is also used in the equations, the time interval steps are reduced, and according to (Belytschko, 1983) the value will be equal to:

$$\Delta t_\beta = \left\{\frac{2}{\omega_{max}}\right\}\left(\sqrt{1+\lambda^2} - \lambda\right) \tag{3.18}$$

The angular velocity in Equation 3.18 was due to the system's highest vibrational frequency, and Lamda is a fraction of critical damping. By Equations 3.19 and 3.20, the values of these two parameters can be estimated.

$$\omega_{max} = \frac{2}{\Delta t_d} \tag{3.19}$$

$$\lambda = \frac{0.4\,\beta}{\Delta t_d} \tag{3.20}$$

$$\beta = \frac{\xi_{min}}{\omega_{min}} \tag{3.21}$$

ξ_{min} damping ratio and ω_{min} is an angular frequency for Rayleigh damping mode.

3.3.2.5. Dynamic Loading

In the FLAC modeling, dynamic loading can be applied in two ways: The first method applies dynamic loading to the model boundaries and the second method applies loading to internal nodes. The adverse effect of wave reflection can be partially eliminated by the use of dampers in the boundaries. In FLAC, dynamic loading input is applied to the model in four ways:

(a) acceleration history;

(b) velocity history;

(c) stress (or pressure) history; or

(d) force history.

Dynamic input is applied to boundaries using the "Apply" command, and to present inputs to internal nodes, the "Interior" Command is used.

3.3.2.6. Boundary Condition in Dynamic Problems

In dynamic analysis, fixed boundaries reflect the vibrational waves, and the energy dissipation does not occur as in the real state. However, the environment is unlimited in nature, and the wave propagates in semi-infinite media. So, the fixed boundaries must be modified in dynamic analysis so that the waves should not be reflected in the environment and the analysis is not encountered errors. In FLAC software, two boundary conditions are introduced, which are discussed in the following.

3.3.2.7. Quiet Boundary Condition

The quiet and energy-absorbing boundaries are applied to the model to prevent wave reflections. In order to do this, independent dampers are used in vertical and shear directions. While using the quiet boundaries, the static loading situations should be concerned significantly. Before dynamic analysis starts, the model should reach static stability. Quiet boundaries can be applied in the X and Y directions. Also, vertical and tangential quiet boundaries can be used for inclined edges. Quiet boundaries for the model

base are necessary if the loading type is stress or force history. For acceleration or velocity histories, the model base has to be fixed.

When the dynamic energy source is located inside the model, the quiet boundaries are used in lateral boundaries. When the dynamic energy source is applied in the lower or upper part of the model, lateral boundaries should not be damped by using the quiet boundaries, and this is because the wave's energy leaks from the sides and is wasted. In this case, the free field boundaries must be used for the lateral boundaries.

3.3.2.8. Free-Field Boundary Condition

In high damping soils, boundary conditions can be installed at short distances from each other. However, the large distance between boundary conditions will increase the model operation volume if the damping is low. The practical way is to define the free field boundaries for lateral boundaries to minimize the wave reflection. As seen in Figure 3.6, viscous dashpots are used to simulate free field boundaries on the side of the model.

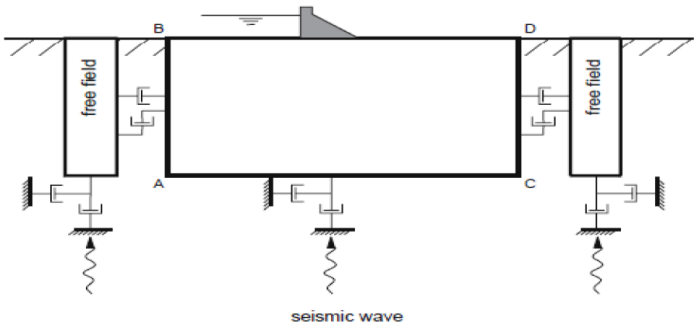

Figure 3.6. Model for seismic analysis of surface structures and free-field mesh (Source: Itasca 2011)

Applying the free field boundaries in the lateral parts, the wave reflection phenomena will not be created during the analysis, and the model sides behave as semi-infinite media.

3.3.2.9. Constitutive Models in Dynamic Analyses

There are various models for evaluating the liquefaction potential and possibility. Some models are given below:

- ROTH Model
- WANG Model
- FINN Model
- UBCSAND Model

The Roth model examines liquefaction by relying on effective stresses but uses weak coupling relations. In this model, the interaction of solid and liquid phases is not fully considered. Therefore, this model can not predict the sediments caused by soil liquefaction. The Wang model uses a plastic constitutive model which considers the liquefaction mechanism properly. Its disadvantages are the high complexity and a large number of variables. The Finn model obtains the PWP directly and has a small number of variables. The UBCSAND model examines the liquefaction phenomena by relying on the effective stresses, which use a strong coupling method.

3.3.2.10. UBCSAND Soil Constitutive Model

UBCSAND is an effective stress plasticity model that was developed to perform simulations for liquefied soils under dynamic loading (Beaty and Byrne, 2011). The UBCSAND model can simulate pore water pressure and changes in soil stiffness due to monotonic and cyclic loading. Notably, this fully-coupled plasticity model uses the flow rule as it makes a link between plastic volumetric strains and plastic shear strains. This essential ability to represent the progress of contractive and dilative responses allows the UBCSAND model to simulate sand-like soil behavior reasonably (Beaty, 2018). The UBCSAND model has been calibrated to replicate the Youd et al. (2001) liquefaction screening chart, which was developed using field observations from previous earthquakes and is stated in terms of standard penetration test resistance, $(N1)_{60}$. The model characteristics are presented in terms of $(N1)_{60}$, which are calculated using an approximate conversion method, such as that proposed by Skempton (1986), from the known relative density, D_r.

Elastic Response:

The elastic behavior is expressed in terms of shear modulus (G^e) and bulk modulus (B^e) which are stress-level dependent (Beaty and Byrne, 2011);

$$B^e = K_B^e \times P_a \times \left(\frac{\sigma'_m}{P_a}\right)^{me} \approx \frac{2(1+\mu)}{3(1-2\mu)} G^e \tag{3.22}$$

$$G^e = K_G^e \times P_a \times \left(\frac{\sigma'_m}{P_a}\right)^{ne} \tag{3.23}$$

Where K_B^e and K_G^e are modulus numbers, P_a is the atmospheric pressure and σ_m' is the initial mean effective stress. Shear modulus number $K_G^e$is typically between 500 and 2000, n_e is the stress exponent for *Ge* (typically between 0.4 and 0.6, or approximately 0.5), K_B^e is the bulk modulus number, m_e is the stress exponent for B^e, and μ is the Poisson's ratio (0.0 to 0.2 for small strain elastic response of sand) (Beaty, 2018).

Plastic Response:

Plastic shear strain estimates during loading are dependent on ϕ_{mob}, ϕ_{cv}, the total strain increments $\Delta\varepsilon_v$ and $\Delta\gamma$, and the flow rule. the prior maximum stress ratio η defines ϕ_{mob} during the running half-cycle of loading, where $\phi_{mob} = \arcsin(\eta_{max})$, and $\eta = \tau/\sigma'_m$ in the plane of loading (τ and σ'_m are the principal shear stress and mean effective stress, respectively). ϕ_{mob} denotes the yield surface and is shown in stress space as a radial line from the origin, as illustrated in Figure 3.7 (Beaty, 2018).

Each solution step begins with the evaluation of a strain increase, assuming an elastic response. If the resulting stress state produces a stress state that lies above ϕ_{mob}, the strain increment is recalculated to account for both elastic and plastic responses. By satisfying the hardening relationship, the flow rule, and the linear elasticity equations connecting effective stress and elastic strain increments, this re-evaluation divides the total strain increments into elastic and plastic components. (Beaty, 2018).

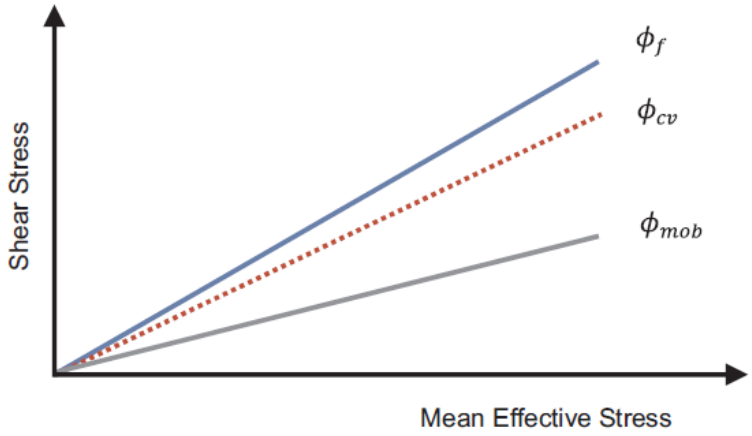

Figure 3.7. UBCSAND yield surface

(Source: Beaty, 2018)

Through the hardening connection indicated in Equation 3.24 and illustrated in Figure 3.8, the plastic shear strain increment $\Delta\gamma^p$ is connected to the change in shear stress ratio $\Delta\eta$.

$$\Delta\gamma^P = \frac{1}{G^P/\sigma'_m}\Delta\eta \tag{3.24}$$

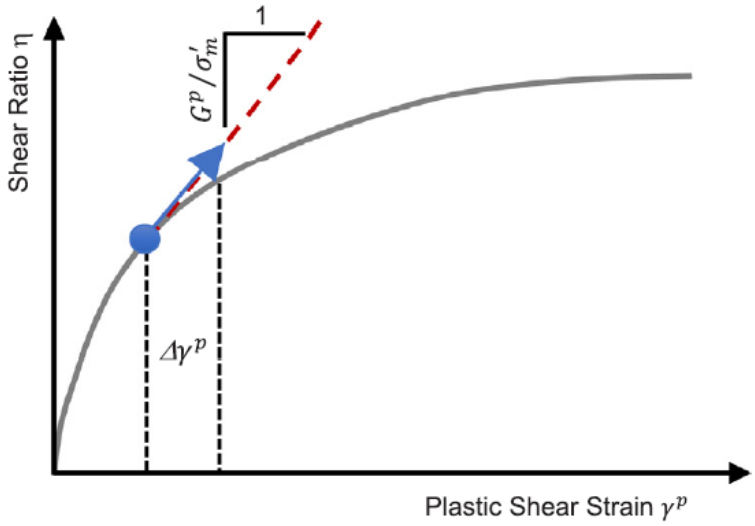

Figure 3.8. Hardening relationship for UBCSAND

(Source: Beaty, 2018)

G^p denotes the plastic shear modulus. Assuming that η and γ^p have a hyperbolic relationship, the plastic shear modulus is given by Equation 3.25:

$$G^p = G_i^P \left(1 - \frac{\eta}{\eta_f} R_f\right)^2 \tag{3.25}$$

where G_i^p is the plastic shear modulus at η = 0 and is also a function of σ'_m, η_f is the stress ratio at failure and equal to sin(ϕ_f), ϕ_f is the peak friction angle in undrained loading, and R_f is the failure ratio for the hyperbolic relationship. R_f ranges typically between 0.6 and 1 and falls as relative density increases (Beaty, 2018).

Equation 3.26 calculates the flow rule relating $\Delta\gamma^p$ to $d\varepsilon_v^p$. This flow rule may be deduced from energy considerations and is analogous to the idea of stress dilation (Beaty, 2018). This rule encompasses two distinct behaviors: 1) the soil contracts under the ϕ_{cv} line and dilates above it, and 2) the rate of contraction or dilatation rises as the difference between the yield surface and the ϕ_{cv} line grows (Beaty, 2018).

$$\Delta\varepsilon_v^P = (\sin\phi_{cv} - \sin\phi_{mob})\Delta\gamma^P \tag{3.26}$$

Upon unloading, defined as a decrease in the magnitude of η, it is anticipated that the sand will behave elastically until a shear stress reversal is recorded. Additional details on these points are given in (Beaty and Byrne, 2012).

UBCSAND (v.904aR) has a number of restrictions due to the relative simplicity of its structure. These restrictions must be weighed in light of any use of the model. The direction of principal stress may rotate considerably under cyclic loading (Ishihara and Towhata, 1983; Zhao et al., 2020). In the UBCSAND model, the initial mean effective stress, which has a powerful effect on the shear stiffness response, influences the liquefaction resistance and the pore pressure generation. Since the initial mean effective stress-liquefaction resistance relationship is exaggerated by UBCSAND (v.904aR), the effect of principal stress rotation is not directly considered in the model (Beaty and Byrne, 2012; Beaty, 2018).

3.3.2.11. Base Excitation

The model was shaken with a sinusoidal base acceleration having a frequency of 2.0 Hz and an amplitude of a_{max} = 0.35g (Figure 3.9). The base excitation duration was 20.0 s, including two rising and falling parts, each of duration of about 1.0 s at the beginning and end of the shaking (Figure 3.9).

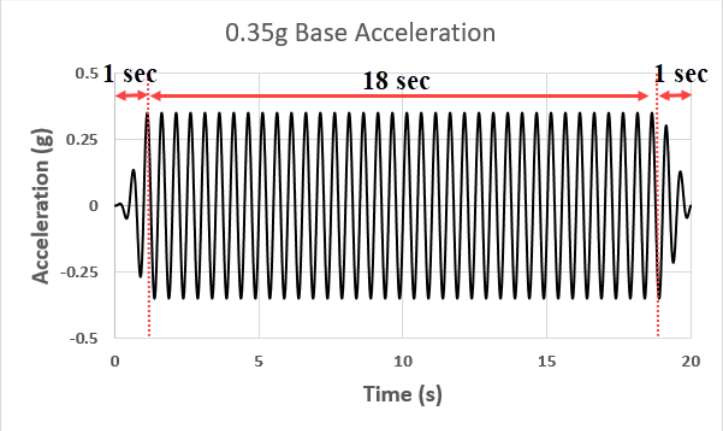

Figure 3.9. Applied base acceleration (a_{max}=0.35g) to the model

3.3.2.12. Damping

Rayleigh-damping is a combination of two frequency-dependent components: a proportional stiffness term and a proportional mass term. For soils, damping is a frequency-independent phenomenon (Topalidisz, 2018); over a limited frequency range, a frequency-independent response can be obtained, as shown in Figure 3.10. Usually, this frequency range is calibrated for the first mode of vibration since it most likely holds the biggest impact on the response. According to Figure 3.11 data, FLAC default hysteretic damping for sand with $L_1 = -3.325$ and $L_2 = 0.823$ was also considered (Seed and Idriss 1970).

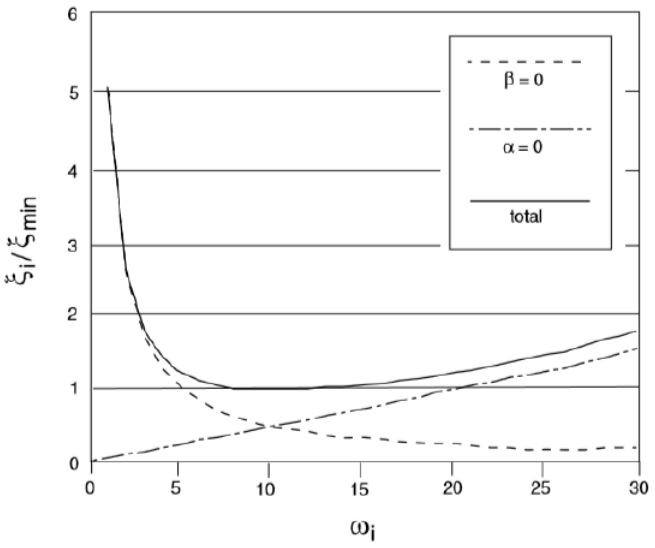

Figure 3.10. Variation of normalized critical damping ratio with angular frequency (Source: Itasca, 2011)

Data set	Default	Sig3	Sig4	Hardin
Sand – upper range (Seed & Idriss 1970)	$L_1 = -3.325$ $L_2 = 0.823$	$a = 1.014$ $b = -0.4792$ $x_o = -1.249$	$a = 0.9762$ $b = -0.4393$ $x_o = -1.285$ $y_o = 0.03154$	$\gamma_{ref} = 0.06$

Figure 3.11. Numerical fits to seed and Idriss data for sand (Source: Itasca, 2011)

3.3.2.13. Scaling

The scaling factors for 1g model tests are theoretically derived based on the mechanics of model tests (Iai, 1989). All the scaling factors are determined by the scaled length (μ), density (μ_r), and strain (μ_ρ). In practice, the soils are often the same for model and prototype. The scaling factor for the strain is determined by $\mu[(V_S)m/(V_S)p]^2$, where $(V_S)m$ and $(V_S)p$ denote the shear wave velocities of soil deposits in the model and the prototype, respectively (Iai and Sugano, 1999).

All required parameters of the physical model were scaled using the similitude law suggested by Iai et al. (2005). Considering the dimensions of the laminar box, a geometric scale of λ=10 was used and introduced (Table 3.2). Detailed information about scaling factors is available in Haeri et al. (2012).

Table 3.2. Scaling factors for 1g model tests
(Source: Iai et al. 2005)

Parameter	Scaling factors proposed by Iai et al. (Prototype/Model)	Scaling factors in this study (Prototype/Model)
Length (L)	λ	10.0
Density (ρ)	λ_ρ	1.0
Strain (ε)	λ_ε	1.0
Time (t)	$(\lambda\,\lambda_\varepsilon)^{0.5}$	3.162
Frequency (f)	$(\lambda\,\lambda_\varepsilon)^{-0.5}$	0.3162
Acceleration ($\ddot{u}$)	1.0	1.0
Displacement (u)	$\lambda\,\lambda_\varepsilon$	10.0
Stress (σ)	$\lambda\,\lambda_\rho$	10.0
EI of pipe	$\lambda^5\lambda_\rho/\lambda_\varepsilon$	100000
EA of pipe	$\lambda^3\lambda_\rho/\lambda_\varepsilon$	1000

3.4. Verification of the Numerical Modelling

To verify the numerical modeling, 1-g shaking table tests previously performed by Ecemis et al. 2021 were considered. The numerical simulations are carried out using the plane strain Finite Difference program, FLAC2D (Itasca Consulting Group, 2011). The physical model geometry and material properties are transformed into the prototype scale. The lateral dimension is adopted as 16 m, and the height of the model is 14 m. The samples are prepared from two layers, the bottom dense sand layer with 6.5 m height and a top loose sand layer with 7.5 m height. The total soil medium is discretized into about 900 Finite Difference meshes in 28 rows and 32 columns, and the zones are set finer around the buried pipe for more precision in this area (Figure 3.12). The pipe is divided into eight segments with three degrees of freedom at each node (two displacements and one rotation).

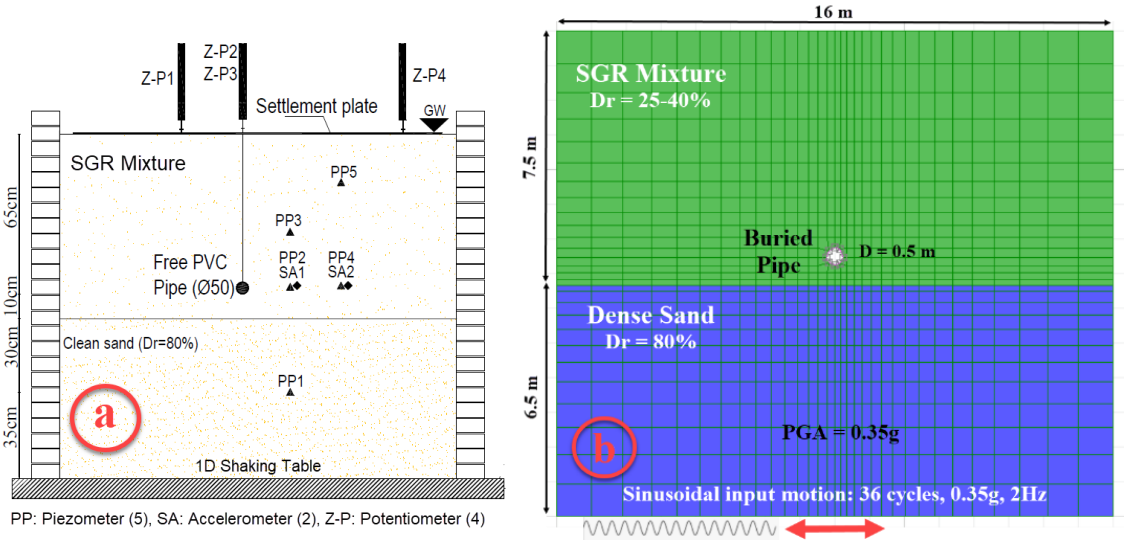

Figure 3.12. a) Side view of the physical model tests and the location of installed instruments (Source: Ecemis et al., 2021), b) prototype geometry and finite difference zone in FLAC2D

Figure 3.12a shows the view of the experimental samples and the location of the installed instruments in the test. The 1-g shaking table testing system was developed to investigate large soil samples under 1D sinusoidal excitation (Ecemis, 2013). The prepared samples were 1.6 m in length, 0.4 m in width, and 1.4 m in height. The model consisted of a 0.75 m thick liquefiable loose SGR mixture layer with a relative density (D_r) of 25-40 % over a dense, clean sand layer with D_r of 80 %. The water table was at the top layer of the surface. The 50-mm-diameter pipe was buried at a depth of 65 cm.

The bottom dense sand layer stayed the same for all samples, but the loose top layer was comprised of SGR mixtures with 10%, 20%, and 30% rubber by volume. The granulated rubber's dimension was 2.5-5 mm. Table 3.3 shows the index properties and the average initial relative density (D_r) of the loose layer.

Properties of GR are given in ASTM D6270-98, and the material properties of the sand-GR mixture are reported by Ecemis et al. 2021. The pipe was assumed to behave elastically with elasticity modulus and Poisson's ratio of 3316 MPa and 0.35, respectively. The unit weight of the pipe material was 13.83 kN/m^3. More details regarding the shaking table tests can be found at (Ecemis et al. 2021).

Table 3.3. Mechanical properties of the Sand-Granulated Rubber mixture (Source: Ecemis et al. 2021)

Test #	GR ratio (by volume)	GR dimension	e_{max}	e_{min}	D_{10}	D_{50}	C_u	C_c	γ_{sat}	D_r^*
-	(%)	(mm)	-	-	(mm)	(mm)	-	-	(kN/m^3)	(%)
T5	10	2.5-5	0.67	0.48	0.11	0.2	2.0	1.31	19.27	26
T6	20	2.5-5	0.53	0.37	0.11	0.2	2.0	1.34	19.16	35
T7	30	2.5-5	0.46	0.29	0.12	0.2	1.91	1.28	18.65	39

GR = Granulated Rubber, γ_{sat} = Saturated unit weight, D_r = Average initial relative density of the mixture (*CPT Results), D_{10} = Effective particle size, D_{50} = Mean grain size of the particle, C_u = Coefficient of uniformity, C_c = Coefficient of curvature, e_{max} = Maximum void ratio, and e_{min} = Minimum void ratio.

A total of two stages were implemented in the numerical analyses. The first stage was the static analysis, where the model's bottom was fixed in both horizontal and vertical directions. On the other hand, the lateral boundaries were fixed only in the horizontal direction. Correspondingly, the soil surface was assumed to be flat and free of loadings (self-weight). The water table was assumed to be at the top layer of the surface. The second stage was the dynamic analysis, and a horizontal dynamic excitation with a maximum acceleration of 0.35 g was applied at the base (Figure 3.9). After applying compliant boundary conditions, fixed-boundary to the base, and free-field conditions to the lateral boundaries, the dynamic analysis was conducted. The free-field boundaries were adopted to the sides boundaries to prevent the energy from flowing out and produce conditions identical to those in an infinite model. The free-field boundaries should be placed to minimize wave reflections (Itasca, 2011). During the dynamic loading for accurate high-frequency shear wave transmission, the dimension of the soil elements was limited to a maximum height, which was less than 1/10 of the wavelength of the input wave (Kuhlemeyer and Lysmer, 1973). The selected soil element size was chosen to be less than 0.25 m around the pipe. For the SGR mixture, the size of the elements gradually increased with proximity to the side boundaries.

To perform a dynamic analysis of the buried pipeline, a proper understanding of pipe-soil interaction was required as it plays an essential role during seismic excitation. An interface was used for modelling the interaction between the pipe and the surrounding soil. FLAC presents interfaces that are characterized by coulomb sliding and/or tensile separation. The properties of interfaces are defined by friction, cohesion, dilation, normal and shear stiffness, and tensile strength (Itasca, 2011). The interaction between soil and

pipe was represented as normal, and shear springs with linear spring-slider systems, preferred by several researchers, were utilized (e.g., Sun et al., 2019; Mahmoud et al., 2020). The relative displacements in the soil-pipe interface are controlled by the normal (K_n) and shear stiffness (K_s) parameters, which were set at ten times the equivalent stiffness of the stiffest neighboring zone (Itasca, 2011). The interface friction angle between the pipe and the soil was defined as about two-third of the soil internal friction angle. The impermeable hydraulic boundary was considered at the interface of pipe and SGR mixture as well.

3.4.1. Soil Constitutive Models Calibration

During the first stage, the two soil layers were simulated by the Mohr-Coulomb constitutive model, and the stresses were set based on the self-weight of the soil due to gravity loading. The soil parameters used in the numerical analyses were determined on the basis of the cone penetration tests performed before the shaking table tests. More details regarding the cone penetration tests can be found in Ecemis et al. 2021. For a Poisson's ratio (υ) of 0.25, the initial bulk modulus (K_0) of the soil was determined from the initial shear modulus, G_0. The first analysis stage aims to set equilibrium stresses and pore pressures in the soil to provide proper initial stress before dynamic simulation. At rest, the earth pressure coefficient K_0' of 0.5 was considered to estimate the initial horizontal effective stress based on the vertical effective stress.

Then the dynamic analysis was conducted after determining the dynamic soil properties, applying compatible boundary conditions to the base and the lateral boundaries, and defining the input excitation to the model's base. The shake table models were shaken with a sinusoidal base acceleration by a frequency of 2.0 Hz and an amplitude of $a_{max}/g = 0.35$. As shown in Figure 3.9, the duration of excitation was 20.0 s, with two increasing and decreasing sections, with a duration of about 1.0 s at the starting and ending of the shaking.

During the second stage (the dynamic analysis), the advanced UBCSAND soil constitutive model simulated the soil layers. The expanding verification method requires more reliable UBCSAND inputs when adjusting laboratory data. The UBCSAND model was verified to obtain the excess pore pressure value and determine the uplift of the buried pipe during the shaking table tests performed in the laboratory. In the UBCSAND model,

the elastic response is declared on the basis of the elastic shear modulus (G^e) and the bulk modulus (B^e), which are stress level-based (Beaty and Byrne, 2011). For each test, the shear modulus and the shear modulus number (K_G^e) were assessed by applying the equations preferred by (Beaty and Byrne, 2011; Seed et al., 1986), respectively.

$$G^e = 4382 \times (N_1)_{60}^{0.333} \times (\sigma'_m)^{0.5} \tag{3.27}$$

$$K_G^e = \frac{G^e}{P_a \times \left(\frac{\sigma'_m}{P_a}\right)^{0.5}} \tag{3.28}$$

where σ'_m is the mean initial effective stress, P_a is the atmospheric pressure in kPa, and $(N_1)_{60}$ is the normalized standard penetration number. The Equation proposed by Robertson et al., 1983 was used to estimate the $(N_1)_{60}$ from the cone penetration test results obtained at distinct depths (Ecemis, 2021). The average cone penetration resistance (qc_{1N}) was 142, 183, and 273 kPa in the SGR mixture layer for T5, T6, and T7 samples. Therefore, the $(N_1)_{60}$ value in the SGR mixture changed between 4 and 6. For mean effective stress at pipe level and shear modulus, K_G^e was evaluated between 695 and 795. Beaty and Byrne, 2011 indicated that K_G^e can range from about 500 to 2000 for loose to dense sand, respectively. Then, elastic bulk modulus (B^e) was specified by the subsequent Equation (Beaty and Byrne, 2011):

$$B^e = \frac{K_G^e}{K_G^e} \times G^e \tag{3.29}$$

where K_B^e is the bulk moduli number and K_B^e /K_G^e is related to the Poisson's ratio. For Poisson's ratio around 0.0 to 0.2, K_B^e /K_G^e ratio varied between 0.65 and 1.35. This ratio (K_B^e /K_G^e) for a Poisson's ratio of 0.25 was specified as 1.7. The K_B^e was evaluated between 1180 and 1350. The plastic response in this model is managed by flow rule and yield surface. G_i^P is the plastic modulus at low-level stress ratio, and it is approximated

through the Equation $G_i^P \approx 3.7 \times D_r^2 \times G^e + P_a$ (Byrne, 2004). D_r and φ_f are the relative density and the peak friction angle, where φ_f changes with constant volume friction angle (φ_{cv}), and D_r. D_r was also directly measured from CPT test results. The measurements ranged from 25-40% for samples with three different GR ratios (Ecemis et al., 2021).

The flow rule relating the plastic shear strain increment, $d\gamma^p$, to plastic volumetric strain increment, $d\varepsilon_v^p$, is given by the following Equation (Beaty and Byrne, 2011; Beaty, 2018):

$$d\varepsilon_v^p = (\sin\varphi_{cv} - \eta)d\gamma^p \tag{3.30}$$

where η is the shear stress ratio (τ/σ'). The material is in a constant-volume condition when $\eta = \sin\varphi_{cv}$. When η is higher than $\sin\varphi_{cv}$, the material shows dilative behavior. Conversely, when η is lower than $\sin\varphi_{cv}$, the material shows contractive behavior (Beaty and Byrne, 2011; Chou, 2021). Laboratory studies on the sand-tires mixtures to estimate their shear strength behavior was conducted by Attom, 2006; Christ and Park, 2010; and Marto et al., 2013. The results indicated that addition of granulated rubber into sand could increase the internal friction angle.

Material damping of the soils, resulting primarily from material failure during liquefaction, is considered to provide sufficient damping. Although hysteretic damping is included through plastic strain simulation in UBCSAND (Beaty, 2018), a small viscous damping is also considered for numerical stability and energy dissipation during elastic cycles. Newmark and Hall, 1982 suggested a critical damping value between 2% and 5%. Then, Rayleigh damping was specified with 5% damping at a center frequency of 15 Hz for the numerical modeling. This frequency was estimated by performing simulations on undamped elastic models and material damping for structural elements not included in this study.

The calibrated UBCSAND model input parameters for the SGR mixture are reported in Table 3.4. To investigate the liquefaction phenomenon, pore pressure ratio in the depth of 105, 65, and 40 cm of the surface equal to PP1, PP2, and PP3 piezometers (Figure 3.12a) were derived and compared with experimental results. Figure 3.13a-c and Figure 3.14 present the EPWP generation and the buried pipe uplift obtained by the

calibrated constitutive models compared to those interpreted from the shaking table tests (T5, T6, and T7). The rational analogy between measured and simulated results suggests that the calibrated model can properly simulate the behavior of the SGR mixture, both in terms of liquefaction triggering and uplift of pipes.

Table 3.4. Initial model parameters for UBCSAND

Parameter	Index	Description	Value
m_n160	$(N1)_{60cs}$	Relative density index	4-6
m_kge	K_G^e	Elastic shear modulus number	695-795
m_kb	K_B^e	Elastic bulk modulus number	1180-1350
m_ne	n_e	Stress exponent for elastic shear modulus	0.5
m_me	m_e	Stress exponent for elastic bulk modulus	0.5
m_kgp	G_i^P	Plastic shear modulus number	-
m_np	np	Stress exponent for plastic shear modulus	0.4
m_rf	R_f	Failure ratio for hyperbolic curve	0.6-1.0
m_phicv	ϕ_{cv}	Constant volume friction angle	36-39
m_phif	ϕ_f	Peak effective friction angle for undrained loading	-
m_hfac1	-	Calibration factor for plastic shear modulus	0.5

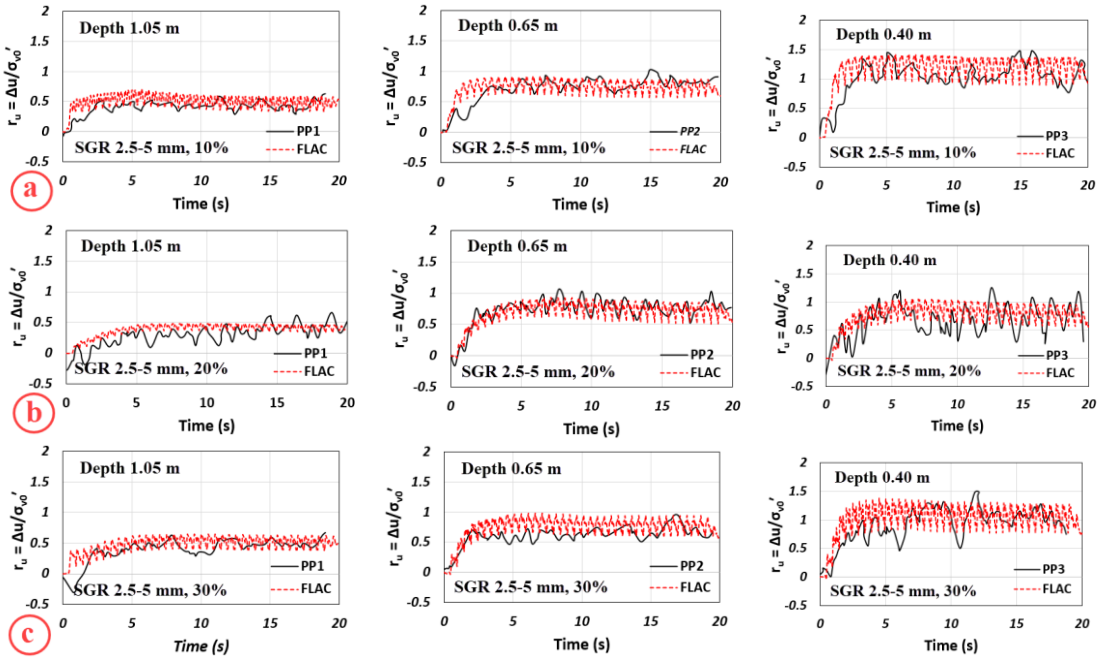

Figure 3.13. Comparison of tests and simulation results of pore water pressure ratio ($r_u = \Delta u/\sigma_{v0}'$) at depths of 105, 65 and 40 cm, a) 10%, b) 20%, and c) 30% GR by volume

The computed excess pore pressures ratio ($r_u = \Delta u/\sigma_{v0}'$) obtained from 1.05, 0.65, and 0.4 m depth for the sample with SGR are compatible with the measured values. The results indicate that the numerical simulation using the UBCSAND soil constitutive model could estimate EPWP and accurately predict the liquefaction phenomenon.

Figure 3.14 compares the pipe uplift amounts from the experimental and numerical modeling. The pipe uplift measured during the base excitation in the laboratory is compared with the uplift results obtained from the numerical simulation using UBCSAND. There is some difference between the experimental and the numerical uplift time histories. However, numerical modeling could accurately predict the pipe's ultimate uplift in the 30% GR in the mixture (T7).

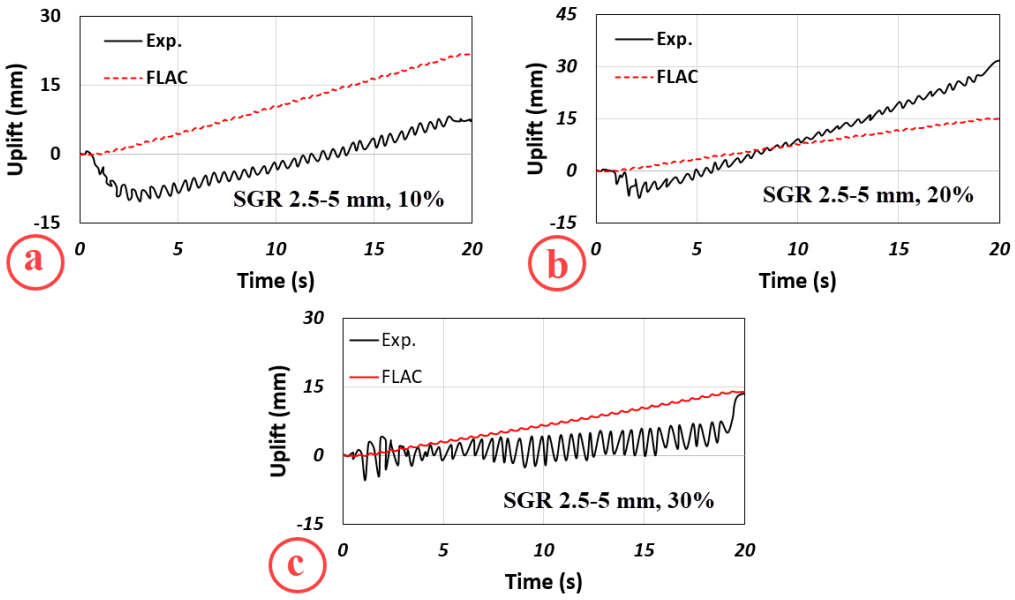

Figure 3.14. Comparison of experimental and numerical results of pipe uplift for a) 10%, b) 20%, and c) 30% GR by volume

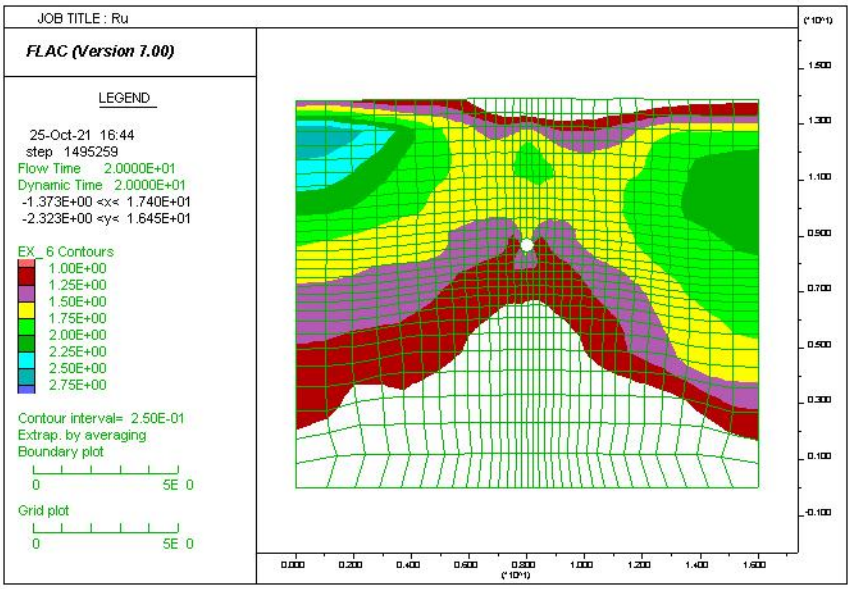

Figure 3.15. Counter of $r_u = \Delta u/\sigma_{v0}'$ in FLAC 2D

3.5. Discussion and Conclusion

The computed excess pore pressures ratio ($r_u = \Delta u/\sigma_{v0}'$) obtained from 1.05, 0.65, and 0.4 m depth is in good agreement with the measured values. The measurements and computed results show that the numerical modeling with the UBCSAND soil constitutive model could simulate excess pore water pressure and accurately predict the liquefaction phenomenon in saturated sand.

The pipe uplift recorded during the base shaking is compared with the computed uplift using the numerical model UBCSAND. There is some difference between the experimental and numerical results. However, numerical modeling could predict pipe uplift accurately in STC 30% sample.

CHAPTER 4

DISCUSSION OF PARAMETRIC NUMERICAL STUDY

4.1. Introduction

The numerical simulation of liquefaction is an extremely complicated process as it is a highly nonlinear problem (Topalidisz, 2018). This research aims to analyze the effect of cyclic loading-induced liquefaction on buried circular pipes. The dynamic performance of buried pipes in liquefied soil was examined using the plane strain finite difference program, FLAC 2D (Itasca, 2011). It can simulate liquefaction by coupling the differential equations of the solid and fluid phases. FLAC can perform coupled effective stress models (Itasca, 2011). Explicit solution methods and finite different element formulation are two significant aspects of FLAC in comparison with other analysis methods. Recently, FLAC was used to observe the seismic behavior of buried structures in liquefiable and non-liquefiable soils (Zheng et al.,2019; Mahmoud et al., 2020). In this study, the liquefaction-induced uplift and the failure mechanism of the buried pipelines are appraised using the FLAC 2D software and the UBCSAND soil constitutive model under cyclic loading.

4.2. Parametric Study

In this section, a series of parametric analyses were carried out to realize the liquefaction-induced uplift of buried pipelines in the SGR mixture (with GR 2.5-5 mm and 30%) under different pipe diameter (D), burial depth (H), and maximum acceleration (a_{max}). The physical model geometry and material properties were transformed into the prototype scale (Table 3.2). As shown in Figure 4.1, the lateral dimension and the height of the model were 16 m and 14 m, respectively. However, the samples were prepared from dense bottom sand and loose top SGR layers with 4 m and 10 m in height. For measuring the r_u results, a total of three locations—in the middle of the dense sand layer (PP01), at pipe level (PP02), and near the surface (PP03)—were considered. Two points at the upper and undersides of the pipe (PP05 and PP06) were also considered to estimate

the upward force due to PWP generation. For deriving the liquefaction-induced uplift and the surface displacement time history, two points, ZP01 and ZP02, were defined. The behavior of the SGR mixture was simulated using the UBCSAND model, and the pipe was assumed to be a linear elastic substance. According to the numerical modeling verification results, the infill SGR mechanical properties of sample T7, according to Table 3.3 (GR size 2.5-5 mm and ratio of 30%), were selected as the parametric study's soil properties.

To investigate the effect of geometric parameters such as pipe diameter (D), burial depth (H), and the maximum acceleration (a_{max}) on the behavior of the buried pipe in liquefiable sand-granulated rubber mixture, 72 numerical modeling samples with the D=5, 10, 15, and 20 cm, H=35, 45, 55, 65, 75, and 85 cm and a_{max}=0.2g, 0.35g, and 0.5g were simulated.

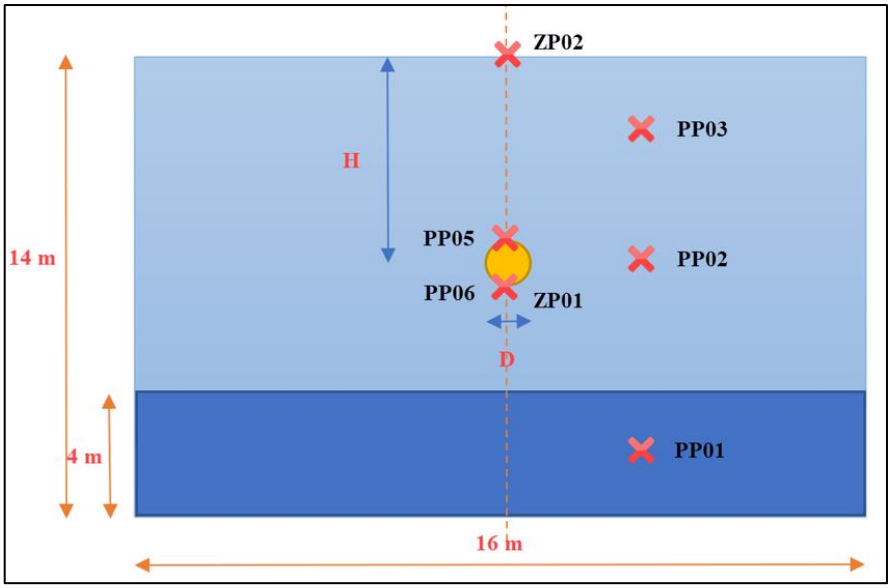

Figure 4.1. Sample dimension modeled for parametric study in FLAC 2D

4.2.1. Input Acceleration

The samples were shaken with a sinusoidal base acceleration having a frequency of 2.0 Hz and amplitudes of a_{max} = 0.2g, 0.35g, and 0.5g (Figure 4.2). The base excitation duration was 20.0 s, including two rising and falling parts, each of duration of about 1.0 s at the beginning and end of the shaking (Figure 4.2).

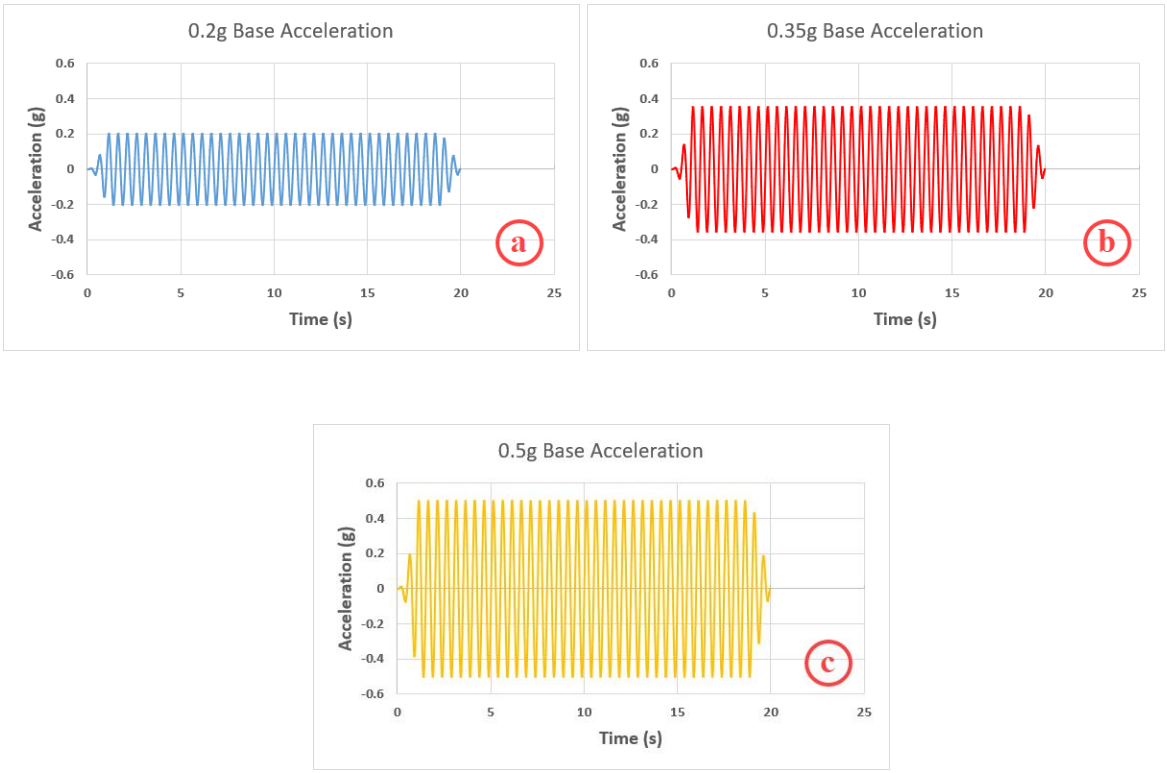

Figure 4.2. Applied base acceleration in FLAC a) a_{max}=0.2g b) a_{max}=0.35g c) a_{max}=0.5g

4.2.2. Numerical Results

Tables 4.1 to 4.6 report the complete numerical modeling results, including pipe uplift, surface displacement, and EPWP ratio in three different levels (Figure 4.1) based on different values of pipe burial depth and maximum input acceleration.

Table 4.1. Result of samples buried in H=35 cm

H=35 cm							
a_{max}	D (cm)	D/H	Uplift (ZP01) (mm)	Settlement (ZP02) (mm)	r_u01	r_u02	r_u03
0.2g	5	0.143	3.41	-5.51	0.44	1.20	0.95
	10	0.285	9.26	-2.42	0.45	1.10	0.90
	15	0.428	18.20	+2.28	0.42	0.90	0.75
	20	0.571	26.34	+13.20	0.40	0.75	0.70
0.35g	5	0.143	10.57	-6.95	0.42	1.20	0.95
	10	0.285	20.96	-2.81	0.45	1.10	0.92
	15	0.428	33.18	+3.86	0.40	0.88	0.78
	20	0.571	46.10	+13.01	0.38	0.78	0.62
0.5g	5	0.143	12.80	-6.05	0.48	1.20	0.95
	10	0.285	27.54	-1.00	0.45	1.10	1.00
	15	0.428	41.64	+6.05	0.45	0.95	0.80
	20	0.571	55.73	+15.42	0.42	0.80	0.70

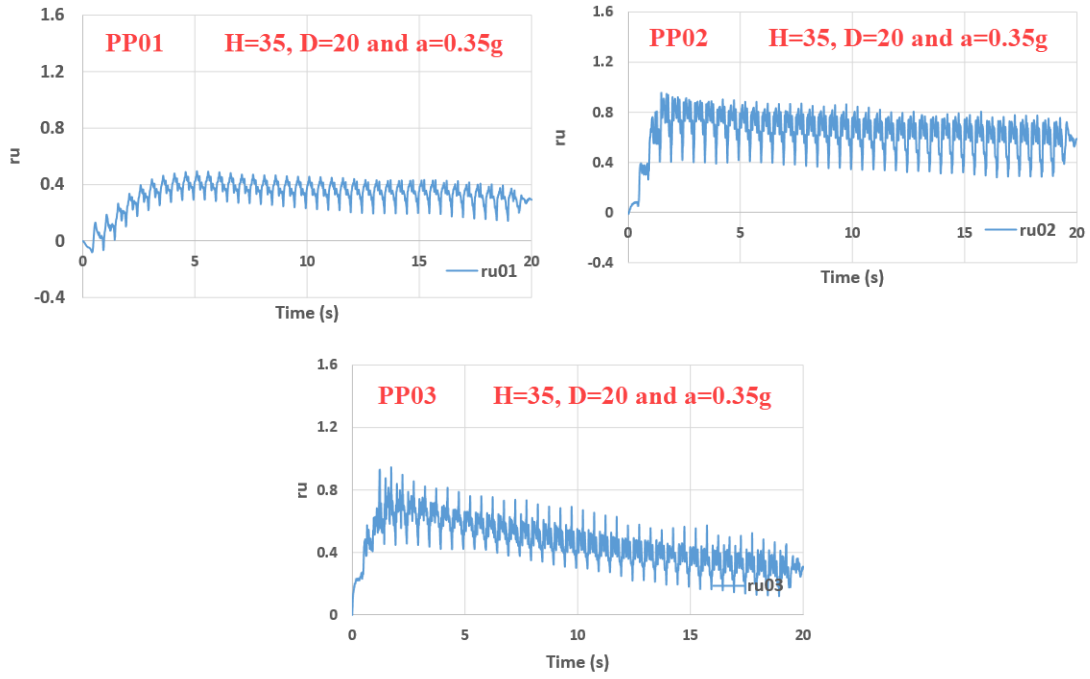

Figure 4.3. r_u ($\Delta u/\sigma_{v0}'$) results of numerical modeling at dense sand (PP01), Pipe level (PP02), and near the surface (PP03) (H=35 cm, D=20 cm, and a_{max}=0.35g)

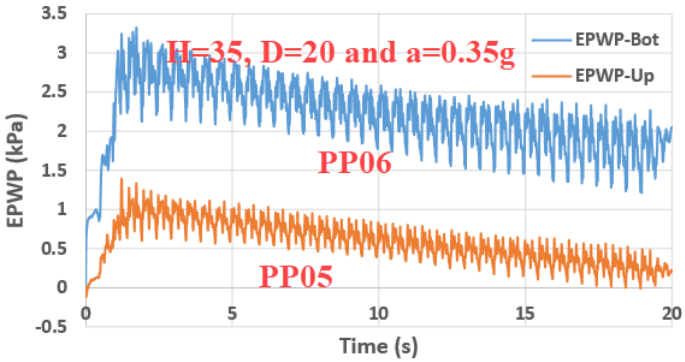

Figure 4.4. Excess pore water pressure at the bottom (PP06) and Top (PP05) of buried (H=35 cm, D=20 cm, and a_{max}=0.35g)

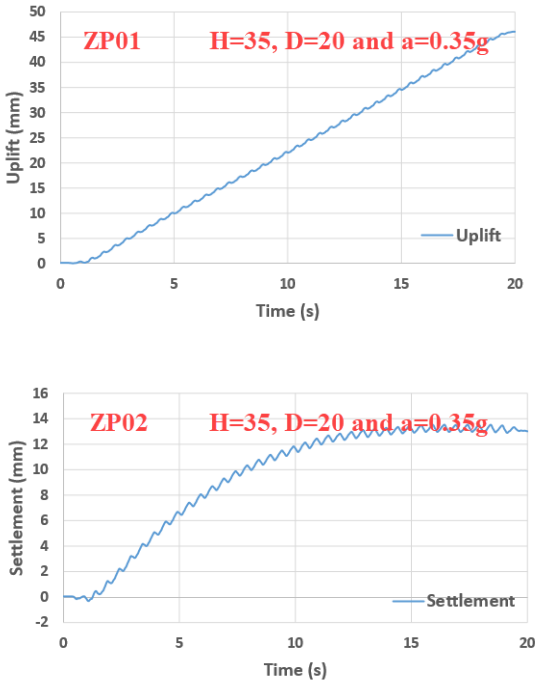

Figure 4.5. Buried pipe Uplift (ZP01) and surface displacement (ZP02) (H=35 cm, D=20 cm, and a_{max}=0.35g)

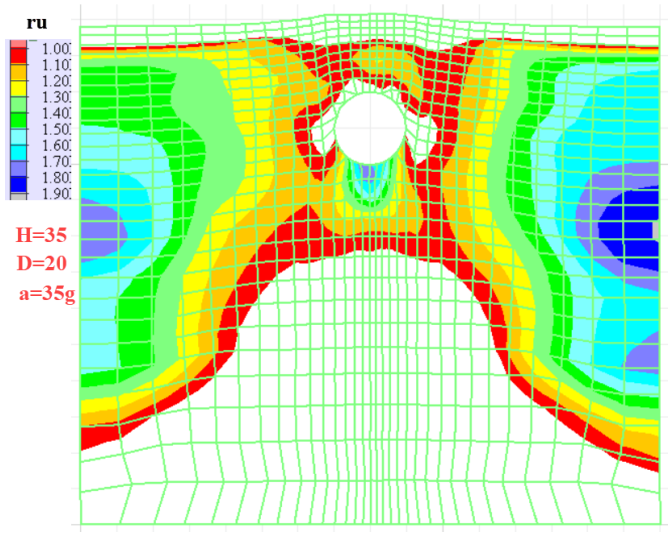

Figure 4.6. Counter of r_u ($\Delta u/\sigma_{v0}'$) obtained from FLAC at the end of excitation (H=35 cm, D=20 cm, and a_{max}=0.35g)

Table 4.2. Result of samples buried in H=45 cm

H=45 cm							
a_{max}	D (cm)	D/H	Uplift (ZP01) (mm)	Settlement (ZP02) (mm)	r_u01	r_u02	r_u03
0.2g	5	0.111	4.75	-6.62	0.46	1.40	1.20
	10	0.222	8.62	-4.80	0.45	1.15	1.15
	15	0.333	13.36	-1.08	0.42	0.90	1.05
	20	0.444	20.50	4.18	0.42	0.78	0.90
0.35g	5	0.111	13.08	-8.39	0.45	1.40	1.20
	10	0.222	20.78	-6.16	0.44	1.10	1.15
	15	0.333	29.45	-1.80	0.42	0.95	1.10
	20	0.444	38.96	6.08	0.40	0.80	0.92
0.5g	5	0.111	15.75	-7.73	0.48	1.40	1.25
	10	0.222	25.61	-5.02	0.45	1.50	1.20
	15	0.333	35.56	0.10	0.45	0.95	1.10
	20	0.444	48.27	9.13	0.42	0.80	1.00

Table 4.3. Result of samples buried in H=55 cm

H=55 cm							
a_{max}	D (cm)	D/H	Uplift (ZP01) (mm)	Settlement (ZP02) (mm)	r_u01	r_u02	r_u03
0.2g	5	0.090	7.34	-5.98	0.42	1.25	1.25
	10	0.182	9.97	-5.84	0.42	1.05	1.25
	15	0.273	12.47	-4.57	0.44	0.95	1.05
	20	0.364	18.18	-0.37	0.44	0.85	1.00
0.35g	5	0.090	18.18	-7.50	0.42	1.20	1.30
	10	0.182	21.53	-8.00	0.40	1.00	1.25
	15	0.273	26.58	-5.10	0.44	0.95	1.05
	20	0.364	33.03	-1.15	0.42	0.80	1.00
0.5g	5	0.090	20.84	-7.40	0.42	1.30	1.30
	10	0.182	25.98	-6.93	0.42	1.10	1.30
	15	0.273	32.96	-4.29	0.44	0.95	1.10
	20	0.364	44.20	-0.54	0.42	0.80	1.05

Table 4.4. Result of samples buried in H=65 cm

H=65 cm							
a_{max}	D (cm)	D/H	Uplift (ZP01) (mm)	Settlement (ZP02) (mm)	r_u01	r_u02	r_u03
0.2g	5	0.076	8.41	-9.67	0.55	1.25	1.70
	10	0.154	10.06	-6.80	0.42	0.82	1.35
	15	0.231	12.03	-5.43	0.42	0.78	1.15
	20	0.308	14.03	-3.12	0.43	0.68	1.20
0.35g	5	0.076	21.16	-10.46	0.52	1.30	1.80
	10	0.154	22.61	-8.38	0.40	0.82	1.35
	15	0.231	24.81	-7.27	0.40	0.80	1.30
	20	0.308	27.79	-3.77	0.42	0.70	1.25
0.5g	5	0.076	30.02	-11.17	0.37	1.25	1.70
	10	0.154	26.79	-7.59	0.42	0.80	1.40
	15	0.231	30.34	-7.39	0.42	0.85	1.25
	20	0.308	34.00	-2.46	0.42	0.70	1.30

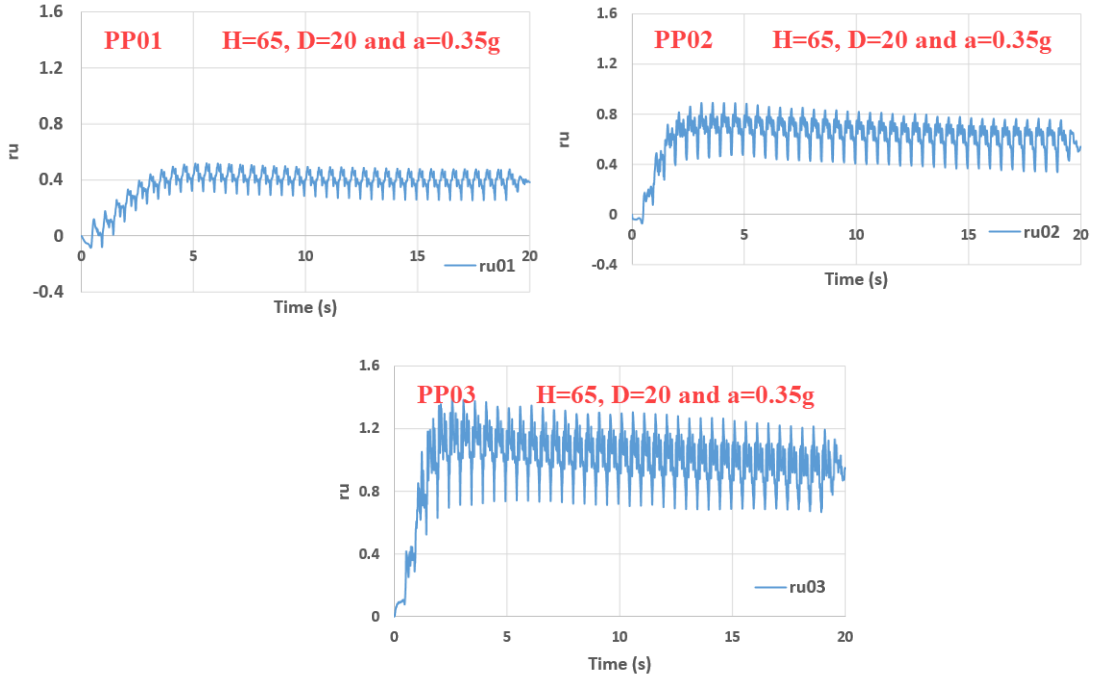

Figure 4.7. r_u results of numerical modeling at dense sand (PP01), Pipe level (PP02), and near the surface (PP03) (H=65 cm, D=20 cm, and a_{max}=0.35g)

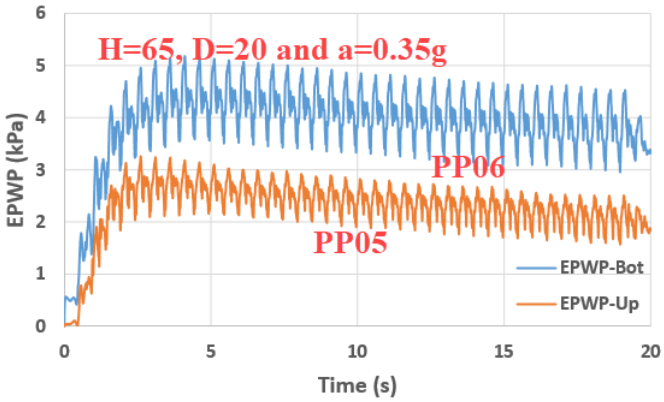

Figure 4.8. Excess pore water pressure at the bottom (PP06) and Top (PP05) of buried (H=65 cm, D=20 cm, and a_{max}=0.35g)

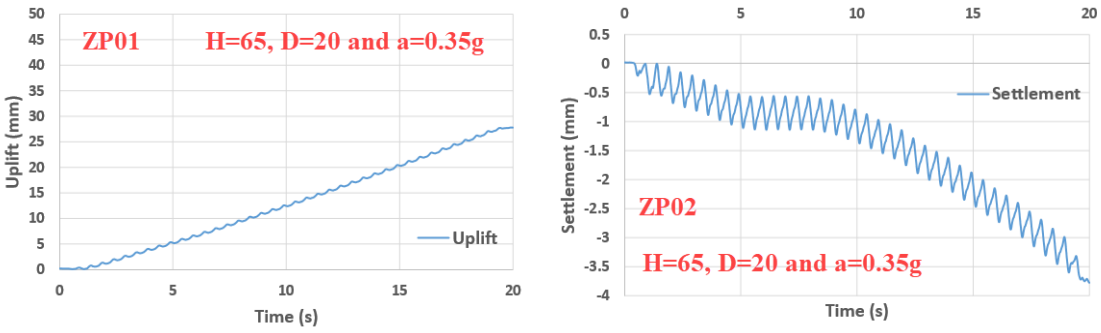

Figure 4.9. Buried pipe Uplift (ZP01) and surface displacement (ZP02) (H=65 cm, D=20 cm, and a_{max}=0.35g)

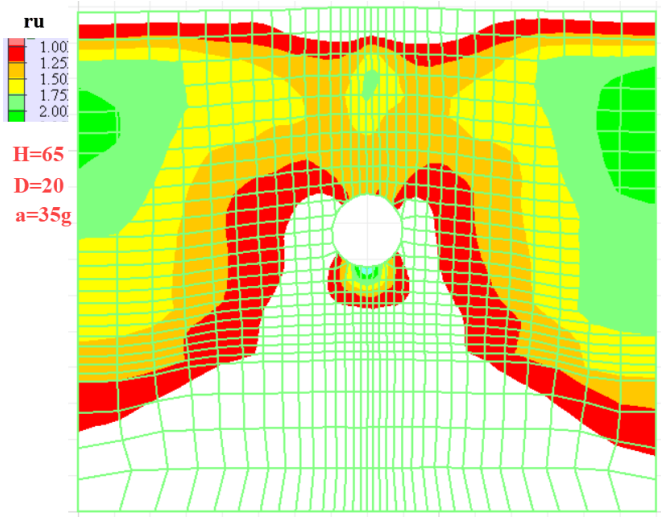

Figure 4.10. Counter of r_u obtained from FLAC at the end of excitation (H=65 cm, D=20 cm, and a_{max}=0.35g)

4.2.2.1 Simulation Results – EPWP Generation

Although full liquefaction occurs when EPWP reaches the initial vertical effective stress (σ'_{v0}) or when the pore water pressure ratio ($r_u = \Delta u/\sigma'_{v0}$) reaches 1.0, Mahmoud et al., 2020 stated that liquefaction could also occur when the pore water pressure ratio is slightly lower than 1.0. In this study, r_u = 1.0 was considered to be the initiation of liquefaction.

Table 4.5. Result of samples buried in H=75 cm

H=75 cm							
a_{max}	D (cm)	D/H	Uplift (ZP01) (mm)	Settlement (ZP02) (mm)	r_u01	r_u02	r_u03
0.2g	5	0.067	9.40	-6.61	0.42	0.98	1.30
	10	0.133	10.13	-6.71	0.42	0.76	1.30
	15	0.200	10.84	-6.24	0.42	0.75	1.20
	20	0.267	11.07	-5.05	0.42	0.62	1.20
0.35g	5	0.067	22.15	-8.95	0.40	1.00	1.35
	10	0.133	23.36	-8.97	0.40	0.78	1.35
	15	0.200	23.00	-9.37	0.40	0.75	1.25
	20	0.267	21.76	-6.28	0.40	0.62	1.25
0.5g	5	0.067	27.49	-8.21	0.40	1.00	1.35
	10	0.133	28.60	-8.26	0.40	0.80	1.40
	15	0.200	27.61	-9.23	0.40	0.75	1.25
	20	0.267	25.53	-6.03	0.40	0.65	1.30

Table 4.6. Result of samples buried in H=85 cm

H=85 cm							
a_{max}	D (cm)	D/H	Uplift (ZP01) (mm)	Settlement (ZP02) (mm)	r_u01	r_u02	r_u03
0.2g	5	0.059	9.42	-6.38	0.42	0.80	1.40
	10	0.117	9.77	-6.79	0.42	0.68	1.25
	15	0.176	9.70	-5.89	0.42	0.67	1.40
	20	0.235	9.65	-5.53	0.40	0.65	1.20
0.35g	5	0.059	22.40	-8.46	0.40	0.80	1.35
	10	0.117	22.89	-9.31	0.40	0.68	1.20
	15	0.176	20.56	-8.61	0.42	0.65	1.50
	20	0.235	16.77	-8.80	0.42	0.65	1.30
0.5g	5	0.059	27.22	-8.18	0.40	0.80	1.40
	10	0.117	27.62	-9.42	0.40	0.70	1.30
	15	0.176	24.59	-7.46	0.40	0.68	1.50
	20	0.235	16.90	-8.41	0.40	0.65	1.30

For example, the EPWP generation of samples with a pipe diameter of 20 cm, buried in two different depths of 35 and 65 cm during dynamic loading with a_{max} of 0.35 g, was illustrated in Figures 4.3 and 4.7. Figures illustrate the build-up of the r_u in three different levels. It was realized that the r_u was rising by a low rate at the loading initiation. About 2 to 5 s, it reached a maximum EPWP, and then it was approximately constant until the end of loading. After 1 s, dynamic load reached a_{max}, and r_u in pipe level was about 0.5. Similar to previous studies (Liu and Song, 2006; Azadi and Hosseini, 2010), numerical simulation results show that EPWP generation causes upward water flow when

liquefaction happens, as shown in Figure 4.11. Inequality in vertical pressure due to EPWP generation under the buried pipe causes the uplift of pipe enclosed by liquefied soil. Degradation of r_u after peak point (in r_u03 for shallow buried pipe) took place because of pore pressure dissipation near the surface (Figure 4.3).

Figure 4.11 shows the SGR mixture deformation and pipe displacement for H = 65 cm, D = 20 cm, and a_{max}/g of 0.35 at the end of the loading (20 s). Considering this deformation, it is evident that the soil movement around the pipe formed circular loops on both sides with a motion from the top to the bottom of the pipe. During uplift, the buried pipe pushed the soil above aside in a manner similar to a punching failure mechanism.

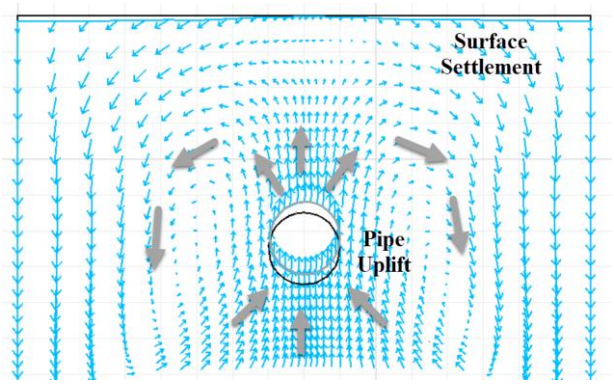

Figure 4.11. The SGR mixture deformation and pipe movement for pipe burial depth of 65 cm, the pipe diameter of 20 cm, and a_{max}/g of 0.35, at 20 s

4.2.2.2 Simulation Results – Pipe Uplift

Figures 4.4 and 4.8 depict the EPWP generation time history at PP05 and PP06 related to pipe top and bottom points, and Figures 4.5 and 4.9 show the pipe uplift and the soil surface displacement for samples with a pipe diameter of 20 cm, buried in two different depths of 35 and 65 cm under dynamic loading with a_{max} of 0.35 g. The difference between EPWPs at the top and bottom of the pipe (P_{EPP}) was utilized to obtain upward force due to the EPWP generation, F_{EPP} (Equation 2.8). Usually, the buried pipe uplift is followed by adjacent soil displacement due to the soil motion, as shown in Figures 4.6 and 4.10, where the incidence uplift of pipe was obvious against the surrounding soil settlement. As mentioned before, circular movements were observed in

the soil at both sides of the pipe. As the buried pipe moves up, the backfill soil flows from the pipe's sides to under the pipe, generating pipe uplift and soil displacement (Figure 4.11). The uplift of the pipe started at about 1.5 s, when the soil at the pipe level was near liquefaction ($r_u \approx 0.8$). Later, a more severe uplift occurred until the excitation's end before the acceleration decreased at t = 19 s.

Table 4.7 reports the FoS against uplift of four samples based on the available theoretical uplift formulation given by Chian and Madabhushi, 2012 with the same a_{max}/g of 0.35 and different burial depth ratio (H/D). According to numerical simulation results, three samples have FoS more than one, but pipe uplift was observed in all the samples. FoS against uplift was 3.5 and 0.75 for the specimens with a burial depth ratio of H/D = 7 and H/D = 1.75, respectively. However, in both samples, there was an occurrence of pipe uplift.

Figure 4.12a-b shows samples' shear strain contour with a pipe diameter of 20 cm and two different burial depths of 35 and 65 cm, respectively. In the sample with H/D = 1.75, the soil failed in the inclined wedge failure mechanism, and the shear strain reached 20% at the failure lines position. According to the direct shear test results, the shear strain, which was about 6%, was considered as failure shear strain. The inclined wedge failure lines are shown by dotted lines in this sample (Figure 4.12a). Nevertheless, the failure mechanism of the sample with H/D = 3.25 is unlike the inclined wedge failure mechanism. In this sample, the soil fails in the punching mechanism because of circular soil movement in the pipe side during pipe uplift. The shear strain contour illustrates that the shear strain remains about 5% at the inclined wedge position (Figure 4.12b).

Table 4.7. The safety factor of selected samples (calculation in Appendix A)

Sample No.	**Max. acc. (a_{max}/g)**	**Pipe diameter (D)**	**Burial depth (H)**	**Burial Depth Ratio (H/D)**	**FoS (Eq. 5)**	**Uplift**
#	**-**	**cm**	**cm**	**-**	**-**	**-**
1	0.35	5	35	7	3.50 > 1.0	Occurred
2		20	35	1.75	0.75 < 1.0	Occurred
3		5	65	13	7.50 > 1.0	Occurred
4		20	65	3.25	1.81 > 1.0	Occurred

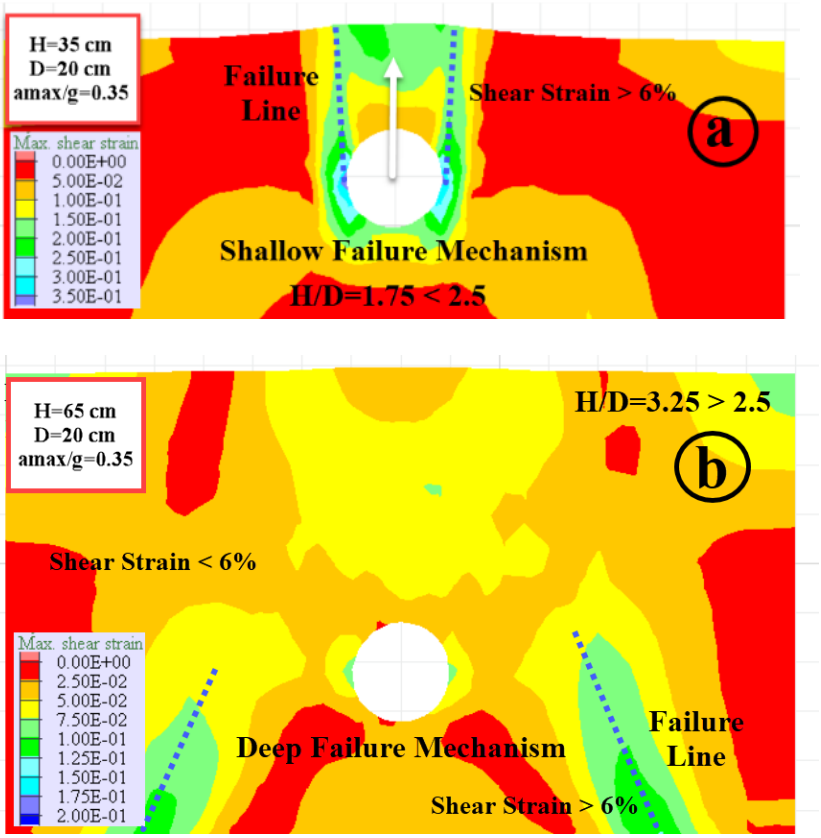

Figure 4.12. Contours of a) shallow failure mechanism of the sample with H/D = 1.75 < 2.5, and b) deep failure mechanism of the sample with H/D = 3.25 > 2.5

4.3. Failure Mechanism

4.3.1. Direct Shear Test

A series of Direct Shear Test (DST) samples of sand-granulated rubber mixture (GR 2.5-5 mm and 30%) were tested in the geotechnical laboratory of Izmir Institute of Technology under dry and saturated conditions. Laboratory tests were conducted in accordance with the ASTM D3080-11 standard. Figure 4.13 shows the shear stress-strain curves for three different vertical load values of 0.2, 0.5, and 1.0 kN.

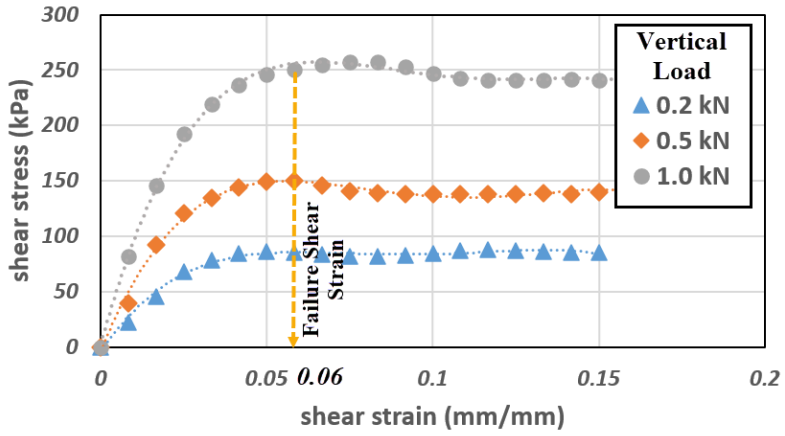

Figure 4.13. Shear Stress-Strain curves obtained from the direct shear test

As shown in Figure 4.13 for 0.2, 0.5, and 1.0 kN vertical load, shear strain increased with an increase in shear stress. The failure occurred at the shear strain about 5-7% for three different vertical load values. The test setup and failure plane are shown in Figure 4.14. Based on the DST test result, the failure shear strain can be obtained about 6%.

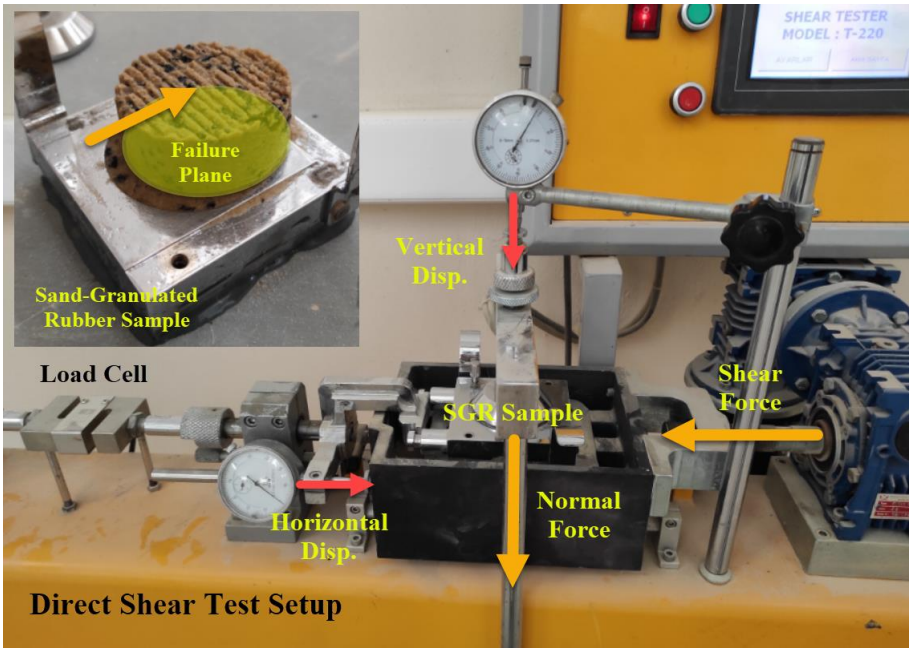

Figure 4.14. Direct shear test setup and SGR sample

4.3.2. Shallow and Deep Failure Mechanisms

This study presents the results of 72 numerical modeling samples with a burial depth ratio of H/D = 1.75 to H/D = 17. Regarding the soil surface displacement (ZP02), pipe uplift (ZP01), and shear strain contour results, the samples' failure mechanism is divided into shallow and deep failure mechanisms based on the H/D values. Figure 4.15 shows the samples' surface displacements versus H/D at three different maximum acceleration values of 0.2, 0.35, and 0.5g. As seen in the figure, H/D = 2.5 can be selected as the critical burial depth for the SGR (GR 2.5-5 mm and 30%) mixture. Then, specimens with H/D < 2.5, such as the inclined wedge model, fail in the shallow failure mechanism (Figure 4.12a), and those with H/D > 2.5, such as the punching mechanism, fail in the deep failure mechanism (Figure 4.12b). The finding shows that analytical limit-equilibrium methods based on inclined wedge failure mechanism cannot be used for deeply buried pipe because of its local failure mechanism tendency. Figures 4.16 and 4.17 show the soil movement vectors in samples (H/D=1.75<2.5 and H/D=3.25>2.5) with two different failure mechanisms. As can be seen, the soil particles movement also proves the association of the burial depth ratio (H/D) and soil failure mechanism type.

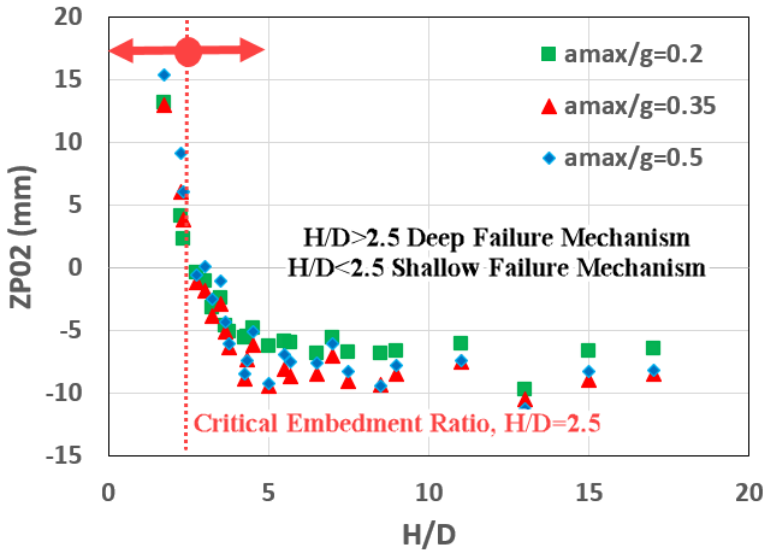

Figure 4.15. The variation of samples' surface displacements at different burial depth ratios (H/D)

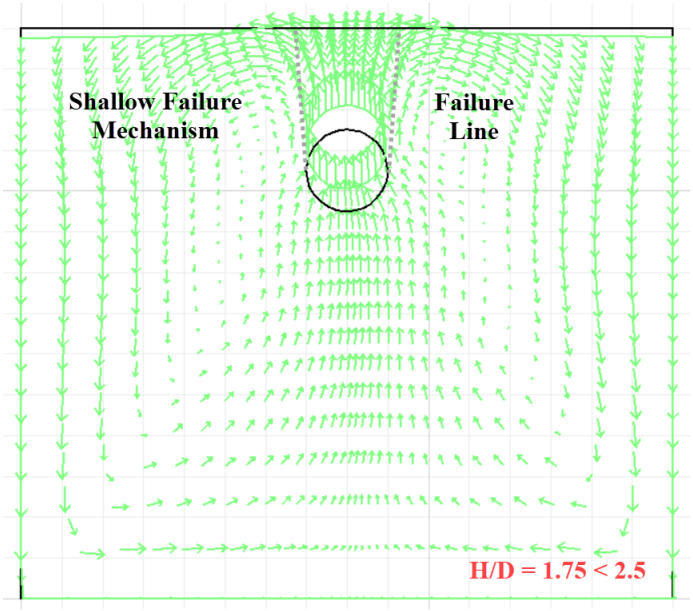

Figure 4.16. The displacement vectors of the sample with H/D=1.75<2.5

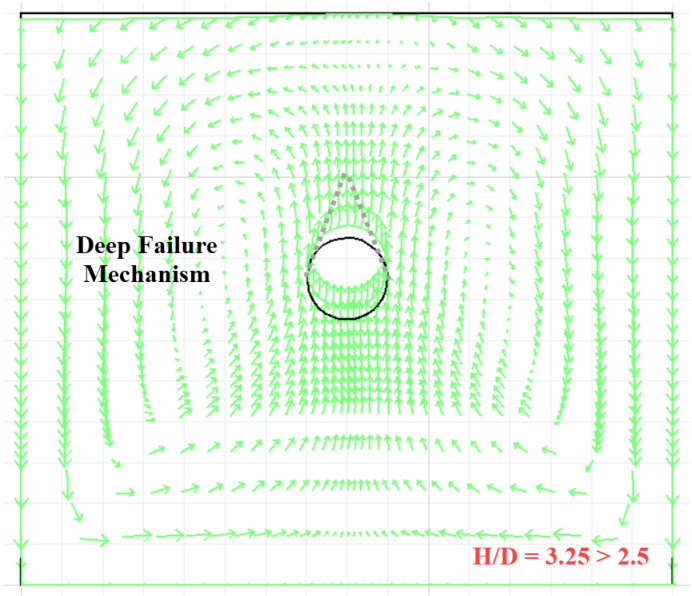

Figure 4.17. The displacement vectors of the sample with H/D=3.25>2.5

4.4. Proposed Analytical Formula

Regarding the uplift values of samples with different pipe diameter ratios (D/H) and drawing a second-order polynomial trendline of numerical data for a_{max}/g of 0.2, 0.35, and 0.5, an analytical formula was proposed to estimate the liquefaction-induced uplift of buried pipes based on the acceleration ratio (a_{max}/g) and D/H variation. The proposed equation predicts the ultimate uplift of the buried pipe in the studied SGR mixture under sinusoidal excitation with a constant frequency of 2Hz. The equation suggested in this study can be used in probabilistic analyses to assess the liquefaction-induced uplift of buried pipes in fully saturated SGR mixtures (Figure 4.18).

$$Uplift\ (mm) = 15.5t\left(\frac{a_{max}}{g}\right)^{0.95}\left(\frac{D}{H}\right)^{2} - 4.4t\left(\frac{a_{max}}{g}\right)^{1.9}\left(\frac{D}{H}\right) + 3.2t\left(\frac{a_{max}}{g}\right)^{1.3} \quad (4.1)$$

where t is the input shaking duration.

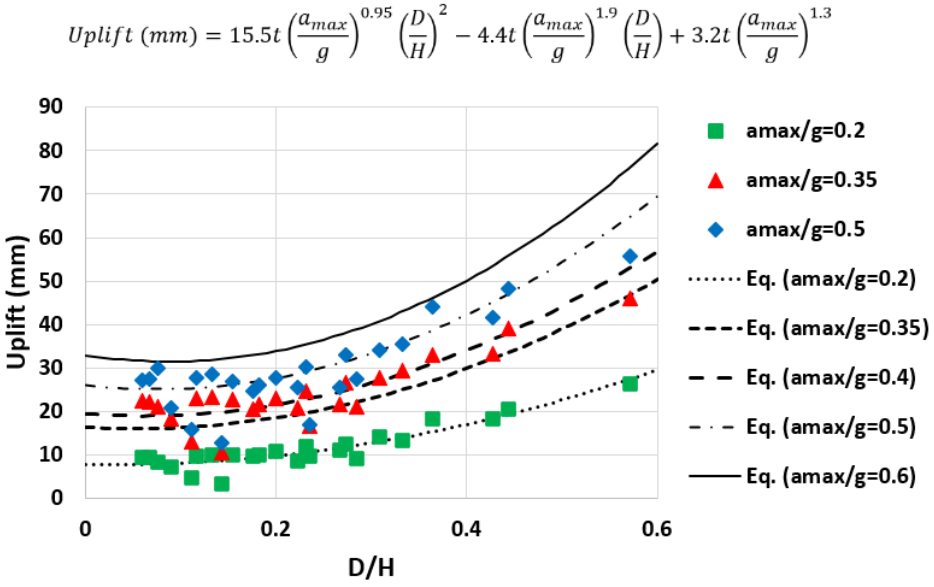

Figure 4.18. Comparing uplift values obtained from numerical study and proposed formula for a_{max}/g of 0.2 to 0.6

4.4.1. Impact of Maximum Acceleration (a_{max})

Table 4.8 compares the uplift values obtained from numerical and analytical studies for a_{max}=0.1g to 0.8g. As can be seen for a_{max}=0.1g, the sand did not experience liquefaction, and the pipe settled during the excitation.

On the other hand, the buried pipe with scaled mechanical properties started to deform slightly after a_{max}=0.7g, then using the proposed formula for a_{max}=0.2g to 0.6g can be acceptable (Figure 4.19).

Table 4.8. Result of samples buried in H=65 cm under various a_{max} values

H=65 cm						
#	D (cm)	D/H	a_{max} (g)	Numerical Uplift (mm)	Analytical Uplift (mm)	Difference %
1	20	0.3	0.1	-1.34	6.00	-
2	20	0.3	0.2	14.02	12.71	-9
3	20	0.3	0.3	25.42	19.59	-23
4	20	0.3	0.4	29.34	26.50	-10
5	20	0.3	0.5	34.00	33.35	-2
6	20	0.3	0.6	40.05	40.10	0
7	20	0.3	0.7	44.45	46.71	+5
8	20	0.3	0.8	48.75	53.15	+9

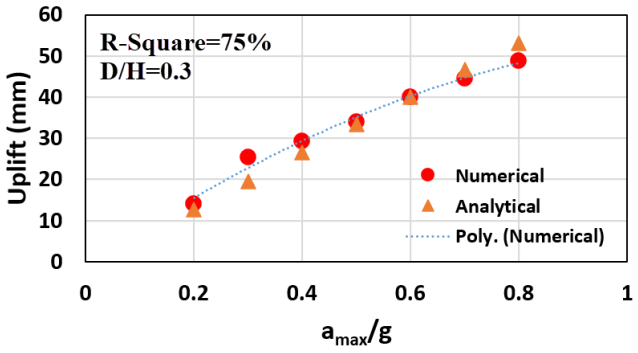

Figure 4.19. Comparing uplift values obtained from numerical and analytical studies for various a_{max}

The uplift results from experimental, numerical, and analytical studies were compared for assessing the proposed analytical formula accuracy. Figure 4.20 depicts the uplift time history of the three methods. Also, the ultimate uplift value is obtained from the methods presented in Table 4.9.

Table 4.9. Comparing the ultimate uplift amounts of Sample04 (2.5-5mm, 30%)

#	Model	Uplift (mm)
1	Experimental	14.00
2	Numerical	13.93
3	Analytical	16.10

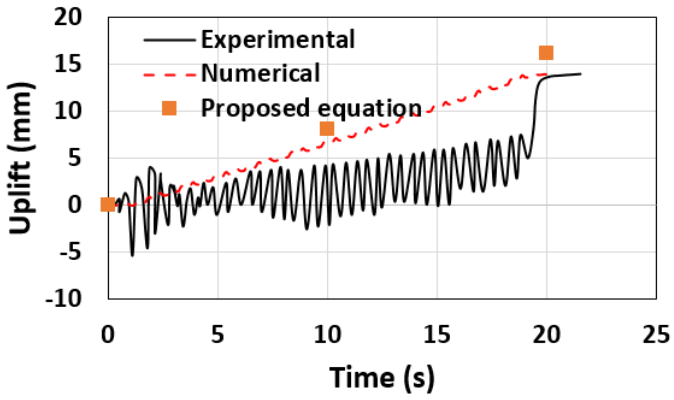

Figure 4.20. Comparing uplift values obtained from Experimental, numerical and analytical studies for Sample04 (2.5-5mm, 30%)

4.5. Summary

In this chapter, a parametric study was conducted to investigate the effects of the pipe diameter, the pipe depth, and the value of the acceleration on pipe uplift and liquefaction potential when the SGR mixture was placed as filling material. The Numerical modeling using the UBCSAND soil constitutive model could accurately simulate EPWP and forecast liquefaction in the saturated SGR mixture.

An analytical formula was proposed to estimate the liquefaction-induced uplift of buried pipes, and the soil failure mode was categorized according to the pipe's burial

depth. The critical burial depth ratio was selected H/D = 2.5. The underground pipes with H/D less than 2.5 failed shallowly, whereas those with H/D greater than 2.5 experienced a deep failure mechanism.

Despite the fact that it appears that increasing the burial depth increases the uplift safety factor of the buried structure, the results indicated that analytical limit-equilibrium methods based on the inclined wedge failure mechanism could not be used for deeply buried pipes due to the tendency of the local failure mechanism.

CHAPTER 5

SUMMARY, CONCLUSIONS, AND RECOMMENDATIONS

5.1. Introduction

This study aims to investigate the effect of cyclic loading-induced liquefaction on buried circular pipelines. The numerical analysis was made in the finite-difference software, FLAC 2D (Itasca, 2011). The first part focuses on understanding the modeling concepts necessary to describe the phenomenon accurately. Such concepts are the mechanism of the nonlinear constitutive model invoked by hysteretic damping, pore water pressure generation, shear wave propagation in 1D condition. Then, the behavior of a buried pipe in a liquefiable sand layer was studied. The previous research showed that the tire content greatly influences the shear strength of the mixture (Gotteland et al. 2005) and decreases the liquefaction impact. The inclusion of shredded waste tires enhanced the shear strength of the sands as well as the angle of internal friction (Attom 2006).

5.2. Conclusions

The dynamic behavior of buried pipe in fully saturated SGR was investigated using the UBCSAND (Beaty and Byrne, 2011) constitutive model by the finite difference program, FLAC 2D (Itasca, 2011). The liquefaction parameters were calibrated based on shaking table tests, and the constitutive model was verified with experimental results. EPWP and pipe uplift were simulated, and an analytical formula was proposed to estimate the pipe liquefaction-induced uplift. The following results were achieved from the numerical parametric study:

- The computed r_u obtained from 1.05, 0.65, and 0.40 m depth are in good agreement with the measured values. The measurements and computed results show that the numerical modeling with the UBCSAND soil constitutive model could simulate

excess pore water pressure and accurately predict the liquefaction phenomenon in saturated sand.

- The pipe uplift recorded during the base shaking is compared with the computed uplift using the numerical model UBCSAND. There is some difference between the experimental and numerical results. However, numerical modeling could predict pipe uplift accurately in STC 30% sample.
- Buried pipelines may go out of service because of liquefaction-induced uplift. The shear resistance reduction of the liquefied sand and the pipe's light weight engendered the pipe uplift. Besides, the EPWP underneath the pipe surpasses the initial effective vertical stress.
- The numerical modeling outcomes indicated that the UBCSAND soil constitutive model could simulate EPWP and accurately predict the liquefaction phenomenon in the saturated SGR mixture. The pipe uplift recorded during the base excitation is compared with the computed uplift from the numerical model. Numerical modeling using the UBCSAND soil constitutive model could predict pipe uplift accurately.
- Regarding the burial depth ratio (H/D), the failure mechanism is divided into two shallow and deep failure mechanisms. H/D = 2.5 can be selected as the critical burial depth ratio. The buried pipes with a H/D ratio less than 2.5 fail in the shallow failure mechanism, and the samples with a H/D ratio more than 2.5 fail in the deep failure mechanism.
- Although it appears that increasing the burial depth increases the FoS of the buried structure against liquefaction-induced uplift because of overloading, the results indicate that analytical limit-equilibrium methods based on inclined wedge failure mechanism could not be used for deeply buried pipes because of its local failure mechanism tendency. The deeply buried pipe fails in the punching mode mechanism (unlike the inclined slip surface model) and experiences uplift.
- The following analytical formula was proposed to estimate the liquefaction-induced uplift of buried pipes based on the acceleration ratio (a_{max}/g), the pipe diameter ratio (D/H), and input shaking duration (t) variations.

$$Uplift\ (mm) = 15.5t\left(\frac{a_{max}}{g}\right)^{0.95}\left(\frac{D}{H}\right)^{2} - 4.4t\left(\frac{a_{max}}{g}\right)^{1.9}\left(\frac{D}{H}\right) + 3.2t\left(\frac{a_{max}}{g}\right)^{1.3}$$

The suggested formula predicts the ultimate uplift of the buried pipe in the studied SGR mixture under sinusoidal excitation with a constant frequency of 2Hz. The proposed equation can be applied in probabilistic analyses to estimate the pipe uplift.

5.3. Recommendations

- Study the uplift behavior of buried pipe in liquefied soil regarding the different soil densities. Due to the soil sand's complicated behavior and its dependence on the soil density, the numerical study of the effect of the variables leads to a better understanding of the phenomena.
- The replacement of sand materials above the buried pipe with coarse aggregates and studying the prevention effect of this method is known as one of the improvement methods to prevent the buried pipe uplift.
- Study the buried pipe uplift behavior in liquefied soil by considering a wide range of seismic loads with different seismic specifications in order to find the effect of load intensity on the buried pipe uplift.
- Using pipe with lower rigidity (flexible) and studying its effect on the soil behavior around the pipe as well as the buried pipe uplift.
- Developing numerical study using modified UBCSAND (UBCSAND 2) constitutive model to consider the effects of principal stress rotation (PSR) on results.
- Using FLAC 3D software to study the uplift behavior of buried pipe.

APPENDIX A

FACTOR OF SAFETY FOR PIPE UPLIFT

Appendix A details the procedure of calculating the safety factors for the samples listed in Table 4.7. The FoS versus uplift of four samples was calculated using the Chian and Madabhushi, 2012 theoretical uplift formulation with the same a_{max}/g of 0.35 and a variable burial depth ratio (H/D).

A.1. H=35 cm and D=5 cm and a_{max}=0.35g

Embedment ratio: H/D=7

F_B-F_T+F_{EPP}>F_{WS}+F_{SP}

$$F.S = \frac{F_{WS}+F_{SP}}{F_B - F_T + F_{EPP}}$$

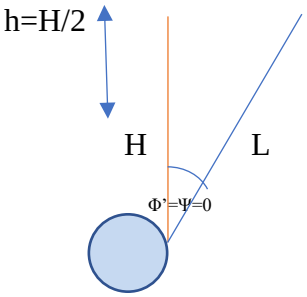

For vertical wedge mechanism:

$$F_{WS} = \left[\left(H.D - \frac{\pi.D^2}{8} + H^2.\tan\acute{\phi}\right).\acute{\gamma}\right]$$ 0 constant

$\gamma' = \gamma_{sat} - \gamma_w$ = 19.8 - 10 = 9.8 kN/m^3

H=35 cm and D=5 cm

F_{WS} = [(0.35*0.05) - (3.14*0.05^2/8)] * 9.8) = 0.1618 kN

$$F_B = \frac{\pi.D^2}{4}.\gamma_w$$ Archimedes' principle

F_B = (3.14*0.05^2/4) * 10=0.02 kN

$$F_T = \pi.D.t.\gamma_s$$

F_T=3.14*0.05*0.0018*13.83 = 0.0039 kN

F_{EPP} = [$(EPP)_{Bot}$ - $(EPP)_{Up}$) * D

$(EPP)_{Bot}$ = 6.7e4 - 3.68e4 = 3e4 Scaled=3e3 kPa

$(EPP)_{Up}$ = 5.5e4 - 3.1e4 = 2.4e4 Scaled = 2.4e3 kPa

F_{EPP} = [3-2.4] * 0.05 = 0.03 kN

F_{SP} = 0 for fully liquefied sand (r_u= 1)

$$F.S = \frac{F_{WS} + F_{SP}}{F_B - F_T + F_{EPP}} = \frac{0.1618 + 0}{0.02 - 0.004 + 0.03} = 3.5$$

A.2. H=35 cm and D=20 cm and a_{max}=0.35g

Embedment ratio: H/D=1.75

F_B-F_T+F_{EPP}>F_{WS}+F_{SP}

$$F.S = \frac{F_{WS}+F_{SP}}{F_B - F_T + F_{EPP}}$$

$$F_{WS} = \left[\left(H.D - \frac{\pi.D^2}{8} + H^2.\tan\acute{\emptyset}\right).\acute{\gamma}\right]$$ 0 constant

$\gamma' = \gamma_{sat} - \gamma_w$ = 19.8 – 10 = 9.8 kN/m^3

H=35 cm and D=20 cm

F_{WS} = [(0.35*0.2) - (3.14*0.2^2/8)] * 9.8) = 0.5321 kN

$F_B = \frac{\pi.D^2}{4}.\gamma_w$ Archimedes' principle

F_B = (3.14*0.2^2/4) * 10 = 0.314 kN

$$F_T = \pi . D . t . \gamma_s$$

F_T=3.14*0.2*0.0018*13.83 = 0.0156 kN

F_{EPP} = [$(EPP)_{Bot}$ - $(EPP)_{Up}$) * D

$(EPP)_{Bot}$ = 6.9e4 - 3.96e4 = 3.8e4 Scaled=3e3 kPa

$(EPP)_{Up}$=3.3e4- 2.36e4 = 1e4 Scaled=1e3 kPa

F_{EPP} = [3-1] * 0.2 = 0.4 kN

$$F.S = \frac{F_{WS} + F_{SP}}{F_B - F_T + F_{EPP}} = \frac{0.53 + 0}{0.314 - 0.015 + 0.4} = 0.75$$

A.3. H=65 cm and D=5 cm and a_{max}=0.35g

Embedment ratio: H/D=13

F_B-F_T+F_{EPP}>F_{WS}+F_{SP}

$$F.S = \frac{F_{WS}+F_{SP}}{F_B - F_T + F_{EPP}}$$

$$F_{WS} = \left[\left(H.D - \frac{\pi.D^2}{8} + H^2.\tan \acute{\emptyset}\right).\acute{\gamma}\right]$$ 0 constant

γ'=γ_{sat} - γ_w = 19.8 – 10 = 9.8 kN/m^3

H=65 cm and D=5 cm

F_{WS} = [(0.65*0.05) - (3.14*0.05^2/8)] * 9.8) = 0.3088 kN

$$F_B = \frac{\pi.D^2}{4}.\gamma_w$$ Archimedes' principle

$F_B = (3.14*0.05^2/4) * 10 = 0.02$ kN

$$F_T = \pi . D . t . \gamma_s$$

$F_T = 3.14*0.05*0.0018*13.83 = 0.0039$ kN

$F_{EPP} = [(EPP)_{Bot} - (EPP)_{Up}) * D$

$(EPP)_{Bot} = 12.3e4 - 7.34e4 = 5e4$ Scaled=5e3 kPa

$(EPP)_{Up} = 11.2e4 - 6.75e4 = 4.5e4$ Scaled=4.5e3 kPa

$F_{EPP} = [5-4.5] * 0.05 = 0.025$ kN

A.4. H=65 cm and D=20 cm and a_{max}=0.35g

Embedment ratio: H/D=3.25

$F_B - F_T + F_{EPP} > F_{WS} + F_{SP}$

$$F.S = \frac{F_{WS}+F_{SP}}{F_B - F_T + F_{EPP}}$$

$$F_{WS} = \left[\left(H.D - \frac{\pi.D^2}{8} + H^2.\tan\acute{\emptyset}\right).\acute{\gamma}\right]$$ 0 constant

$\gamma' = \gamma_{sat} - \gamma_w = 19.8 - 10 = 9.8$ kN/m^3

H=35 cm and D=20 cm

$F_{WS} = [(0.65*0.2) - (3.14*0.2^2/8)] * 9.8) = 1.1201$ kN

$F_B = \frac{\pi.D^2}{4}.\gamma_w$ Archimedes' principle

F_B=(3.14*0.2^2/4)*10 = 0.314 kN

$$F_T = \pi . D . t . \gamma_s$$

F_T=3.14*0.2*0.0018*13.83 = 0.0156 kN

F_{EPP} = [$(EPP)_{Bot}$- $(EPP)_{Up}$] * D

$(EPP)_{Bot}$ = 12.1e4 - 7.77e4 = 4.3e4 Scaled=4.3e3 kPa

$(EPP)_{Up}$ = 8.5e4- 5.762e4 = 2.7e4 Scaled=2.7e3 kPa

F_{EPP}=[4.3-2.7]*0.2=0.32 kN

$$F.S = \frac{F_{WS} + F_{SP}}{F_B - F_T + F_{EPP}} = \frac{1.12 + 0}{0.314 - 0.015 + 0.32} = 1.81$$

APPENDIX B

UPLIFT AMOUNTS OBTAINED FROM NUMERICAL AND ANALYTICAL CALCULATIONS

The uplift values derived from the numerical analysis and the proposed formula for a_{max}= 0.2g, 0.35g, and 0.5g were compared and presented in Appendix B.

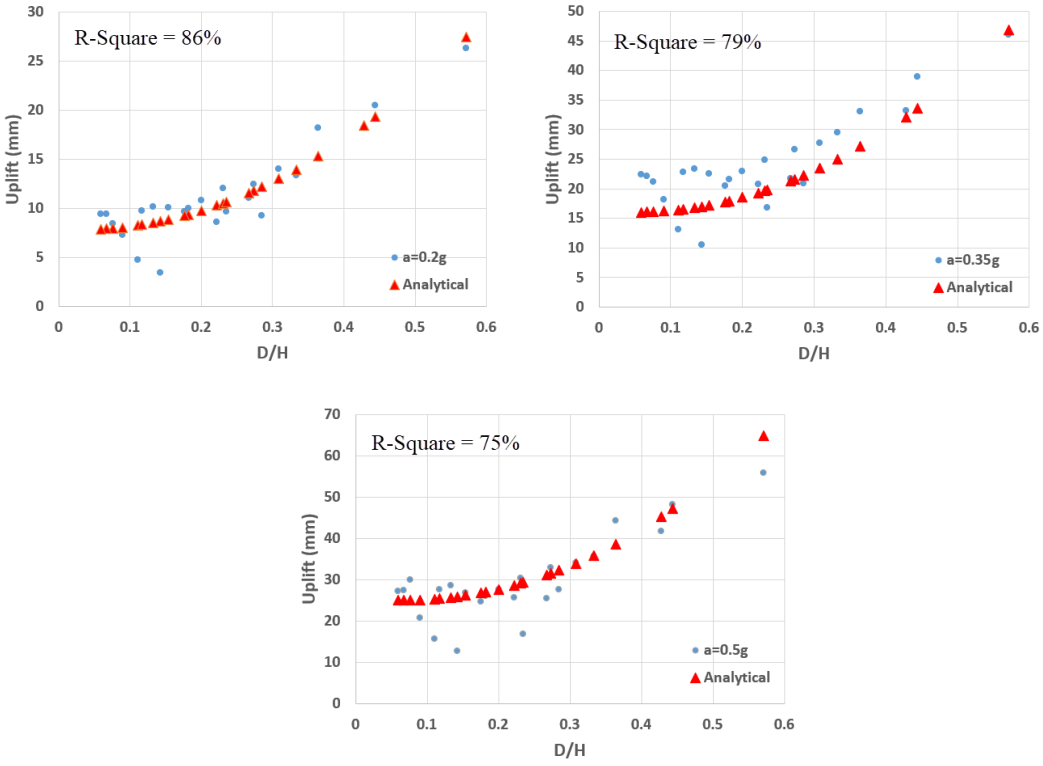

Figure B.1. Comparing uplift values obtained from numerical study and proposed formula for a_{max}= 0.2g, 0.35g, and 0.5g

Table B.1. Uplift results of samples obtained from numerical and analytical studies (a_{max}=0.2g)

a_{max}=0.2g			
Test #	D/H	Uplift (mm)	
		Numerical	Analytical
1	0.143	3.41	8.68
2	0.285	9.26	12.18
3	0.428	18.20	18.45
4	0.571	26.34	27.46
5	0.111	4.75	8.27
6	0.222	8.62	10.29
7	0.333	13.36	13.98
8	0.444	20.50	19.32
9	0.090	7.34	8.07
10	0.182	9.97	9.37
11	0.273	12.47	11.78
12	0.364	18.18	15.30
13	0.076	8.41	7.97
14	0.154	10.06	8.86
15	0.231	12.03	10.53
16	0.308	14.03	13.00
17	0.067	9.40	7.92
18	0.133	10.13	8.54
19	0.200	10.84	9.76
20	0.267	11.07	11.59
21	0.059	9.42	7.89
22	0.117	9.77	8.34
23	0.176	9.70	9.25
24	0.235	9.65	10.64

Table B.2. Uplift results of samples obtained from numerical and analytical studies (a_{max}=0.35g)

a_{max}=0.35g			
Test #	D/H	Uplift (mm)	
		Numerical	Analytical
25	0.143	10.57	16.97
26	0.285	20.96	22.23
27	0.428	33.18	32.18
28	0.571	46.10	46.81
29	0.111	13.08	16.43
30	0.222	20.78	19.33
31	0.333	29.45	25.04
32	0.444	38.96	33.58
33	0.090	18.18	16.20
34	0.182	21.53	17.96
35	0.273	26.58	21.60
36	0.364	33.03	27.15
37	0.076	21.16	16.10
38	0.154	22.61	17.22
39	0.231	24.81	19.68
40	0.308	27.79	23.51
41	0.067	22.15	16.06
42	0.133	23.36	16.78
43	0.200	23.00	18.53
44	0.267	21.76	21.30
45	0.059	22.40	16.04
46	0.117	22.89	16.51
47	0.176	20.56	17.78
48	0.235	16.77	19.85

Table B.3. Uplift results of samples obtained from numerical and analytical studies (a_{max}=0.5g)

a_{max}=0.5g			
Test #	D/H	Uplift (mm)	
		Numerical	Analytical
49	0.143	12.80	25.90
50	0.285	27.54	32.30
51	0.428	41.64	45.30
52	0.571	55.73	64.86
53	0.111	15.75	25.35
54	0.222	25.61	28.66
55	0.333	35.56	35.93
56	0.444	48.27	47.16
57	0.090	20.84	25.17
58	0.182	25.98	27.01
59	0.273	32.96	31.51
60	0.364	44.20	38.67
61	0.076	30.02	25.13
62	0.154	26.79	26.16
63	0.231	30.34	29.10
64	0.308	34.00	33.95
65	0.067	27.49	25.13
66	0.133	28.60	25.69
67	0.200	27.61	27.69
68	0.267	25.53	31.13
69	0.059	27.22	25.16
70	0.117	27.62	25.43
71	0.176	24.59	26.81
72	0.235	16.90	29.31

REFERENCES

Alliance, A. L. 2001. “Guidelines for the design of buried steel pipe”. FEMA, p. 75.

American Society for Testing and Materials, ASTM D6270–98: 1998. “Standard practice for use of scrap tires in civil engineering applications,” ASTM International, West Conshohocken, PA, USA.

American Society for Testing and Materials, ASTM D422, 2004a. “standard test method for particle-size analysis of soils,” West Conshohocken, PA, USA.

American Society for Testing and Materials, ASTM D5681-18, 2018. “Standard Terminology for waste and waste management,” West Conshohocken, Pa: ASTM International.

American Society for Testing and Materials, ASTM D6270–08, 2012. “Standard practice for use of scrap tires in civil engineering applications,” (Reapproved, 2012). DOI: https:// doi. org/ 10. 1520/ D6270- 08R12.2.

Attom, M.F. 2006. “The use of shredded waste tires to improve the geotechnical engineering properties of sand,” Envion Geol., 49:497–503. https://doi.org/10.1007/s00254-005-0003-5.

Azadi, M., Hosseini, S.M. 2010. “The uplifting behavior of shallow tunnels within the liquefiable soils under cyclic loadings,” Tunn. Undergr. Space Technol., 25 (2), 158–167. https://doi.org/10.1016/j.tust.2009.10.004.

Bahadori, H., Manafi, S. 2015. “Effect of tyre chips on dynamic properties of saturated sands,” International Journal of Physical Modelling in Geotechnics, Paper 1300014. http://dx.doi.org/10.1680/ijpmg.13.00014

Beaty, M.H., Byrne, P.M. 2011. “UBCSAND constitutive model,” Version 904aR. Documentation Report: UBCSAND Constitutive Model on Itasca UDM Web Site; February 2011.
http://www.itasca-udm.com/pages/UBCSand.html.

Beaty, M.H. 2018. “Application of UBCSAND to the LEAP centrifuge experiments,” Soil Dynamics and Earthquake Engineering, 104, 143–153. http://dx.doi.org/10.1016/j.soildyn.2017.10.006.

Belytschko, T. 1983. “An Overview of Semidiscretization and Time Integration Procedures,” in Computational Methods for Transient Analysis, Ch. 1, pp. 1-65. T. Belytschko and T. J. R. Hughes, eds. New York: Elsevier Science Publishers, B.V.

Bhattacharya, S., Madabhushi, S. and Bolton, M. 2003. “Pile instability during earthquake liquefaction,” University of Cambridge Cambridge, UK, 2003.

Byrne, P.M., Park, S., Beaty, M., Sharp, M., Gonzalez, L., Abdoun, T. 2004. “Numerical modeling of liquefaction and comparison with centrifuge tests,” Can. Geotech. J., 41, 193–211.
https://doi.org/10.1139/t03-088.

Castiglia, M., Santucci de Magistris, F., Koseki, J. 2019. “Uplift of buried pipelines in liquefiable soils using shaking table apparatus,” In 7th International Conference on Earthquake Geotechnical Engineering, ICEGE 2019, 1638–1646. ISBN 978–0–367–14328–2.

Castiglia, M., Santucci de Magistris, F., Morgante, S., Koseki, J. 2020. “Geogrids as a Remedial measure for seismic-liquefaction induced uplift of onshore buried gas pipelines,” National conference of the researchers of geotechnical engineering, CNRIG 2019: Geotechnical Research for Land Protection and Development, 649–657.
DOI: https:// doi. org/ 10. 1007/ 978-3- 030- 21359-6_ 69.

Chapter 8, 2018. “Liquefaction With the Great East Japan Earthquake,” in The Fukushima and Tohoku Disaster, S. Faculty of Societal Safety, Ed.: Butterworth-Heinemann, pp. 147-159.

Chen, S., Tang, B., Zhao, K., Li, X., Zhuang, H. 2020. “Seismic response of irregular underground structures under adverse soil conditions using shaking table tests,” Tunnelling and Underground Space Technology, Volume 95, 103145. https://doi.org/10.1016/j.tust.2019.103145.

Chian, S. and Tokimatsu, K. 2011. “Floatation of underground structures during the Mw 9.0 Tōhoku Earthquake of 11th March 2011,” in Proceedings of the 15th World Conference on Earthquake Engineering, Lisbon, Paper ID, vol. 3705.

Chian, S. C., Tokimatsu, K. and Madabhushi, S. P. G. 2014. “Soil liquefaction–induced uplift of underground structures: physical and numerical modeling,” Journal of Geotechnical and Geoenvironmental Engineering, vol. 140 ,no. 10, p. 04014057.

Chian S. and Tokimatsu, K. 2012. “Floatation of underground structures during the Mw 9.0 Tōhoku Earthquake of March 11 2011,” in Proceedings of the 15th World Conference on Earthquake Engineering, Lisbon, Paper ID, vol. 3705.

Chian S. C., and Madabhushi S. P. G. 2012. “EFFECT OF SOIL CONDITIONS ON UPLIFT OF UNDERGROUND STRUCTURES IN LIQUEFIED SOIL,” Journal of Earthquake and Tsunami, Vol. 6, No. 4 (2012) 1250020 (20 pages). DOI: 10.1142/S1793431112500200.

Chian, S.C., Madabhushi, S.P.G. 2012. “Effect of buried depth and diameter on uplift of underground structures in liquefied soils,” Soil Dynamics and Earthquake Engineering, 41, 181–190. http://dx.doi.org/10.1016/j.soildyn.2012.05.020.

Chou, J.C., Yang, H.T., Lin, D.G. 2021. “Calibration of Finn Model and UBCSAND Model for Simplified Liquefaction Analysis Procedures,” Appl. Sci., 11, 5283. https://doi.org/10.3390/app11115283.

Chou, J.C., Kutter, B.L., Travasarou, T., Chacko, J.M. 2011. “Centrifuge modeling of seismically induced uplift for the BART Transbay tube,” J. Geotech. Geoenviron. Eng., 137, 754–765. https://doi.org/10.1061/(ASCE)GT.1943-5606.0000489.

Christ, M., Park, J.B. 2010. “Laboratory determination of strength properties of frozen rubber-sand mixtures,” Cold Reg Sci Technol 2010; 60: 169–75. https://doi.org/10.1016/j.coldregions.2009.08.013.

CWA, 2002. “CEN workshop agreement 14243,” 2002 Postconsumer tire materials and applications CEN, Brussels.

Das, B. M. 1983. “Fundamentals of soil dynamics,” (no. Sirsi) (i9780444007056).

Duncan, J.M., and Chang, C.Y. 1970. “Nonlinear analysis of stress and strain in soil,” ASCE Journal of the Soil Mechanics and Foundations Division; 96:1629–53.

Ecemis, N. 2021. “Experimental and numerical modeling on the liquefaction potential and ground settlement of silt-interlayered stratified sands,” Soil Dynamics and Earthquake Engineering, 144, 106691. https://doi.org/10.1016/j.soildyn.2021.106691.

Ecemis, N., Valizadeh, H., Karaman, M. 2021. “Sand-Granulated-Rubber Mixture to Prevent Liquefaction-Induced Uplift of Buried Pipes: A Shaking-Table Study,” Bulletin of Earthquake Engineering, Volume 19, pages 2817–2838. https://doi.org/10.1007/s10518-021-01091-3.

Ecemis, N. 2013. “Simulation of seismic liquefaction: 1-g model testing system and shaking table tests,” European Journal of Environmental and Civil Engineering, Vol. 17, No. 10, 899–919. http://dx.doi.org/10.1080/19648189.2013.833140.

Eiksund, G. 2014. “Modelling of uplift and lateral resistance of offshore pipelines in rock berms,” Dept. of Civil and Transport Engineering, NTNU, Trondheim, Norway, June 2014.

Giridharan, Sh., Gowda, S., Stolle, D.F.E., Moormann, C. 2020. “Comparison of UBCSAND and Hypoplastic soil model predictions using the Material Point Method,” Soils and Foundations, 60 989–1000. https://doi.org/10.1016/j.sandf.2020.06.001.

Gotteland, P., Lambert, S., Balachowski, L. 2005. “Strength characteristics of tire chips-sand mixture,” Stud Geotech Mech 27(1):55–66.

Hu, J., Chen, Q., Liu, H. 2018. “Relationship between earthquake-induced uplift of rectangular underground structures and the excess pore water pressure ratio in saturated sandy soils,” Tunnelling and Underground Space Technology, 79, 35–51. https://doi.org/10.1016/j.tust.2018.04.039.

Huang, B., Liu, J., Lin, P. and Ling, D. 2014. “Uplifting behavior of shallow buried pipe in liquefiable soil by dynamic centrifuge test,” The Scientific World Journal, vol. 2014, Article ID 838546.

Itasca Consulting Group, I. 2011. FLAC-fast Lagrangian analysis of continua, User's manual, version 7.0, Minneapolis.

Ishihara, K. 1993. “Liquefaction and flow failure during earthquakes,” *Geotechnique,* vol. 43, no. 3, pp. 351-451.

Ishihara, K., Towhata, I. 1983. “Sand response to cyclic rotation of principal stress directions as induced by wave loads,” Soils Found., 23(4) 11-26.

Jamshidi Chenari R., Fatahi B., Akhavan Maroufi MA., Alaie R. 2017. “An Experimental and Numerical Investigation into the Compressibility and Settlement of Sand

Mixed with TDA," Geotechnical and Geological Engineering, 35(2), pp. 2401-2420.
DOI 10.1007/s10706-017-0255-3.

Kaneko, T., Rolando, P.O., Masayuki, H., Norimasa, Y. 2013. "Seismic response characteristics of saturated sand deposits mixed with tire chips," J Geotech Geoenviron Eng 139(4):633–643.
https:// doi. org/ 10. 1061/(ASCE) GT. 1943- 5606. 00007 52.

Kramer, S. L. 1996. "Geotechnical Earthquake Engineering," Pren-tice Hall, New Jersey, 2005.

Koseki, J., Matsuo, O., and Koga, Y. 1997. "Uplift Behavior of Underground Structures caused by Liquefaction of Surrounding Soil during Earthquake," Soils and Foundations, Vol. 37, No. 1, 97-108.

Kuhlemeyer, R.L., Lysmer, J., 1973. "Finite element method accuracy for wave propagation problems," Journal of Soil Mechanics and Foundations. Div. ASCE 99, 421–427.
https://doi.org/10.1061/JSFEAQ.0001885.

Ling, HI., Mohri, Y., Kawabata, T., Liu, H., Burke, C., Sun, L. 2003. "Centrifugal modeling of seismic behaviour of large-diameter pipe in liquefiable soil," J. Geotech. Geoenviron. Eng., 129, 1092–1101.
https://doi.org/10.1061/(ASCE)1090-0241(2003)129:12(1092).

Liu, L., Cai, G., Zhang, J., Liu, X., Liu, K. 2020. "Evaluation of engineering properties and environmental effect of recycled waste tire-sand/soil in geotechnical engineering: A compressive review," Renewable and Sustainable Energy Reviews, 126, 109831.
https://doi.org/10.1016/j.rser.2020.109831.

Liu, L., Cai, G., Liu, S. 2018. “Compression properties and micro-mechanisms of rubber-sand particle mixtures considering grain breakage,” Construct Build Mater 2018;187: 1061–72. https://doi.org/10.1016/j.conbuildmat.2018.08.051.

Liu, H., Song, E. 2006. “Working mechanism of cutoff walls in reducing uplift of large underground structures induced by soil liquefaction,” Computers and Geotechnics; 33, 209–221. https://doi.org/10.1016/j.compgeo.2006.07.002.

Liu, L., Cai, G., Zhang, J., Liu, X., Liu, K. 2020. “Evaluation of engineering properties and environmental effect of recycled waste tire-sand/soil in geotechnical engineering: A compressive review,” Renewable and Sustainable Energy Reviews, Volume 126, 109831. https://doi.org/10.1016/j.rser.2020.109831.

Mahmoud, A.O., Hussien, M.N., Karray, M., Chekired, M., Bessette, C., Jingad, L. 2020. “Mitigation of liquefaction-induced uplift of underground structures,” Computers and Geotechnics; Volume 125, 103663. https://doi.org/10.1016/j.compgeo.2020.103663.

Marto, A., Latifi, N., Moradi, R., Oghabi, M., Zolfeghari. S.Y. 2013. “Shear properties of sand-tire chips mixtures,” Electron J Geotech Eng; 18: 325–34.

Morales, E., Filiatrault, A., Aref, A. 2018. “Seismic floor isolation using recycled tires for essential buildings in developing countries,” Bull Earthq Eng., 16:6299–333. https://doi.org/10.1007/s10518-018-0416-7.

Newmark, N.M., Hall, W.J. 1982. “Earthquake spectra and design, monograph,” earthquake engineering research Institute (EERI): 1982, Oakland, CA. Newmark.

Noorzad, R., Raveshi, M. 2017. “Mechanical Behavior of Waste Tire Crumbs–Sand Mixtures Determined by Triaxial Tests,” Geotechnical and Geological Engineering volume 35, pages1793–1802. https://doi.org/10.1007/s10706-017-0209-9.

Neaz Sheikh, M., Mashiri, M., Vinod, J., Tsang, HH. 2012. “Shear and compressibility behavior of sand–tire crumb mixtures,” J Mater Civ Eng., 25:1366–74. https://doi.org/10.1061/(ASCE)MT.1943-5533.0000696.

O'Rourke, T. 1996. “Lessons learned for lifeline engineering from major urban earthquakes,” in Eleventh World Conference on Earthquake Engineering, 1996.

Robertson, P.K., Campanella, R.G., Wightman, A. 1983. “SPT-CPT correlations,” J Geotech Eng, ASCE;109(11):1449–59.

Rubeiz, C. G. 2009. “Performance of Pipes during Earthquakes,” in Pipelines 2009: Infrastructure's Hidden Assets, pp. 1205-1215.

Saberian, M., Li, J., Thach Nguyen, B., Boroujeni, M. 2020. “Experimental and analytical study of dynamic properties of UGM materials containing waste rubber,” Soil Dynamics and Earthquake Engineering, 130, 105978. https://doi.org/10.1016/j.soildyn.2019.105978.

Saeedzadeh, R. and Hataf, N. 2011. “Uplift response of buried pipelines in saturated sand deposit under earthquake loading,” Soil Dynamics and Earthquake Engineering, vol. 31, no. 10, pp. 1378-1384.

Seed, H.B. and Idriss, I. M., 1971. “Simplified Procedure for Evaluating Soil Liquefaction Potential,” Journal of the Soil Mechanics and Foundation Division, ASCE, Vol. 97, No SM9, Proc. Paper 8371, pp. 1249-1273.

Seed, H.B. and Idriss, I. M., 1970. “Soil moduli and damping factors for dynamic response analyses,” Earthquake Engineering Research Center Report No. UCB/EERC/70-10, University of California at Berkeley.

Seed, H.B., Wong, R.T., Idriss, I.M., Tokimatsu, K. 1986. “Moduli and damping factors for dynamic analyses of cohesionless soils,” J Geotech Eng, ASCE 1986;112(11), 1016–32.
https://doi.org/10.1061/(ASCE)0733-9410(1986)112:11(1016).

Sharafi, H., Parsafar, P. 2016. “Seismic simulation of liquefaction-induced uplift behavior of buried pipelines in shallow ground,” Arab J Geosci, 9:215 Pages No. 9.
DOI 10.1007/s12517-015-2025-y.

Sun, Q., Dias, D., Guo, X., Li, P. 2019. “Numerical study on the effect of a subway station on the surface ground motion. Computers and Geotechnics; 111, 243–254.
https://doi.org/10.1016/j.compgeo.2019.03.026.

Su, H., Yang, J., Ling, TC. Ghataora GS., Dirar S. 2015. “Properties of concrete prepared with waste tyre rubber particles of uniform and varying sizes,” J Clean Prod, 91: 288–96.
DOI: 10.1016/j.jclepro.2014.12.022.

Tafreshi, SM., Mehrjardi, GT., Dawson, A. 2012. “Buried pipes in rubber-soil backfilled trenches under cyclic loading,” J Geotech Eng 2012; 138:1346–56.
https://doi.org/10.1061/(ASCE)GT.1943-5606.0000710.

Topalidisz, M. 2018. “Numerical modeling of the seismic response of gas pipelines in liquefiable sand,” Thesis to obtain the Master of Science Degree in Civil Engineering, July 2018, TECNICO LISBOA.

Tobita, T., Iai, S., Kang, G. and Konishi, Y. 2009. “Observed damage of wastewater pipelines and estimated manhole uplifts during the 2004 Niigataken Chuetsu, Japan, earthquake,” in TCLEE 2009: Lifeline Earthquake Engineering in a Multihazard Environment, pp. 1-12.

Tokimatsu, K., Tamura, S., Suzuki, H., Katsumata, K. 2012. “Building damage associated with geotechnical problems in the 2011 Tohoku Pacific earthquake,” Soils Found., 52 (5), 956–974.
https://doi.org/10.1016/j.sandf.2012.11.014.

Uchimura, T., Chi, NA., Nirmalan, S. Sato, T., Meidani, M., and Towhata, I. 2007. “Shaking table tests on effect of tire chips and sand mixture in increasing liquefaction resistance and mitigating uplift of pipe,” Proc., Int. Workshop on Scrap Tire Derived Materials (IW-TDGM2007), Taylor and Francis Group, London, 179- 182.

Uygunoglu, T., Topçu, IB. 2010. “The role of scrap rubber particles on the drying shrinkage and mechanical properties of self-consolidating mortars,” Construct Build Mater, 24, 1141–50.
https://doi.org/10.1016/j.conbuildmat.2009.12.027.

Yasuda, S. and Kiku, H. 2006. “Uplift of sewage manholes and pipes during the 2004 Niigataken-Chuetsu earthquake,” Soils and Foundations, vol. 46, no. 6, pp. 885-894.

Yasuda, S., Nagase, H., Itafuji, S., Sawada, H. and Mine, K. 1994. “Shaking table tests on floatation of buried pipes due to liquefaction of backfill sands,” in Technical Report NCEER, vol. 94: US National Center for Earthquake Engineering Research (NCEER), pp. 665-77.

Yamaguchi, A., Mori, T., Kazama, M., Yoshida, N. 2012. “Liquefaction in Tohoku district during the 2011 off the Pacific Coast of Tohoku Earthquake,” Soils and Foundations, Volume 52, Issue 5, Pages 811-829.
https://doi.org/10.1016/j.sandf.2012.11.005

Yoshida, M., Miyajima, M. and Kitaura, M. 2008. “Experimental Study on Mitigation of Liquefaction-Induced Flotation of Severage Manhole by Using Permeable Recycled Materials Packed in Sandbags,” The 14th World Conference on Earthquake Engineering.

White, D. J., Barefoot, A.J., Bolton, M.D. 2001. “Centrifuge model-ling of upheaval buckling in sand,” International Journal of Physi-cal Modelling in Geomechanics, 2, 19-28.

Zhai, E., Davis, C. A., Yan, L., and Hu, J. 2014. “Numerical simulations of geotechnical centrifuge modeling of seismic earth pressures on an underground restrained structure,” Int. Efforts in Lifeline Earthquake Engineering; ASCE, Reston, VA, 369-376.
https://doi.org/10.1061/9780784413234.048.

Zhao, H. Y., Zhu, J. F., Zheng, J. H., Zhang, J. S. 2020. “Numerical modelling of the fluid-seabed-structure interactions considering the impact of principal stress axes rotations,” Soil Dynamics and Earthquake Engineering, 136, 106242.
https://doi.org/10.1016/j.soildyn.2020.106242.

Zheng, G., Yang, P., Zhou, H., Zeng, C., Yang, X., He, X., Yu, X. 2019. “Evaluation of the earthquake induced uplift displacement of tunnels using multivariate adaptive regression splines,” Computers and Geotechnics, 113, 103099.
https://doi.org/10.1016/j.compgeo.2019.103099.

Zhou, J., Jiang, J., Chen, X. 2015. “Micro-and macro-observations of liquefaction of saturated sand around buried structures in centrifuge shaking table tests,” Soil Dyn. Earthq. Eng. 72, 1–11.
https://doi.org/10.1016/j.soildyn.2014.12.017.